

OMI Algorithm Theoretical Basis Document

Volume II

OMI Ozone Products

Edited by
Pawan K Bhartia
NASA Goddard Space Flight Center
Greenbelt, Maryland, USA

ATBD-OMI-02, Version 2.0, August 2002

Preface

Background

The Ozone Monitoring Instrument OMI is a Dutch-Finnish ozone monitoring instrument that will fly on NASA's Aura Mission, part of the Earth Observation System (EOS), scheduled for launch in January 2004. OMI's measurements of ozone columns and profiles, aerosols, clouds, surface UV irradiance, and the trace gases NO₂, SO₂, HCHO, BrO, and OCIO fit well into Aura's mission goals to study the Earth's atmosphere. OMI is a wide swath, nadir viewing, near-UV and visible spectrograph which draws heavily on European experience in atmospheric research instruments such as GOME (on ERS-2), SCIAMACHY and GOMOS (both flying on Envisat).

Purpose

The four OMI-EOS Algorithm Theoretical Basis Documents (ATBDs) present a detailed picture of the instrument and the retrieval algorithms used to derive atmospheric information from the instrument's measurements. They will provide a clear understanding of the data-products to the OMI scientists, to the Aura Science Team, and the atmospheric community at large. Each chapter of the four ATBDs is written by the scientists responsible for the development of the algorithms presented.

These ATBDs were presented to a group of expert reviewers recruited mainly from the atmospheric research community outside of Aura. The results of the reviewer's study, critiques and recommendations were presented at the ATBD panel review on February 8th, 2002. Overall, the review was successful. All ATBDs, except the Level 1b ATBD, have been modified based on the recommendations of the written reviews and the panel, which were very helpful in the development of these documents. An updated level 1b ATBD is expected in the near future.

Contents

ATBD 1 contains a general description of the instrument and its measurement modes. In addition, there is a presentation of the Level 0 to 1B algorithms that convert instrument counts to calibrated radiances, ground and in-flight calibration, and the flight operations needed to collect science data. It is critical that this is well understood by the developers of the higher level processing, as they must know exactly what has been accounted for (and how), and what has not been considered in the Level 0 to 1B processing.

ATBD 2 covers several ozone products, which includes total ozone, profile ozone, and tropospheric ozone. The capability to observe a continuous spectrum makes it possible to use a DOAS (Differential Optical Absorption Spectroscopy) technique developed in connection with GOME, flying on ERS-2 to derive total column ozone. At the same time, an improved version of the TOMS total ozone column algorithm, developed and used successfully over 3 decades, will be used on OMI data. Completing the group of four algorithms in this ATBD is a separate, independent estimate of tropospheric column ozone, using an improved version of the Tropospheric Ozone Residual (TOR) and cloud slicing methods developed for TOMS. Following the recommendation of the review team, a chapter has been added which lays out the way ahead towards combining the individual ozone algorithms into fewer, and ultimately a single ozone "super" algorithm.

ATBD 3 presents retrieval algorithms for producing the aerosols, clouds, and surface UV radiation products. Retrieval of aerosol optical thickness and aerosol type is presented. Aerosols are of interest because they play an important role in tropospheric pollution and climate change.

The cloud products include cloud top height and effective cloud fraction, both of which are essential, for example, in retrieving the trace gas vertical columns accurately. Effective cloud fraction is obtained by comparing measured reflectance with the expected reflectance from a cloudless pixel and reflectance from a fully cloudy pixel with a Lambertian albedo of 0.8. Two complementary algorithms are presented for cloud-top height (or pressure). One uses a DOAS method, applied to the O₂-O₂ absorption band around 477 nm, while the other uses the filling-in of selected Fraunhofer lines in the range 352-398 nm due to rotational Raman scattering. Surface UV irradiance is important because of its damaging effects on human health, and on terrestrial and aquatic ecosystems. OMI will extend the long, continuous record produced by TOMS, using a refined algorithm based on the TOMS original.

ATBD 4 presents the retrieval algorithms for the “additional” trace gases that OMI will be able to monitor: NO₂, SO₂, HCHO, BrO, and OCIO. These gases are of interest because of their respective roles in stratospheric and tropospheric chemistry. Extensive experience with GOME has produced spectral fitting techniques used in these newly developed retrieval algorithms, each adapted to the specific characteristics of OMI and the particular molecule in question.

Summary

The four OMI-EOS ATBDs present in detail how each of OMI’s data products are produced. The data products described in the ATBD will make significant steps toward meeting the objectives of the NASA’s Earth Science Enterprise. OMI data products will make important contributions in addressing Aura’s scientific questions and will strengthen and compliment the atmospheric data products by the TES, MLS and HIRDLS instruments.

P.F. Levelt (KNMI, The Netherlands)

G.H.J. van den Oord (KNMI, The Netherlands)

E. Hilsenrath (NASA/GSFC, USA)

G.W Leppelmeier (FMI, Finland)

P.K. Bhartia (NASA/GSFC, USA)

Principal Investigator

Deputy PI

Co-PI

Co-PI

US ST Leader

TABLE OF CONTENT

	<i>Background</i>	2
	<i>Purpose</i>	2
	<i>Contents</i>	2
	<i>Summary</i>	3
1.	INTRODUCTION.....	7
1.1.	OVERVIEW.....	7
1.2.	PROPERTIES OF BACKSCATTERED UV (BUV) RADIATION.....	8
1.2.1.	O ₃ Absorption.....	8
1.2.2.	Molecular Scattering.....	9
1.2.3.	Trace Gas Absorption.....	10
1.2.4.	Cloud Scattering.....	10
1.2.5.	Aerosol Scattering.....	11
1.2.6.	Surface Reflection.....	12
1.3.	REFERENCES.....	12
2.	TOMS-V8 TOTAL O₃ ALGORITHM.....	15
2.1.	OVERVIEW.....	15
2.2.	FORWARD MODEL.....	15
2.2.1.	Spectroscopic Constants.....	16
2.2.2.	Ozone and Temperature Profiles.....	16
2.2.3.	Radiance Computation.....	18
2.2.4.	Accounting for aerosol and clouds.....	19
2.2.5.	Cloud height and surface pressure.....	20
2.3.	INVERSE ALGORITHM.....	20
2.3.1.	Basic Algorithm.....	20
	<i>Computation of Effective Reflectivity/Cloud Fraction</i>	21
	<i>Total O₃ computation</i>	21
2.3.2.	Corrections to the basic algorithm.....	23
	<i>Aerosols</i>	23
	<i>Sea-Glint</i>	24
	<i>Ozone Profile</i>	24
	<i>Sulfur dioxide (SO₂)</i>	25
2.4.	ERROR ANALYSIS.....	25
2.4.1.	Forward Model Errors.....	25
	<i>Radiative Transfer Code</i>	26
	<i>Spectroscopic Constants</i>	27
2.4.2.	Inverse Model Errors.....	27
	<i>O₃ Profile</i>	27
	<i>Temperature Profile</i>	28
2.4.3.	Instrumental Errors.....	28
	<i>Spectral Calibration</i>	28
	<i>Radiometric Calibration</i>	28
	<i>Instrument Noise</i>	28
2.4.4.	Error Summary.....	29
2.5.	VALIDATION.....	29
2.5.1.	Analysis of Residuals.....	29
2.5.2.	Internal Validation.....	30
2.5.3.	External Validation.....	30
2.6.	REFERENCES.....	31
3.	DOAS TOTAL O₃ ALGORITHM.....	33
3.1.	OVERVIEW.....	33

3.1.1.	Heritage	33
3.1.2.	Product description	33
3.2.	ALGORITHM DESCRIPTION	34
3.2.1.	Slant Column Density	34
	<i>Basic concept</i>	34
	<i>Ring effect</i>	35
	<i>Instrumental Errors</i>	36
	<i>Fit window</i>	37
	<i>Fit Method</i>	37
3.2.2.	Air Mass Factor (AMF)	38
	<i>Computation</i>	38
	<i>Radiative transfer model</i>	40
	<i>Look-up-Table</i>	40
3.2.3.	Cloud Correction.....	42
	<i>Cloud Model</i>	42
	<i>Air Mass Factor for Partly Cloudy Conditions</i>	42
	<i>Ghost Column</i>	42
	<i>Total Vertical Column Density</i>	43
3.3.	ERROR ANALYSIS	43
3.3.1.	Slant column density	43
	<i>Forward model errors</i>	44
	<i>A priori errors</i>	44
	<i>Instrument errors</i>	44
3.3.2.	Air mass factor (AMF).....	45
	<i>Forward model errors</i>	45
	<i>A priori errors</i>	46
3.3.3.	Cloud correction.....	46
3.3.4.	Error Budget.....	47
3.3.5.	Exceptional Cases	47
	<i>Desert Dust</i>	47
	<i>Biomass Burning</i>	47
	<i>Polar Stratospheric Clouds</i>	48
	<i>Large Solar Zenith Angles</i>	48
3.4.	VALIDATION.....	48
3.4.1.	Algorithm validation	49
3.4.2.	Product validation	49
3.5.	ACKNOWLEDGMENTS	50
3.6.	REFERENCES.....	50
4.	OZONE PROFILE ALGORITHM	53
4.1.	OVERVIEW.....	53
4.1.1.	Historical Background	53
4.1.2.	Processing Overview.....	54
4.1.3.	Product Description.....	55
4.2.	THE FORWARD MODEL.....	56
4.2.1.	Introduction.....	56
4.2.2.	Atmospheric state input to the RTM.....	56
	<i>Trace Gas Databases</i>	56
	<i>Aerosols</i>	57
	<i>Temperature/humidity</i>	57
	<i>Clouds</i>	57
	<i>Surface</i>	57
4.2.3.	Radiative transfer model (RTM).....	57
	<i>Single-scattering RTM</i>	58
	<i>Multiple-scattering RTM</i>	58
	<i>Computation of Jacobians</i>	59
	<i>Sphericity correction at large viewing angle</i>	60

	<i>Polarisation Correction</i>	60
	<i>Ring effect</i>	60
4.2.4.	Instrument Model	61
4.3.	INVERSE MODEL	61
4.3.1.	The problem of inversion	61
4.3.2.	Finding the Optimal Estimate	62
4.4.	IMPLEMENTATION OF THE OPERATIONAL ALGORITHM	62
4.4.1.	Level 1B Input and Usage	62
4.4.2.	Determination of measurement error covariance	63
4.4.3.	Definition of the state vector and a priori	63
4.4.4.	Performance Considerations	64
	<i>Forward Model Efficiency</i>	64
	<i>Fitting Window; size and binning</i>	64
	<i>Number of iterations</i>	66
4.5.	ERROR ANALYSIS	66
4.5.1.	Sources of error in the retrieval	66
	<i>Smoothing Error</i>	66
	<i>Measurement error contribution</i>	67
	<i>Model parameter errors</i>	67
	<i>Forward model errors</i>	67
	<i>Non-orthogonality of errors</i>	67
4.5.2.	Test data set: Input configuration	69
4.5.3.	Error analysis results	69
4.6.	DISCUSSION	72
4.7.	VALIDATION	72
4.8.	REFERENCES	74
5.	TROPOSPHERIC O₃ RESIDUAL	77
5.1.	OVERVIEW	77
5.2.	PROPOSED TOR ALGORITHM USING DATA FROM OMI AND HIRDLS	78
5.3.	ERROR ANALYSIS	81
5.3.1.	OMI Total O ₃ Error	82
5.3.2.	Error in Stratospheric Column Ozone (SCO)	83
5.3.3.	Interpolation Errors	83
5.3.4.	Error in Tropopause Height	83
5.4.	VALIDATION	84
5.4.1.	Comparison with Ozonesondes	84
5.4.2.	Coordinated Aircraft Campaigns	84
5.4.3.	Comparison with TES	85
5.5.	REFERENCES	86
6.	CONVERGENCE OF O₃ ALGORITHMS	89
6.1.	OVERVIEW	89
6.2.	PROFILE CORRECTION TO TOTAL O ₃ ALGORITHMS	89
6.3.	COMBINING TOMS AND DOAS ALGORITHMS	90
6.4.	COMBINING TOR AND PROFILE ALGORITHMS	91
6.5.	FULL CONVERGENCE OF THE 4 ALGORITHMS	91

1. Introduction

Pawan K Bhartia

NASA Goddard Space Flight Center, Greenbelt, Maryland, USA

1.1. Overview

This document describes the theoretical basis of the OMI ozone product algorithms. We propose to develop 3 separate ozone products from OMI: Total column ozone, ozone vertical profile, and tropospheric column ozone. We propose two independent total ozone algorithms—one developed at NASA/GSFC the other at KNMI/Netherlands.

The NASA algorithm is an enhanced version of the TOMS Version 8 (V8) algorithm, which is currently under development. V8 is the most recent version of the buv total ozone algorithms that have undergone 3 decades of progressive refinement. Its predecessor, V7, developed about 6 years ago, has been used to produce the acclaimed TOMS total ozone time-series. V8 will correct several small errors in V7 that were discovered by extensive error studies using radiative transfer models and by comparison with ground-based instruments. TOMS V8 uses only two wavelengths (317.5 and 331.2 nm) to derive total ozone. Other 4 TOMS wavelengths are used for diagnostics and error correction. Experience with TOMS suggests that the algorithm is capable of producing total ozone with rms error of about 2%, though these errors are not necessarily randomly distributed over the globe. The errors typically increase with solar zenith angle and in presence of heavy aerosol loading. Since V8 will be used to reprocess all SBUV and TOMS total ozone data taken since April 1970, we propose to apply it to OMI to ensure continuity of this unique data record. This algorithm will remain in operation until a demonstrably better algorithm using the enhanced capabilities of OMI is developed and the differences between the new algorithm and V8 are well understood.

The KNMI total ozone algorithm is based on the Differential Optical Absorption Spectroscopy (DOAS) that has been widely used to measure trace gases from ground. It has been applied successfully to process data from the GOME instrument that is currently flying on the ERS-2 satellite. Several groups, including KNMI, are using DOAS to estimate the total ozone column from the GOME instrument. As the technique is most suitable for weakly-absorbing trace gases, the ozone column is estimated from longer wavelengths than those used in the TOMS algorithm. In principle, DOAS is less sensitive to disturbing effects by absorbing aerosols, SO₂, and calibration errors than the TOMS algorithm. However, the ozone column derived from the operational DOAS algorithm shows systematic seasonal and latitudinal differences when compared to ground-based measurements. The DOAS algorithm we describe in this document uses a different spectral window to minimize O₃ profile and atmospheric temperature related errors.

The OMI profile algorithm is based on the maximum-likelihood estimation technique (also called optimal estimation) that has become standard in the field. It will take advantage of the hyperspectral capabilities of the OMI instrument to improve the vertical resolution of the ozone profile below 20 km compared to those from the SBUV instruments that have flown on NASA and NOAA satellites since 1970. It uses new approaches to calculate the required Jacobians in an efficient manner and to correct for polarization effects. In principle, this algorithm should be able to provide more accurate total O₃ estimates than the two algorithms discussed above, for it uses a broader range of OMI wavelengths that includes those that are used for total ozone. The total O₃ algorithms have some sensitivity to the ozone profile, particularly at large solar zenith angles, which could be better accounted for using OMI-derived ozone profiles. However, current implementation of the OMI profile algorithm is computationally slow, and

does not include corrections for cloud and aerosol effects. Given the complexity of hyperspectral profile retrieval algorithms and lack of operational experience with such algorithms, we think it is prudent to develop a separate total O₃ algorithm.

Since the vertical resolution of the O₃ profile derived from OMI is expected to be ~12 km near the tropopause, it would be difficult for the algorithm to reliably separate tropospheric O₃ from the lower stratospheric O₃, particularly in mid and high latitudes where the lower stratosphere O₃ has very large variability. Therefore, we propose to make a separate independent estimate of tropospheric column ozone using an improved version of the Tropospheric Ozone Residual (TOR) method developed for TOMS. In this algorithm one uses a high vertical resolution O₃-profiling instrument to determine the stratospheric ozone column, which is then subtracted from total column ozone. EOS Aura has two instruments, HIRDLS and MLS, that are designed to produce the stratospheric O₃ profile at high vertical resolution. The TOR algorithm will also use the “cloud slicing” technique developed for TOMS, which is insensitive to calibration but works best only in the tropics, to intercalibrate the various instruments.

This document is organized as follows. In the next section we provide an overview of key properties of backscattered ultraviolet radiation in the wavelength range used to derive OMI ozone products. The chapters following this introduction describe the theoretical basis of each of the 4 algorithms that will be used to produce the 3 ozone products mentioned above. The description includes error analysis, and a summary of the proposed validation plan. Finally, in chapter 6 we discuss how the 3 total O₃ algorithms discussed in this document could be merged into a single algorithm.

1.2. Properties of Backscattered UV (BUV) Radiation

The OMI instrument measures the radiation backscattered by the Earth’s atmosphere and surface in the wavelength range 270-500 nm. Though ozone has some absorption over this entire wavelength range (Fig. 1-1), OMI ozone products are derived using UV wavelengths, shorter than 340 nm, where the absorption is significant enough to permit reliable retrievals. Longer wavelengths are used for the retrieval of aerosol and cloud properties and for the estimation of column amounts of several trace gases (OCIO, BrO, HCHO, NO₂). These are discussed in other OMI ATBDs. In the following sub-sections we summarize key properties of the buv radiation in the 270-340 nm wavelength range that form the basis for the algorithms described in the subsequent chapters.

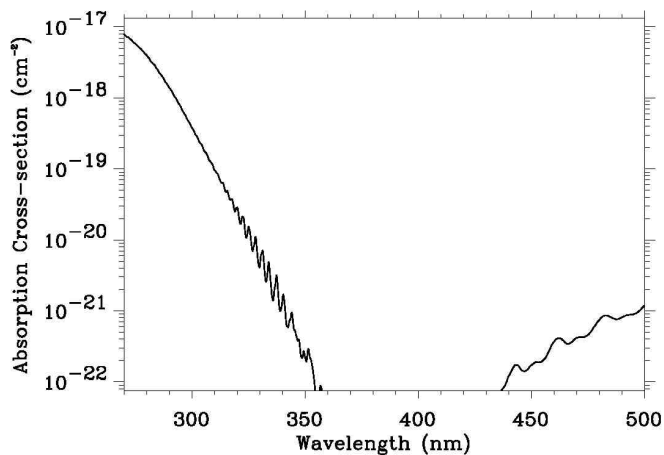


Figure 1-1: O₃ Absorption Spectrum at OMI Wavelengths

1.2.1. O₃ Absorption

By multiplying the ozone cross-sections given in Fig. 1-1 with typical O₃ column density of 1×10^{19} molecule/cm², one gets the vertical absorption optical depth of the atmosphere, which varies from 80 at 270 nm to 0.01 at 340 nm. Since 90% of this absorption occurs in the stratosphere, little radiation reaches the troposphere at wavelengths shorter than 295 nm, hence the radiation emanating from the earth at these wavelengths is unaffected by clouds, tropospheric

aerosols, and the surface. Therefore, the short wavelength buv radiation consists primarily of Rayleigh-scattered radiation from the molecular atmosphere, with small contributions by scattering from stratospheric aerosols [Torres & Bhartia, 1995], polar stratospheric clouds (PSC) [Torres et al., 1992], polar mesospheric clouds (PMC) [Thomas, 1984]; and emissions from NO [McPeters, 1989], Mg^{++} and other ionized elements. Ozone absorption controls the depth from which the Rayleigh-scattered radiation emanates which, as shown in Fig. 1-2, occurs over a fairly broad region of the atmosphere (roughly 16 km wide at the half maximum point) defined by the radiance contribution functions (RCF). As shown by Bhartia et al. [1996], the magnitude the buv radiation is proportional to the pressure at which the contribution function peaks, which occurs roughly at an altitude where the slant ozone absorption optical path is about one. This means that the basic information in the buv radiation is about the ozone column density as a function of pressure.

Fig. 1-2 also shows that the RCF becomes extremely broad at around 305 nm with two distinct peaks, one in the stratosphere the other in the troposphere. At longer wavelengths the stratospheric peak subsides and the tropospheric peak grows. Since roughly 95% of the ozone column is above the tropospheric peak, the radiation emanating from the troposphere essentially senses the entire ozone column, while the radiation emanating from the stratosphere senses the column above the RCF peak. Thus the longer wavelength OMI measurements (>310 nm) are suitable for measuring total ozone, while the middle wavelengths (~ 300 nm), after correction for the tropospheric component, provide information about the lower stratospheric ozone profile.

The magnitude of the buv radiation that emanates from the troposphere is determined by molecular, cloud, and aerosol scattering, reflection from the surface, and absorption by aerosol and other trace gases. In the following we provide basic information about each of these.

1.2.2. Molecular Scattering

In absence of clouds, Rayleigh scattering from the molecular atmosphere forms the dominant component of the radiation measured by OMI in the 270-340 nm wavelength range. Using the standard definition [Young, 1981], we define Rayleigh scattering as consisting of conservative scattering as well as non-conservative scattering, the latter consisting primarily of rotational Raman scattering (RRS) from O_2 and N_2 molecules [Kattawar et al., 1981, Chance & Spurr, 1997]. Though molecular scattering varies smoothly with wavelength, following the well-known $\lambda^{-\alpha}$ law (where α is 4.3 near 300 nm), RRS, which contributes ~ 3.5 % to the total scattering, introduces a complex structure in the buv

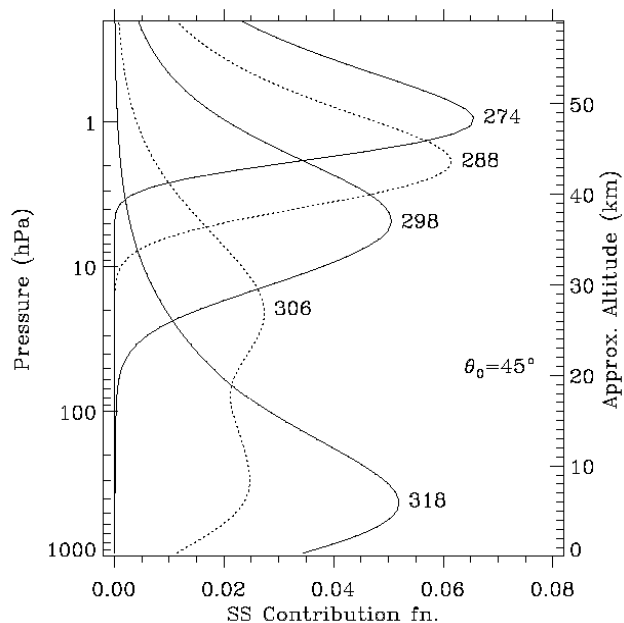


Figure 1-2: Radiance Contribution Functions

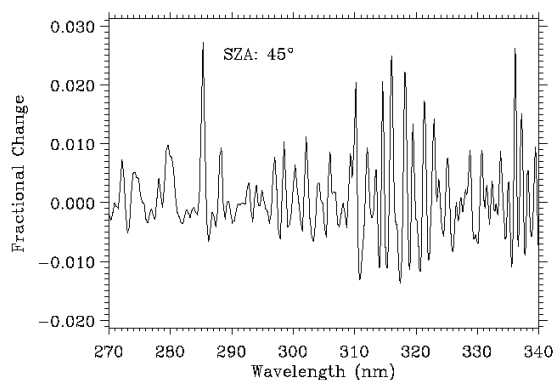


Figure 1-3: Fractional change in buv radiance due to Ring Effect

spectrum by filling-in (or depleting) structures in the atmospheric radiation, producing the so-called Ring Effect [Grainger & Ring, 1962] (Fig. 1-3). The most prominent structures in buv radiation are those due to solar Fraunhofer lines, however, structures produced by absorption by ozone and other molecules (principally volcanic SO₂) in the earth's atmosphere are also altered by RRS. (Vibrational Raman scattering from water molecules can also produce the Ring effect. Though this effect is insignificant below 340 nm, it can be important at longer wavelengths.) Radiative transfer codes have been developed recently [Joiner et al., 1995; Vountas et al., 1998; Spurr, 2002] that calculate the effect of gaseous absorption, surface reflection and multiple scattering on the Ring signal. A key results of these models is that below 340 nm the RRS filling-in varies significantly with slant ozone column. It is necessary to account for this effect to keep radiative transfer errors in deriving total O₃ to <1%. Smaller but significant variations are caused by surface albedo, aerosols and clouds [Joiner & Bhartia, 1995]. No current algorithm accounts for these effects adequately though the errors in deriving total O₃ are likely to be small.

1.2.3. Trace Gas Absorption

Besides O₃, SO₂ can produce strong absorption in the 270-340 nm band. Fig. 1-4 shows that at some wavelengths, a molecule of SO₂ can have 4 times stronger absorption than a molecule of O₃. However, the background vertical column density (VCD) of SO₂ in the atmosphere is very small (less than 0.1% of ozone), and most of it is the boundary layer where, because of shielding by molecular scattering, the absorption by a molecule of SO₂ reduces by a factor of 5-10 from that shown in Fig. 1-4. For this reason, even localized enhancements of boundary layer SO₂ due to industrial emission, which can increase VCDs by a factor of 10 or more, are difficult to detect in the buv radiance. However, episodic injection of SO₂ by volcanic eruptions can produce VCDs from 10% of total ozone to more than twice the total ozone [Krueger, 1983; McPeters et al., 1984], thus greatly perturbing the buv radiances.

As shown in Fig. 1-5, on a per molecule basis, NO₂ has a much stronger absorption than O₃ at wavelengths longer than 310 nm. However, the VCD of NO₂ in the atmosphere is about 3000 times smaller than O₃, so the NO₂ absorption becomes important only at wavelengths longer than 325 nm, where the NO₂ absorption exceeds 1% of the O₃ absorption. (Like SO₂, boundary layer NO₂ has 5 to 10 times smaller effect.)

1.2.4. Cloud Scattering

Clouds produce two important effects. First, they alter the spectral dependence of the buv radiation. Though Mie scattering in the clouds is inherently wavelength independent in UV, the effect of clouds on buv radiation is strongly wavelength-dependent. At longer wavelengths this is because in absence of clouds the upwelling radiation from the atmosphere is strongly wavelength dependent due to Rayleigh scattering. As the amount or thickness of clouds in a pixel increases, the spectral dependence

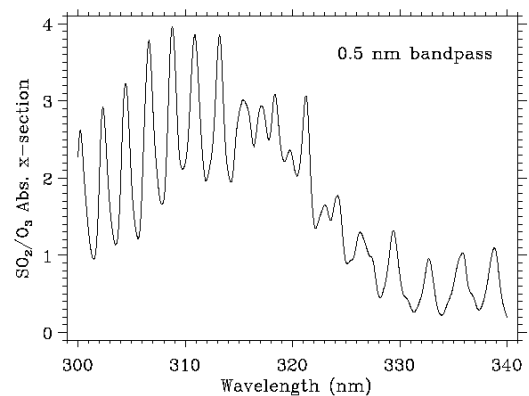


Figure 1-4: Ratio of SO₂ to O₃ absorption cross-section

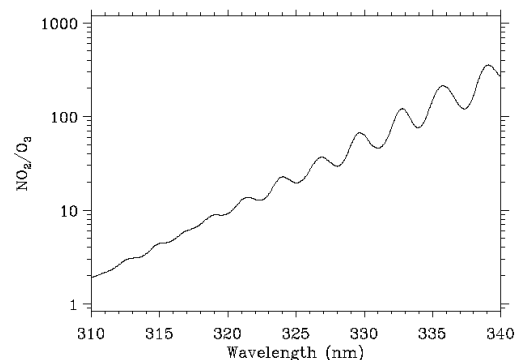


Figure 1-5 Ratio of NO₂ to O₃ absorption cross-section

of radiation is reduced, as seen in Fig 1-6. (The figure shows top-of-the-atmosphere reflectance which is proportional to the upwelling radiation.) At shorter wavelengths ozone controls what fraction of the radiation reaches the cloud altitude. Thus, while tropospheric clouds have no effect on buv radiation at $\lambda < 295$ nm, PSCs and PMCs do. At longer wavelengths, cloud effect rapidly increases, becoming as large as 90% of the total radiation at 335 nm when deep convective clouds are present.

The second effect of the cloud is that it alters the absorption of buv radiation by ozone (as well as UV-absorbing aerosols, tropospheric NO_2 , and SO_2 , when they are present). Absorption below the cloud layer is reduced while the absorption inside and

above the clouds is enhanced. These effects are complex: a function of cloud optical thickness, its geometrical thickness (which determines the amount of absorbers inside the cloud), height and surface albedo, and, of course, wavelength and observation geometry. Fortunately, these effects are usually small, for there is little O_3 or SO_2 in the troposphere, except in highly polluted conditions. However, thick PSCs and PMCs in the upper atmosphere can introduce large errors [Torres et al., 1992; Thomas, 1995].

1.2.5. Aerosol Scattering

Though the effect of aerosol scattering on buv radiation is usually small compared to the effect of clouds (with the exception of stratospheric aerosols produced after some volcanic eruptions), this effect can be surprisingly complex [Torres et al., 1998] depending both on their

macrophysical properties (vertical distribution, and optical depth) as well as their microphysical properties (size distribution and refractive index). Fig. 1-7 shows how 3 different aerosol types affect buv radiance at the ozone-absorbing wavelengths. (Tropospheric aerosols have little effect below 300 nm.). The solid line in Fig. 1-7 represents the case for most common type of aerosols found around the globe. These aerosols contain sea-salt and sulfate and have low levels of soot. Their effect on buv radiance is very similar to that from low level clouds, so they usually require no special consideration. However, aerosols that absorb UV radiation, e.g., continental aerosols containing soot (dotted line), carbonaceous aerosols (smoke) produced by biomass burning (not shown), and mineral dust (dashed line) from the deserts reduce the UV radiation passing through them, so they cause the underlying surface (including clouds) to appear darker. If a layer of UV-absorbing aerosols is above a dark surface, the amount of radiation they absorb is strongly dependent on the layer altitude, the higher the aerosol the larger the effect. Sometimes, it is assumed that the effect of aerosols on buv radiation is a simple linear (or quadratic) function of wavelength. However, as shown in Fig. 1-7, this assumption is not valid at wavelengths below 310 nm; even at longer

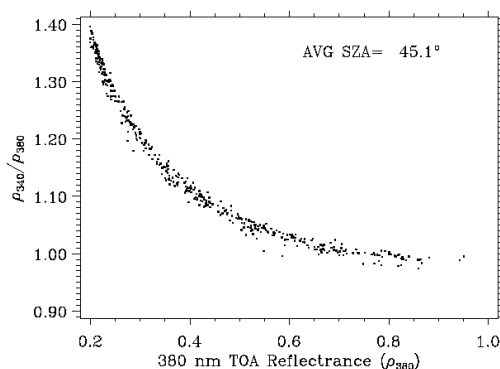


Figure 1-6: Ratio of 340/380 TOA reflectance vs. 380 reflectance observed by TOMS

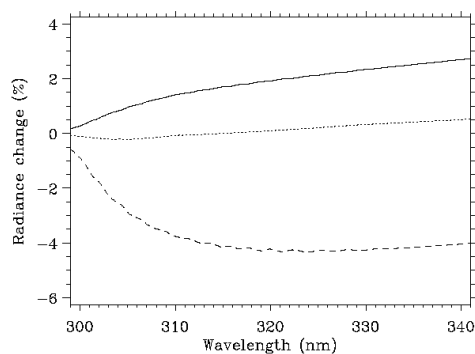


Figure 1-7: Effect of aerosols on buv radiances. (25° solar ZA, nadir view, optical depth at 550 nm: 0.15, marine, aerosol: solid line, continental: dotted line, dust: dashed line.)

and mineral dust (dashed line) from the deserts reduce the UV radiation passing through them, so they cause the underlying surface (including clouds) to appear darker. If a layer of UV-absorbing aerosols is above a dark surface, the amount of radiation they absorb is strongly dependent on the layer altitude, the higher the aerosol the larger the effect. Sometimes, it is assumed that the effect of aerosols on buv radiation is a simple linear (or quadratic) function of wavelength. However, as shown in Fig. 1-7, this assumption is not valid at wavelengths below 310 nm; even at longer

wavelengths, a layer of thick aerosols can modify trace gas absorption, just like clouds, i.e., the gaseous absorption above and inside the aerosol layer is enhanced while the absorption below the layer is reduced. This effect must be taken into account for accurate retrievals in highly polluted conditions.

A notable exception is stratospheric aerosol produced after high altitude volcanic eruptions. Stratospheric aerosols of relatively small optical thickness ($\tau \sim 0.1$) can markedly alter the ozone absorption of the buv radiation [Bhartia *et al.*, 1993, Torres & Bhartia, 1995; Torres *et al.*, 1995], increasing the absorption at some wavelengths, decreasing it at other wavelengths. One needs accurate knowledge of the aerosol vertical distribution to account for these effects. It is expected that such information would be available from the HIRDLS instrument on EOS Aura.

1.2.6. Surface Reflection

The reflectivity of the Earth's surface in UV is usually quite small [Eck *et al.*, 1987; Herman & Celarier, 1997]. Even over deserts, where the visible reflectivity can be quite high, the UV reflectivity remains below 10%. It exceeds 10% only in presence of sea-glint, snow and ice. More importantly, to the best of our knowledge, the UV reflectivity doesn't vary with wavelength significantly enough to alter the spectral dependence of the buv radiation. An important exception is the sea-glint. Since the reflectivity of the ocean, when viewed in the glint (geometrical reflection) direction, is very different for direct and diffuse light (exceeding 100% for direct when the ocean is calm, but only 5% for diffuse), in UV, where the ratio of diffuse to direct radiation has a strong spectral dependence, the ocean appears "red", i.e., it gets brighter as wavelength increases. The reflectivity of the ocean at any wavelength, as well as its spectral dependence, is a strong function of wind speed, and of course, aerosol and cloud amount. Accurate retrieval in presence of sea glint requires that one account for these complex effects.

1.3. References

- Bhartia, P. K., J. R. Herman, R. D. McPeters and O. Torres, Effect of Mount Pinatubo Aerosols on Total Ozone Measurements From Backscatter Ultraviolet (BUV) Experiments, *J. Geophys. Res.*, 98, 18547-18554, 1993.
- Bhartia, P. K., R. D. McPeters, C. L. Mateer, L. E. Flynn, and C. Wellemeyer, Algorithm for the Estimation of Vertical Ozone Profile from the Backscattered Ultraviolet (BUV) Technique, *J. Geophys. Res.*, 101, 18793-18806, 1996.
- Chance, K., and R. J. D. Spurr, Ring Effect Studies: Rayleigh Scattering, Including Molecular Parameters for Rotational Raman Scattering, and the Fraunhofer Spectrum, *Applied Optics* 36, 5224-5230, 1997.
- Eck, T. F., P. K. Bhartia, P. H. Hwang, and L. L. Stowe, Reflectivity of the Earth's Surface and Clouds in Ultraviolet from Satellite Observations, *J. Geophys. Res.*, 92, 4287, 1987.
- Grainger, J. F. and J. Ring, Anomalous Fraunhofer line profiles, *Nature*, 193, 762, 1962.
- Herman, J. R., and E. A. Celarier, Earth surface reflectivity climatology at 340-380 nm from TOMS data, *J. Geophys. Res.*, 102, 28003-28011, 1997.
- Joiner, J., P. K. Bhartia, R. P. Cebula, E. Hilsenrath, R. D. McPeters, and H. W. Park, Rotational-Raman Scattering (Ring Effect) in Satellite Backscatter Ultraviolet Measurements, *Appl. Opt.*, 34, 4513-4525, 1995.
- Joiner, J. and P. K. Bhartia, The Determination of Cloud Pressures from Rotational-Raman Scattering in Satellite Backscatter Ultraviolet Measurements, *J. Geophys. Res.*, 100, 23019-23026, 1995.

- Kattawar, G. W., A. T. Young, and T. J. Humphreys, Inelastic scattering in planetary atmospheres. I. The Ring Effect, without aerosols, *Astrophys. J.*, 243, 1049-1057, 1981.
- Krueger, A.J., Sighting of El Chichon Sulfur Dioxide with the Nimbus-7 Total Ozone Mapping Spectrometer, *Science*, 220, 1377-1378, 1983.
- McPeters, R. D., D. F. Heath, and B. M. Schlesinger, Satellite observation of SO₂ from El Chichon: Identification and Measurement, *Geophys Res. Lett.*, 11, 1203-1206, 1984.
- McPeters, R. D., Climatology of Nitric Oxide in the upper stratosphere, mesosphere, and thermosphere: 1979 through 1986, *J. Geophys. Res.*, 94, 3461-3472, 1989.
- Spurr, R. J. D., Discrete ordinate theory in a stratified medium with first order Raman scattering: a general quasi-analytic solution, in preparation, 2002.
- Thomas, G. E., Solar Mesosphere Explorer measurements of polar mesospheric clouds (noctilucent clouds). *J. Atmos. Terr. Phys.*, 46, 819-824, 1984.
- Thomas G. E., Climatology of polar mesospheric clouds: Interannual variability and implications for long-term trends, Geophysical Monograph 87, AGU, 1995.
- Torres, O., Z. Ahmad and J. R. Herman, Optical effects of polar stratospheric clouds on the retrieval of TOMS total ozone, *J. Geophys. Res.*, 97, 13015-13024, 1992.
- Torres, O. and P. K. Bhartia, Effect of Stratospheric Aerosols on Ozone Profile from BUV Measurements, *Geophys. Res. Lett.*, 22, 235-238, 1995.
- Torres, O., J. R. Herman, P. K. Bhartia, and Z. Ahmad, Properties of Mt. Pinatubo Aerosols as Derived from Nimbus-7 TOMS Measurements, *J. Geophys. Res.*, 100, pp. 14,043-14,056, 1995.
- Torres, O., P. K. Bhartia, J. R. Herman, Z. Ahmad, and J. Gleason, Derivation of aerosol properties from satellite measurements of backscattered ultraviolet radiation: Theoretical basis, *J. Geophys. Res.*, 103, 17,099-17,110, 1998.
- Vountas, M., V. V. Rozanov and J. P. Burrows, Ring Effect: Impact of rotational Raman scattering on radiative transfer in Earth's Atmosphere, *Journal of Quantitative Spectroscopy and Radiative Transfer*, 60, 943-961, 1998.
- Young, A. T., Rayleigh Scattering, *Appl. Opt.*, 20, 533-535, 1981.

2. TOMS-V8 Total O₃ Algorithm

Pawan K. Bhartia¹ & Charles W. Wellemeyer²

¹NASA Goddard Space Flight Center, Greenbelt, Maryland, USA

²Science Systems & Applications, Inc., Lanham, Maryland, USA

2.1. Overview

The TOMS-V8 total ozone algorithm is the most recent version of a series of buv (backscattered ultraviolet) total ozone algorithms that have been developed since the original algorithm proposed by Dave and Mateer [1967], which was used to process Nimbus-4 BUUV data [Mateer et al., 1971]. These algorithms have been progressively refined [Klenk et al., 1982; McPeters et al., 1996; Wellemeyer et al., 1997] with better understanding of UV radiation transfer, internal consistency checks, and comparison with ground-based instruments. However, all algorithm versions have made two key assumptions about the nature of the buv radiation that have largely remained unchanged over all these years. First assumption is that the buv radiances at wavelengths greater than 310 nm are primarily a function of total ozone amount, with only a weak dependence on ozone profile that can be accounted for using a set of climatological profiles. Second assumption is that a relatively simple radiative transfer model that treats clouds, aerosols, and surfaces as Lambertian reflectors can account for most of the spectral dependence of buv radiation, though corrections are required to handle special situations. The recent algorithm versions have incorporated procedures for identifying these special situations, and apply a semi-empirical correction, based on accurate radiative transfer models, to minimize the errors that occur in these situations. The primary difference between the TOMS-V8 and its OMI version would be that these diagnostics and correction procedures can be improved by taking advantage of OMI's hyperspectral capability. This will be particularly useful in identifying instrumental errors, particularly slowly developing calibration drifts [Joiner & Bhartia, 1997].

In the following sections we will describe the forward model used to calculate the top-of-the-atmosphere (TOA) reflectances, the inverse model used to derive total ozone from the measured reflectances, a summary of errors, and the validation plan

2.2. Forward Model

The TOMS forward model, called TOMRAD, is based on successive iteration of the auxiliary equation in the theory of radiative transfer developed by Dave [1964]. This elegant solution accounts for all orders of scattering, as well as the effects of polarization, by considering the full Stokes vector in obtaining the solution. Though the solution is limited to Rayleigh scattering only and can only handle reflection by Lambertian surfaces, the original Dave code, written more than 3 decades ago, is still one of the fastest radiative transfer codes that is currently available to solve such problems. With the modifications that have been incorporated into the code over the years, it is also one of the most accurate. The modifications include a pseudo-spherical correction (in which the incoming and the outgoing radiation is corrected for changing solar and satellite zenith angle due to Earth's sphericity but the multiple scattering takes place in plane parallel atmosphere), molecular anisotropy [Ahmad & Bhartia, 1995], and rotational Raman scattering [Joiner et al., 1995]. Comparison with a full-spherical code indicates that the pseudo-spherical correction is accurate to 88° solar zenith angle [Caudill et al., 1997]. The current version of the code can handle multiple molecular absorbers, and accounts for the effect of atmospheric temperature on molecular absorption and of Earth's gravity on the Rayleigh optical depth. In the following we describe the various inputs and outputs of this code.

2.2.1. Spectroscopic Constants

The Rayleigh scattering cross-sections and molecular anisotropy factor used are based on Bates [1984], while the ozone cross-sections and their temperature coefficients are based on Bass and Paur [1984]. The forward model also accounts for O₂-O₂ absorption, which is based on Greenblatt et al. [1990].

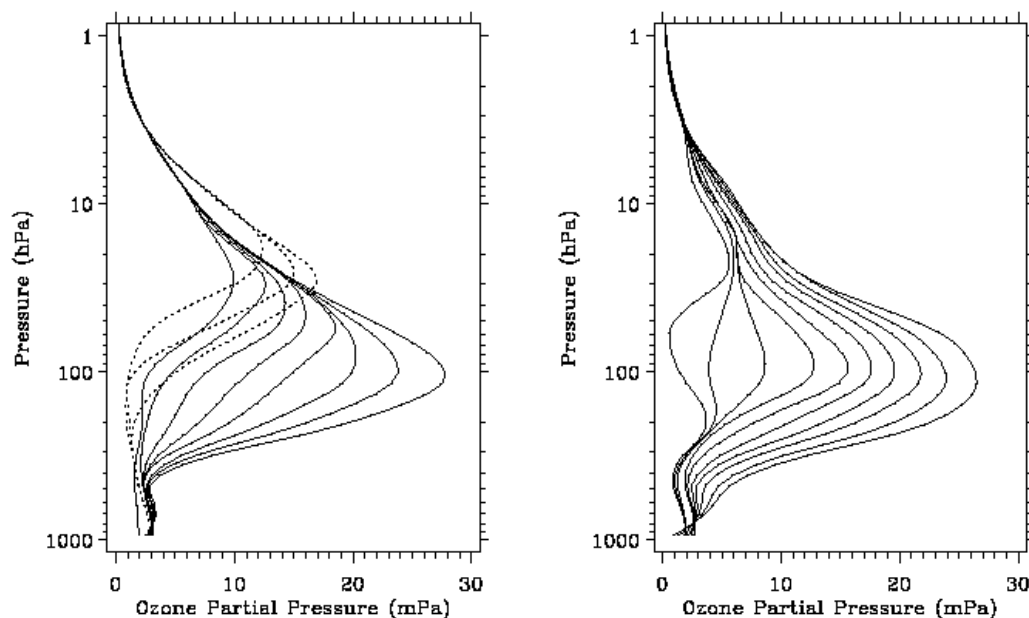


Figure 2-1: Total O₃-dependent standard profile used for generating the radiance table. Left panel shows 3 low latitude profiles (dotted lines) and 8 mid latitude profiles. Right panel shows the 10 high latitude profiles.

2.2.2. Ozone and Temperature Profiles

In general, the buv radiation at any wavelength is a function of O₃ and temperature profile. Though at 317.5 nm, which is used to derive total O₃ in the TOMS V8 algorithm, these effects are usually quite small, they must be accounted for if high accuracy in deriving total O₃ is required. The empirical orthogonal analysis of the ozonesonde data [Wellemeyer et al., 1997] shows that the largest variation in ozone profile occurs in the lower stratosphere (10-20 km), and that these variations are highly correlated with total O₃. By contrast, the tropospheric (0-10 km) and upper stratospheric (20-40 km) O₃ density shows weak correlation with total O₃, but varies with season and latitude. Recognizing this, the TOMS V8 algorithm uses a 3-dimensional dataset of ozone profiles to compute total O₃, consisting of profiles that vary with total O₃, latitude and month. These profiles are constructed by combining two 2-dimensional datasets described below.

The first dataset consists of 21 ozone profiles (called standard profiles) that vary with total ozone and latitude. These profiles have been generated using ozonesonde data below 25 km and SAGE satellite data above. These data are first integrated to obtain ozone amounts in ten (~4.8 km thick) layers, equally spaced in logp with spacing of log2, extending from 1 atm (1013.25 hPa) to 2⁻¹⁰ atm. (This smoothes out any high resolution structures that might occur when there are not enough data points to average.) A top layer that extends to infinity is then added by linear extrapolation of the logarithm of the ozone in the upper two layers with logp (which amounts to assuming that the ratio of O₃ to atmospheric scale height in the top layer is

constant). The layer ozone values are binned two-dimensionally, in 50 DU total ozone bins, and 30° latitude bins, with data from both hemispheres combined, to get 3 profiles for low latitudes (30S-30N) containing 225-325 DU, 8 for mid latitude (30-60) containing 225-575 DU, and 10 for high latitude (60-pole) containing 125-575 DU. The O₃ partial pressure profiles reconstructed from the layer ozone amounts are shown in Fig. 2-1. They capture the well-known features of the ozone vertical distribution, that in a given latitude band the ozone peak and the O₃ tropopause get lower as total ozone increases, and for a given total ozone they get lower as one moves to higher latitude. Empirical orthogonal function analysis shows that the standard profiles capture the first two eigen functions of the ozone profile covariance matrix, and explain about 80% of the variance of the layer O₃ amounts [Wellemeier et al., 1997]. The second dataset consists of more traditional O₃ and temperature profiles constructed by Logan, Labow & McPeters [unpublished] by binning ozonesonde and satellite data in 12 monthly and 18 latitude (each 10° wide) bins.

The 3-dimensional profiles are constructed by combining these two datasets in such a way that in the part of the atmosphere where total O₃ is a good predictor of O₃ profile the first dataset prevails while in the rest of the atmosphere the 2nd data set prevails. This results in 1512 profiles, 12n profiles in each of the 18 latitude bins, where n is 3 in low latitudes (30S-30N), 8 in mid latitude (30°-60°), and 10 in high latitudes (60°-90°), containing the same total O₃ as in the first dataset. These profiles are slightly different in the two hemispheres, primarily due to hemispherical asymmetry in the tropospheric O₃.

Figure 2-2 shows scatter plots comparing layer ozone amounts measured by the Hohenpeissenberg ozonesonde station with the 96 profile subset of the 3D profiles at that latitude. In layers 2-4 the correlation between the two are ~85%. Table 2-1 shows the variation reduction and residual standard deviation with this station and the SAGE satellite data at 50°N. The residual standard deviation in all layers is less than 10 DU. Similar results are obtained at other latitudes.

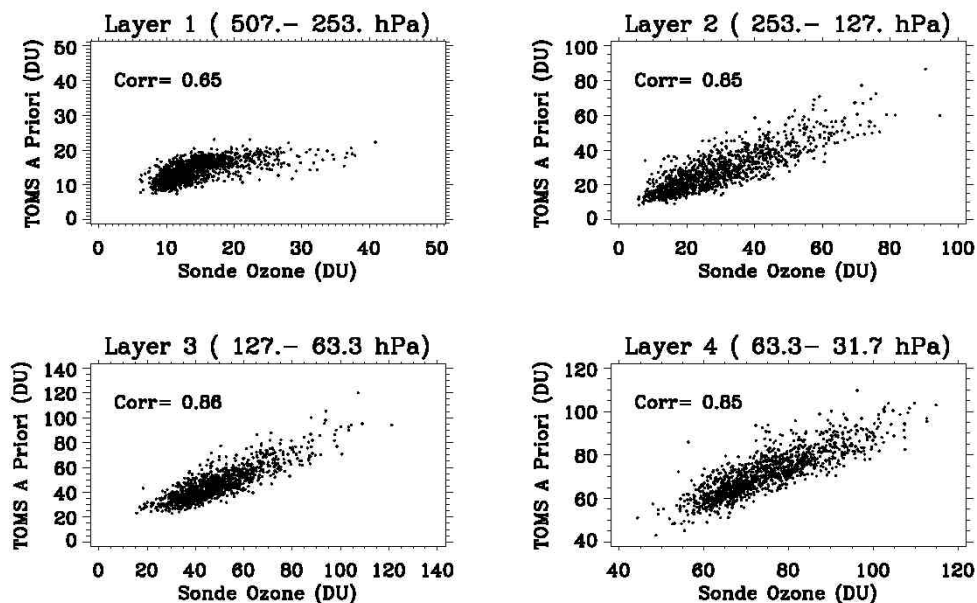


Figure 2-2: Comparison of the profiles uses by the TOMS V8 algorithm as a priori for total O₃ retrieval and the data taken by the Hohenpeissenberg ozonesonde station in Germany (47°N).

Table 2-1: Comparison of *A Priori* profiles with ozonesonde and SAGE

Layer No	Layer midpoint (~km)	Hohenpeissenberg		SAGE @50°N	
		Variance reduction (%)	Residual std dev (DU)	Variance reduction (%)	Residual std dev (DU)
0	2.8	41	2.9	-	-
1	7.7	42	3.8	-	-
2	12.5	73	7.6	75	9.7
3	17.0	74	7.4	83	8.9
4	21.3	73	6.0	77	6.4
5	25.8	24	5.5	29	5.3
6	30.4	42	3.5	35	4.3
7	35.2	-	-	39	1.9
8	40.2	-	-	28	1.0
9	45.5	-	-	40	0.5

2.2.3. Radiance Computation

To minimize computer time, the TOA radiances are computed by interpolation and adjustment of a pre-computed radiance table, which is created using the TOMRAD radiative transfer code. This table consists of 5 variables: I_0 , I_1 , I_2 , I_R and S_b . Using these 5 variables one can calculate the TOA radiance I , using the following formula:

$$I = I_0(\mathbf{q}_0, \mathbf{q}) + I_1(\mathbf{q}_0, \mathbf{q}) \cos \mathbf{f} + I_2(\mathbf{q}_0, \mathbf{q}) \cos 2\mathbf{f} + \frac{RI_R(\mathbf{q}_0, \mathbf{q})}{(1 - RS_b)} \quad [2-1]$$

where, the first three terms together constitute the purely atmospheric component of the radiance, unaffected by the surface. This component, which we will refer to as I_a , is a function of solar zenith angle θ_0 , satellite zenith angle θ , and ϕ , the relative azimuth angle between the plane containing the sun and local nadir at the viewing location and the plane containing the satellite and local nadir. The last term provides the surface contribution, where, RI_R is the once-reflected radiance from a Lambertian surface of reflectivity R , and the factor $(1 - RS_b)^{-1}$ accounts for multiple reflections between the surface and the overlying atmosphere. Note that this factor can enhance the effect of absorbers that may be present just above a bright surface, e.g., tropospheric ozone, O_2-O_2 , UV-absorbing aerosols, and SO_2 . The tables are computed for 10 solar zenith angles, 6 satellite zenith angles, and 4 surface pressures, which have been selected such that the interpolation errors in the computed radiances are $<0.1\%$.

Since TOMRAD calculates only the elastic scattering component of the TOA radiance, a correction for the inelastic Rotational Raman scattering (RRS), discussed in Section 1.2.2, is applied. The inelastic scattering fills-in any absorption lines that may be present in the incoming radiation. Typically this consists of solar Fraunhofer lines, but absorption lines introduced by the Earth's atmosphere itself are also filled-in by RRS (telluric effect). The telluric filling-in, which increases with the slant column of the molecular absorbers in the path of the radiation, is more serious for it produces an apparent reduction in the molecular absorption that one wants to measure. We use a radiative transfer program recently developed by Spurr [2002] to create a table of correction to Eq.[2-1]. Though the corrections to radiances are typically less than 1%, if not corrected, they can produce several percent error in total O_3 .

To compute the radiance for an arbitrary O_3 and temperature profile, the following two-step procedure is used. It takes advantage of the fact that the TOA radiance at a wavelength

longer than 310 nm is largely determined by the integrated total O₃ amount rather than by the shape of the profile. Variations in the shape of the O₃ profile and in the atmospheric temperature produce second order effects that are corrected by first order Taylor series expansion. This procedure is described below.

The basic radiance tables are computed using the 21 standard profiles (described in Section 2.2.2), and then by perturbing each of these profiles by 10% in each of the 10 layers respectively. A nominal global average temperature profile is used. To compute the TOA radiance for a given O₃ and temperature profile and its latitude, we first interpolate (or in rare cases, extrapolate) in the radiance table based only on total O₃ and latitude of the profile. Then we correct the interpolated radiance for the difference between the assumed O₃ and temperature profile (x₀, T₀) used in constructing the radiance table and the given profile (x,T), as follows:

$$\ln I(x, T) = \ln I(x_0, T_0) + \sum_{l=0}^9 \left. \frac{\partial \ln I}{\partial x_l} \right|_{x_0, T_0} (x - x_0)_l + \sum_{l=0}^9 \left. \frac{\partial \ln I}{\partial \mathbf{s}_l} \right|_{x_0, T_0} [\mathbf{s}(T) - \mathbf{s}(T_0)] \quad [2-2]$$

where, $\sigma(T)$ is the ozone absorption cross-section at temperature T, and l is the layer number. The two Jacobians in the above equation can be reduced to one by noting that a fractional change in O₃ absorption cross-section in a layer produces the same effect on radiance as the same fractional change in layer O₃, i.e., $\partial \ln I / \partial \log \mathbf{s}_l = \partial \ln I / \partial \log x_l$. Applying this identity one gets,

$$\ln I(x, T) = \ln I(x_0, T_0) + \sum_{l=0}^9 \left. \frac{\partial \ln I}{\partial x_l} \right|_{x_0, T_0} (x - x_0)_l + \sum_{l=0}^9 \left. \frac{\partial \ln I}{\partial x_l} \right|_{x_0, T_0} \frac{x_l}{\mathbf{s}_l} [\mathbf{s}(T) - \mathbf{s}(T_0)] \quad [2-3]$$

The Jacobian is calculated by differencing the radiances calculated using the perturbed and unperturbed standard profiles. Calculations using sonde and satellite profiles show that [2-3] allows one to calculate TOA radiance at any buv wavelength longer than 310 nm to few tenths of a percent accuracy (compared to the direct TOMRAD calculation). This not only allows one to rapidly compute the radiances for the 1512 profile dataset used by the operational TOMS algorithm, but also allows for future incorporation of profiles from external sources, e.g., data assimilation, to improve accuracy.

2.2.4. Accounting for aerosol and clouds

The forward model doesn't account for aerosols explicitly; aerosols are treated as part of the reflecting surface. Aerosols usually increase the apparent reflectivity of the surface, though desert dust, which strongly absorbs the UV radiation, can have an opposite effect. Dave [1978] noted that aerosols usually make the effective reflectivity wavelength dependent, even when the true surface is not. Though for common aerosol types (sea-salt, sulfates etc.) this effect is usually quite small, a thick layer of smoke or desert dust at several km altitude can cause the apparent reflectivity of the surface to decrease non-linearly with wavelength. This is caused by the absorption of Rayleigh-scattered radiation emanating from below the aerosol layer by these aerosols. Section 2.3 discusses how the inverse model accounts for these effects.

The forward model treats a cloud as an opaque Lambertian surface. Transmission through and around clouds is accounted for by a mixed-Lambertian surface model, in which the TOA radiance I is written as:

$$I = I_s(R_s, p_s)(1 - f_c) + I_c(R_c, p_c)f_c \quad [2-4]$$

where, I_s represents radiance from the clear portion of the scene, containing a Lambertian surface of reflectivity R_s at pressure p_s; and I_c similarly represents the cloudy portion, and f_c is the cloud fraction. As discussed by Ahmad et al. [2002], this model agrees reasonably well with plane-

parallel Mie scattering cloud model and reproduces the spectral dependence of the TOA radiance in the UV, provided one sets R_c equal to 0.80, and derives f_c from the measurements at a non-ozone-absorbing wavelength (rather than from external sources). However, since typical clouds have an albedo of ~ 0.40 , f_c thus derived should be thought as radiative (effective) cloud fraction, rather than the geometric cloud fraction.

2.2.5. Cloud height and surface pressure

To compute the radiances using [2-3] one also needs the surface pressure p_s and the effective cloud pressure p_c (defined as the pressure from which the cloud-scattered radiation appears to emanate). Surface pressure is obtained by converting a standard terrain height data base using US standard temperature profiles. The surfaces are also flagged as containing snow/ice using a climatological database.

We expect that the effective cloud pressure would be derived using the O_2 - O_2 absorption bands and/or from the Ring Effect. These algorithms are described in a separate ATBD.

2.3. Inverse Algorithm

The basic TOMS V8 algorithm uses just two wavelengths to derive total O_3 : a weakly-absorbing wavelength (331.2 nm) to estimate an effective surface reflectivity (or effective cloud fraction), and another wavelength (317.5 nm) with stronger O_3 absorption to estimate ozone. One makes the implicit assumption that the effective reflectivity or the cloud fraction has no significant variation between 331.2 and 317.5 nm.

As is typically the case with inverse remote sensing algorithms, the solution requires *a priori* constraints. This constraint is set by the 1512 profile dataset that are described in Section 2.2.2. For a given latitude and month this dataset provides between 3 to 10 profiles that vary with total O_3 , which allow one to construct a unique mathematical relationship between the TOA radiance at 317.5 nm and total O_3 . Conceptually, this constraint is very similar to that one applies in optimal estimation methods [Rodgers, 2000], except that instead of imposing the constraint through a mean *a priori* profile and an associated covariance matrix one constructs a set of *a priori* profiles (that vary with total O_3) to constrain the solution. We have verified that the two methods give virtually identical results when one uses one wavelength to derive one quantity (total O_3). Optimal estimation using additional wavelengths of TOMS didn't show noticeable improvement so we have decided to stay with the simpler of the two methods for now. However, we are continuing to study this problem using the GOME data. Switching to multi-wavelength optimal estimation method would be relatively simple since all the necessary tools are already in place (a fast and accurate forward model and the Jacobians).

Though the results from the basic 2-wavelength algorithm are usually quite good (rms error $< 2\%$), large errors can occur in special situations. These situations are identified by the analysis of residuals (difference between the measured and computed radiances), and a correction is applied assuming a relationship between the residuals and error in derived total O_3 . In Section 2.3.1 we discuss the basic algorithm, and in Section 2.3.2 we discuss the corrections to the basic algorithm.

2.3.1. Basic Algorithm

As noted above, the basic algorithm uses two wavelengths to derive two quantities. This procedure is described below.

Computation of Effective Reflectivity/Cloud Fraction

One calculates the effective reflectivity of the scene by inverting Eq. **Error! Reference source not found.** The inverse equation is:

$$R = \frac{(I_m - I_a)}{[I_R + S_b(I_m - I_a)]} \quad [2-5]$$

where, I_m is the measured radiance, and I_a and I_R are calculated using terrain or sea-surface pressure. If $R < 0.15$ the algorithm assumes that there are no clouds present, otherwise one estimates an effective cloud fraction f_c by inverting [2-4], which gives,

$$f_c = (I_m - I_s) / (I_c - I_s) \quad [2-6]$$

where I_s and I_c are computed using [2-1] assuming $R_s = 0.15$ and $R_c = 0.8$. If f_c exceeds one we assume that the surface contribution to the radiance is zero, and an effective cloud reflectivity is then re-derived using [2-5] assuming the surface is at p_c .

Note that the surface is assumed to have a reflectivity of 15%, even though UV reflectivity of most surfaces (not covered with snow/ice) is between 2-8% [Eck et al., 1987; Herman & Celarier, 1997]. A larger value is used to account for haze, aerosols, and fair-weather cumulus clouds that are frequently present over the oceans at very low altitudes. We believe that treating them as part of the surface rather than as part of (a higher-level) cloud offers the best strategy to minimize errors. However, the method may produce small errors when cirrus clouds are present. This error can be corrected if OMI cloud products are able to reliably separate low-level cumulus from cirrus. The algorithm also ignores clouds when the snow/ice flag is set, since radiative transfer calculations indicate that clouds effects are usually small under these conditions. This approach can also be modified if OMI cloud products prove reliable in separating snow/ice from clouds.

The algorithm also checks for sea-glint, which is detected by checking if the viewing angle is within a 15° cone of the geometrical reflection direction and by the fact that the surface appears much brighter at longer wavelengths (360 nm) than at shorter wavelengths (330 nm), for reasons discussed in Section 1.2.6. When sea-glint is detected sea-surface pressure is used for estimating effective reflectivity irrespective of its value.

TOMS V8 algorithm uses 331.2 nm wavelength to derive surface reflectivity at low solar zenith angles but switches to 360 nm when the ozone absorption at 331.2 nm becomes too large. Ozone correction is made by iteration, i.e., by starting with a nominal total O_3 estimate and then recalculating the reflectivity using total O_3 provided by the shorter wavelength. The process is repeated if reflectivity changes significantly. For OMI we propose to switch to 332.7 nm, which can be used everywhere for it has 3 times smaller O_3 absorption

Total O_3 computation

Using the above estimates of R or f_c , and the two-step radiance computation procedure described in Section 2.2.3, one can define a relationship between the 317.5 nm radiances and total using the *a priori* profiles. For a given latitude and month, the *a priori* profile dataset provides between 3 to 10 ozone profiles that vary with total O_3 , plus a temperature profile. The relationship between the logarithm of 317.5 radiance and total O_3 is slightly non-linear, so total O_3 corresponding to the measured radiance is estimated by piece-wise linear interpolation (or extrapolation).

In actual implementation, the 21 standard profiles are first used to derive an estimated total ozone Ω_0 . Then using this ozone (as well as month and latitude) a single profile x_{ap} is selected from the 1512 profile dataset, from which the adjustment to the radiance is calculated

using Eq. **Error! Reference source not found.** In most cases this adjustment to radiance is less than 2% of I_0 , but can reach up to 10% at 85° solar zenith angle. This correction leads to a new value of total O_3 , $\Omega_{ap} = \Omega_0 - (\ln I_{ap} - \ln I_0) \left/ \frac{\partial \ln I}{\partial \Omega} \right.$, where the partial derivative w.r.t. total ozone Ω is the slope the piece-wise curve calculated at Ω_0 .

Using the partial derivatives of the 317.5 nm radiance with respect to layer ozone, $\partial \ln I / \partial x$, we also compute the layer efficiency factors $h_l = \frac{\partial \ln I}{\partial x_l} \left/ \frac{\partial \ln I}{\partial \Omega} \right.$. It can be shown that η provides a relationship between the true total ozone, Ω , and the estimated total ozone, $\hat{\Omega}$, as follows:

$$\hat{\Omega} = \Omega - \sum_{l=0}^9 (1 - h_l)(x - x_{ap}) \quad [2-7]$$

where, x_{ap} is the *a priori* profile and x is the true profile. Note that the efficiency factor η is same as Rodgers' [2000] averaging kernel concept applied to total O_3 . In layers where η is significantly different from unity one has sensitivity to the *a priori* profile.

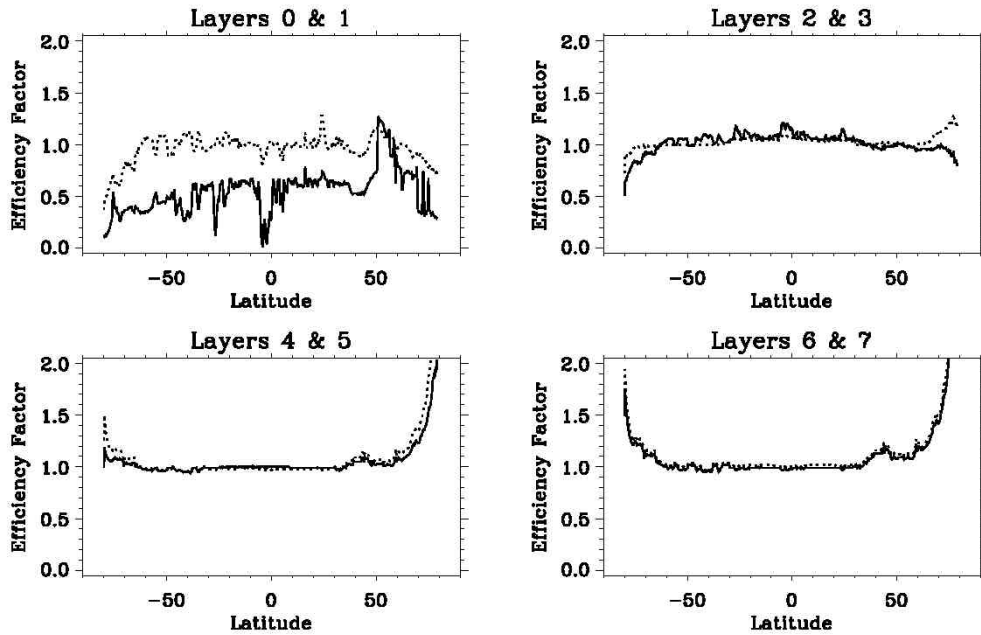


Figure 2-3: Layer efficiency factors for one day of TOMS data taken on March 20, 1979. Even numbered layers are shown as solid lines, odd numbered as dashed lines.

Fig. 2-3 shows how η of the nadir pixel varies with latitude for one orbit of TOMS data taken near the vernal equinox. Since TOMS was in a noon sun-synchronous orbit the latitude and solar zenith angles are nearly the same. One notes that except at high solar zenith angles η remains close to 1 in most layers except in layer 0. Variation in layer 0 is due to shielding of the lower troposphere by Rayleigh scattering and clouds. (Values greater than 1 can occur in presence of snow or low clouds.) At high solar zenith angles, η starts to become greater than 1 in the middle stratosphere, i.e., underestimation of O_3 in the upper layers can cause overestimation of total O_3 . Using [2-7] one can correct the estimated total O_3 if a better estimate of O_3 profile from an external source is available.

2.3.2. Corrections to the basic algorithm

Though, on a global basis, the basic algorithm provides total O₃ with rms error ~2%, large errors can occur in special situations. The following describes how such situations are identified and corrected using the radiance data at wavelengths not used by the basic algorithm.

Aerosols

TOMS data show very clearly that the apparent reflectivity of the Earth's surface derived from [2-7] has a strong wavelength dependence in presence of mineral dust and carbonaceous aerosols. Mie scattering calculations show that this is caused by the absorption of Rayleigh-scattered radiation as it passes through the aerosol layer. Since this scattering increases with decreasing wavelength, the apparent reflectivity of the surface (obtained by neglecting the aerosol absorption) decreases with wavelength. When one uses only two wavelengths to derive ozone, this absorption produces an effect that cannot be distinguished from ozone absorption, and hence one overestimates total ozone. TOMS V8 detects such aerosols by monitoring the ΔR at the two weakly-absorbing wavelengths (331.2 and 360 nm). When one uses the R derived from 331.2 nm to calculate radiance at 360 nm, the ΔR produces a positive residue (difference between measured and calculated radiance) at 360 nm when absorbing aerosols are present. By Mie scattering calculation, using various types of aerosols, Torres and Bhartia [1999] showed that a simple linear relationship between the residues and the ozone error exists. More detailed calculations show that the slope of this relationship varies with slant path ($\sec\theta_0 + \sec\theta$). The correction is applied using the tabulated value of these slopes. Calculations suggest that the residual errors in total O₃ are <1% except when aerosols load is extremely heavy ($\tau > 3$). The latter data are flagged.

Mie scattering calculations show that the non-absorbing aerosols can also produce residues, but for reasons that are more conventional. It is well known that the optical depth of aerosols consisting of small particles varies as λ^{-A} , where A is called the Ångstrom coefficient; for continental aerosols it is ~1.5 in the UV. This produces a greater increase in buv radiances (above the Rayleigh background) at shorter wavelengths than at longer wavelengths, thus producing ozone underestimation and a negative residue at 360 nm. However, compared to absorbing aerosols these effects are small. The correction procedure is similar to that for the absorbing aerosols.

Using the hyperspectral capability of OMI it is straightforward to test if the correction procedure described above works correctly. From Mie scattering calculations the effect of aerosols on the radiance should be a smooth but non-linear curve of the type shown in Figure 2-4. If the O₃ values have been properly corrected for the aerosols the residues should vary smoothly with wavelength in this manner and should not have the characteristic O₃ absorption structure of the Huggins band.

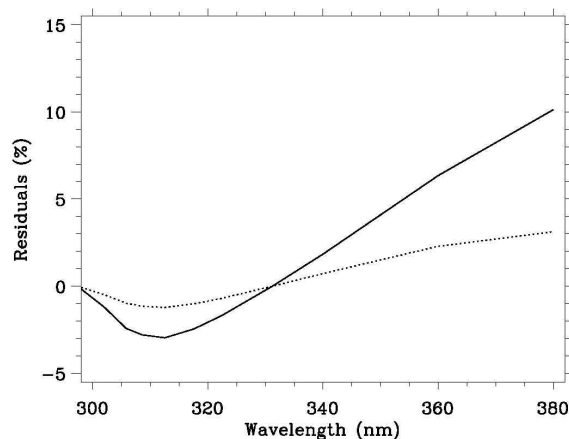


Figure 2-4: Radiance residuals produced by smoke of optical depth 1, at 3 km (solid line) and at 1 km (dashed line) altitudes.

Sea-Glint

As discussed in Section 1.2.6, the apparent reflectivity of the ocean in the UV in the glint direction (roughly a cone of $\pm 15^\circ$ from the geometrical reflection direction) varies with wavelength due to variation in the direct to diffuse ratio of the radiation falling on the surface. The magnitude of the sea-glint, and hence the $R-\lambda$ dependence it produces, decreases with increase in surface winds and by the presence of aerosols and clouds which also decrease the direct to diffuse ratio. Radiative transfer calculations [Ahmad & Fraser, private communication] show that, though the cause of the $R-\lambda$ dependence produced by sea-glint is quite different, its effect on ozone and residuals is similar to that for absorbing aerosols, and the same correction procedure also applies.

However, there is one aspect of sea-glint that is different from absorbing aerosols- the fact that they can significantly increase the apparent brightness of the surface and are easily confused with clouds. Since sea-glint increases the absorption of radiation by O_3 near the surface while clouds reduce the absorption, it is important to separate the two. TOMS V8 distinguishes clouds from sea-glint using the fact that clouds do not produce residues. However, if the OMI cloud products prove reliable in presence of sea-glint, this effect would be accounted for automatically using [2-6].

Ozone Profile

As noted above the total O_3 derived from the basic 2-wavelength algorithm is sensitive to the *a priori* profile; this sensitivity is captured by the efficiency factor η which is also reported along with the derived total O_3 . Examination of Fig. 2-3 shows that in most latitudes layer 0 is the primary source of error, though the error is small. A rough estimate of this error can be made by multiplying the average value of $1-\eta$ for layer 0 (~ 0.5) with the residual standard deviation of O_3 in this layer from Table 2-1 (2.9 DU), giving 1.5 DU rms error. However, larger errors can occur when η in the upper layers, particularly layer 6 and 7, starts to deviate from unity. These situations start to occur when the ozone slant column density (SCD), $\Omega \times (\sec\theta + \sec\theta_0)$, exceeds ~ 1500 DU. Study of ozone in the polar regions requires that the algorithm be able to derive reasonable total ozone values as close to the solar terminator as possible. At 80° solar zenith angle, the SCD can vary from less than 1000 DU to more than 4000 DU, and simply discarding data with very large SCD would seriously bias the zonal means. Therefore, it is important to design the algorithm such that reasonable total ozone values can be obtained for SCD of up to 5000 DU. Fig. 2-5 shows how a 10% error in the assumed profile between 4-32 hPa (representing roughly 1σ variation of ozone profile) affects the total ozone derived using the basic algorithm as a function of SCD.

Profile errors near 10 hPa can be detected by examining the residue at shorter buy wavelengths which are more sensitive to ozone profile than the wavelengths used for deriving total ozone. Fig. 2-6 shows how the 312.5 nm residue responds to the profile error assumed for Fig. 2-5. More detailed analysis of this error using a set of ozone profiles derived from high

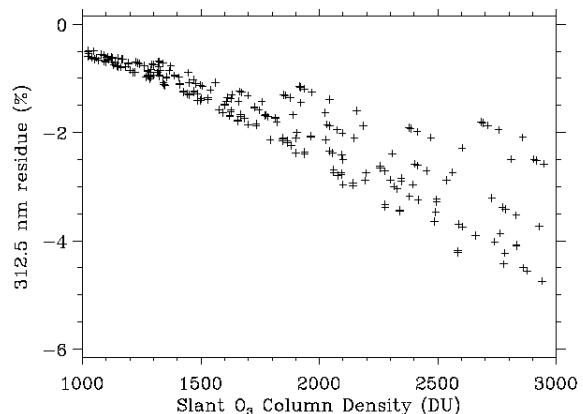


Figure 2-5: Error in retrieved total O_3 due to 10% excess ozone in 4-32 hPa layer than assumed. The data shown are for the full range of solar zenith angles, satellite zenith angles and total O_3 amounts that will be seen by OMI.

latitude ozonesondes indicates that a simple correction factor of 2.5 DU for 1% residue at 312.5 nm provides adequate correction to obtain reliable total ozone values (2%, 1σ) at SCDs of up to 3000 DU. However, the correction procedure becomes increasingly unreliable as the SCD exceeds 3000 DU.

Analysis indicates that it is possible to derive reliable total ozone values at even larger SCD values by doing optimal estimation of the ozone profile using a set of wavelengths. Though the procedure is similar to that described in Chapter 4, derivation of total ozone doesn't require wavelengths shorter than 310 nm. Also, since the residues and the Jacobian needed for optimal estimation have already been calculated, it is straightforward to extend the algorithm described in this chapter for this purpose.

Sulfur dioxide (SO₂)

As noted in Section 1.2.3, SO₂ has strong absorption in the wavelengths used for the estimation of total ozone. However, only volcanic SO₂ produces significant error in deriving total ozone. Figure 2-7 shows the residues produced by a layer of SO₂ at 7.4 km (solid line) and 2.5 km (dotted line) containing 2.6×10^{16} molecules/cm² (1 DU), which will produce respectively 2.5 DU and 1.3 DU errors in deriving total ozone using the TOMS V8 algorithm. It is clear, however, that such SO₂ amounts can be readily detected using residues in the wavelength range 305-310 nm, provided the OMI has adequate S/N at these wavelengths.

2.4. Error Analysis

Like any remote sensing technique, the TOMS V8 total O₃ algorithm is susceptible to three distinctly different types of error sources: 1) forward model errors, 2) inverse model errors, and 3) instrumental errors. The following sub-sections discuss these errors.

2.4.1. Forward Model Errors

The forward model errors include errors that occur in the computation of radiances. Since even the best radiative transfer models can only approximate the complex scattering and absorption processes of the real atmosphere, one inevitably has errors. Since the retrieval algorithm essentially uses the difference between the measured and calculated radiances to derive ozone, errors in forward model calculations have the same effect as similar errors in measured radiances. However, the two errors typically have very different spectral structure and they vary differently in space and time. So, their importance depends on how one plans to use the retrieved data. For example, many types of radiative transfer errors are unimportant for

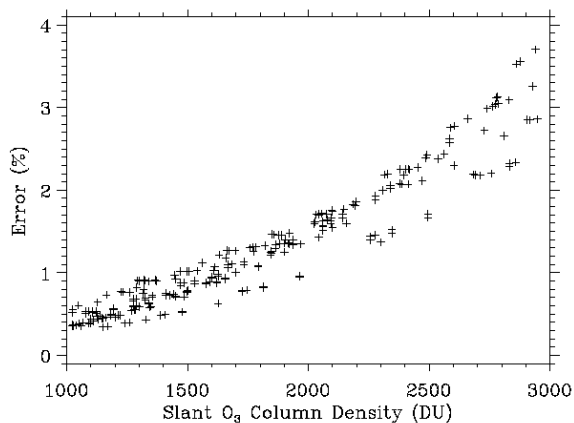


Figure 2-6: 312.5 nm residue for same profile error as in Fig. 2-5.

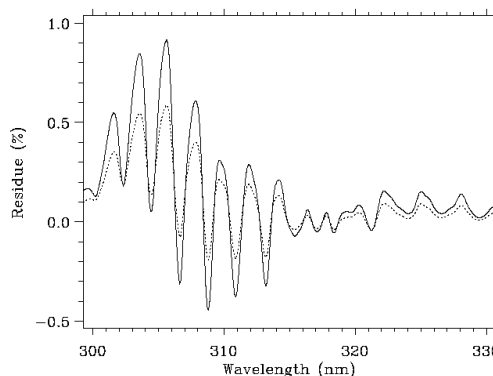


Figure 2-7: Residue caused by 1 DU of SO₂ column at 45° solar zenith angle, nadir view. Solid line for SO₂ layer at 7.4 km, dotted for 2.5 km.

determining long-term trend from a particular type of instrument, as long as the algorithm is kept the same, but they can be of vital importance in comparing two different measuring systems or algorithms. Following is a brief summary of the key forward model errors.

Radiative Transfer Code

The TOMRAD radiative transfer code, the work-horse of the TOMS algorithm, assumes that the atmosphere contains only molecular scatterers and absorbers bounded by opaque Lambertian surfaces. Radiation from these surfaces are linearly mixed to simulate the effect of clouds. Clearly, this scheme is an overly simplified treatment of many complex processes that occur in the real atmosphere, including Mie scattering by clouds and aerosols, scattering by non-spherical dust particles, and reflection by non-Lambertian surfaces. However, as discussed in the previous section, the key issue for determining total O₃ is not how well the radiative transfer code computes the radiance but how well it predicts the spectral dependence of radiance. This can be partially tested by examining the residuals at the longer wavelengths where the O₃ absorption is weak. These tests show that the predictions of the TOMS forward model work quite well over a very large range of conditions, with two key exceptions which we have already noted: sea-glint and UV-absorbing aerosols..

Analysis of long wavelength residuals, however, leaves out the possible effect of clouds, aerosols and surfaces in changing the absorption of radiation by ozone. To understand these effects we use a more realistic radiative transfer model in which we assume that clouds are homogeneous and plane-parallel layer of Mie scatterers. We calculate the effect of clouds on the buv radiances using the Gauss-Seidel vector code [Herman & Browning, 1965] using Deirmendjian's [1969] C1 cloud model. By varying the cloud optical depth in this model one can produce a curve similar to that shown in Fig. 1-6. Comparison with TOMS data shows similar good agreement, which leads us to believe that this model is a reasonable way to model cloud effects in UV, with the advantage that one can account for surface-cloud interactions that the operational model ignores. However, detailed comparison of the results from the two models indicates that despite their drastically different characterization of clouds, the total ozone derived from these models are essentially the same (within $\pm 1\%$), provided one uses the correct effective pressure of the clouds. (The effective pressure of the cloud is usually greater, i.e., the clouds scattering emanates from lower altitude, than the cloud top pressure, depending upon the optical and physical thickness of the clouds, surface albedo and observation geometry. It is expected that OMI cloud algorithms would provide a more accurate value of this pressure than infrared algorithms, which sense the black-body temperature of cloud-tops, for all but very thin clouds, such as cirrus.)

However, this error analysis doesn't apply to clouds and aerosols in the stratosphere, which can significantly alter the absorption of the buv radiation by stratospheric ozone, producing relatively large errors. It has been shown [Torres et al., 1992; Bhartia et al., 1993] that at high solar zenith angles ($\theta_o > 80^\circ$) stratospheric clouds (PSCs) and aerosols may cause the total ozone to be significantly underestimated, provided they are sufficiently optically thick ($\tau > 0.1$) and are close to the ozone density peak. This is because the photons scattered in the stratosphere do not sense the entire ozone column. However, at lower solar zenith angles, the error can be either positive or negative and may vary in a complicated way with observation geometry. Though it is known that optically thick Type III PSCs containing water ice do form due to adiabatic ascent of air as it passes over orographic features (lee waves), sometimes creating localized ozone depletion called a "mini-hole", it is not known if the optical depth of these clouds is large enough, or if they are high enough, to produce the errors postulated by Torres et al. However, the effects of high altitude stratospheric aerosols that form after volcanic eruptions are well understood [Torres et al., 1995]. Bhartia et al. [1993] estimate that the stratospheric

aerosols created few months after the 1991 eruption of Mt. Pinatubo volcano in the Philippines introduced errors in the buv total O₃ retrieval of +6 to -10%, depending on solar zenith angle, though these errors subsided quickly after 6 months as the altitude of the aerosols dropped.

To summarize, under normal circumstances, for OMI the radiative transfer modeling errors contribute no more than 1% rms error in the computation of ozone, provided one has a reasonably accurate (~100 hPa) estimate of effective cloud pressure. (Since this information is not available for TOMS, TOMS errors are estimated to be ~1.5%). However, in the presence of Type III PSCs, and for several months after high altitude volcanic eruptions, the errors may be an order of magnitude larger.

Spectroscopic Constants

Several groups have made measurements of ozone absorption cross-sections recently. Based on evaluation of Bass and Paur [1984] measurements by Chance [private communication], it is estimated that at the wavelengths used to derive TOMS total ozone (317.5 nm) Bass and Paur measurements are probably accurate to better than 2%. Uncertainty in molecular scattering cross-sections are generally considered small (<1%), and in any case the errors are not likely to vary significantly with wavelength to affect derived total ozone.

2.4.2. Inverse Model Errors

In remote sensing problems, the inverse model errors are caused by the fact that the inversion of radiances into geophysical parameters require *a priori* information. This is true of even the simplest type of remote sensing, e.g., measurement of total ozone using direct solar radiation, as employed by ground-based Dobson and Brewer instruments. The inversion algorithms for these instruments require some knowledge of how the ozone is distributed vertically in the atmosphere in order to correct for the effects of atmospheric temperature on ozone absorption cross-section, and for the effect of Earth's sphericity on the airmass factor. Errors in *a priori*, therefore, inevitably introduce retrieval errors; though for Dobson and Brewer algorithms they are usually quite small (<1%). The following is a summary of these errors for TOMS V8.

O₃ Profile

As discussed in Section 2.3, TOMS V8 algorithm uses a carefully constructed 1512 profile data set to minimize profile shape errors, and then it checks the residuals at 312.5 nm to identify unusual profiles and applies a correction. To understand the remaining errors, it is important to consider the region below 20 km (UTLS) and the region between 20-40 km (MS) separately. (There is not much O₃ above 40 km to be of concern.). In general, the UV wavelengths do not have enough information to detect or correct errors in the *a priori* profile in the UTLS region, therefore, 312.5 nm residuals are of no help in this region. So, the variance of error in total O₃ contributed by the UTLS region can be accurately predicted from the error covariance of the *a priori* profile (S)

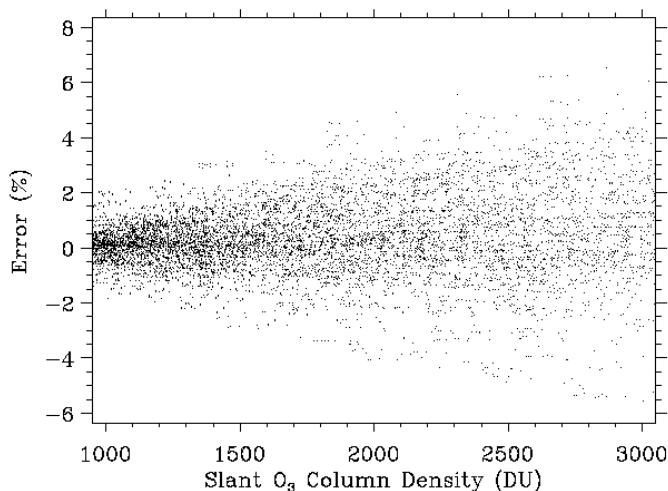


Figure 2-8: Retrieval error due to the UTLS region estimated using Sodankylä ozonesonde data.

and the layer efficiency factors (η), discussed earlier, by $\sum_{l=0}^3 \sum_{l'=0}^3 (1-h_l)(1-h_{l'})S_{l,l'}$. Using ozonesonde data to estimate S , we estimate that the UTLS region produces about 1.5% rms error in deriving total O_3 up to a SCD of 1000 DU. Such small errors are a direct result of the carefully constructed *a priori* we use in our retrievals. The errors, however increase at large SCDs, as shown by Fig. 2-8. These errors have been estimated using data from the Sodankylä ozonesonde station (67.4°N, 26.6°E). As a function of solar zenith angle, the standard deviation of error remains less than 2% up to 81°, increasing to only 3.1% at 86°.

At SCD>1500 DU, the MS region also starts to become important. However, the profiles in this region can be accurately estimated using the shorter wavelength OMI data, so we expect only a modest addition to the total errors. Total rms errors due to ozone profile are estimated to be: ~1.5% up to 70° solar zenith, ~3% at 82° and ~5% at 85°.

Temperature Profile

The basic algorithm corrects for seasonal and latitudinal variation of the atmospheric temperature. Residual errors are less than 0.5% (1σ). Though the errors can become larger in the polar regions, the O_3 profile errors remain the dominant error source at all latitudes. Therefore, at present, we do not see any need to bring in daily temperature maps to improve our total ozone estimates.

2.4.3. Instrumental Errors

Instrumental errors include systematic errors due to pre-launch errors in instrument calibration (spectral and radiometric), calibration drift after launch, and random noise. Since we do not yet know how large these errors are likely to be, we provide sensitivity to various errors in the following.

Spectral Calibration

The 317.5 nm wavelength is located on a plateau in ozone absorption cross-section, hence it is not particularly sensitive to wavelength error: 0.01 nm error in wavelength produces 0.1% error in ozone. It is expected that the OMI's wavelength calibration would be better than 0.01 nm, since instrument wavelength can be monitored using solar Fraunhofer lines as well as ozone absorption lines.

Radiometric Calibration

For the basic TOMS V8 algorithm, which uses two wavelengths, 1% wavelength independent calibration error at these wavelengths, introduces a 0-2 DU ozone error depending on brightness of the scene. (Larger errors occur for darker scenes.) A 1% relative calibration error between the two wavelengths introduces 4-6 DU error depending on slant column ozone amount. (Smallest errors occur at SCD of ~1000 DU). Over the years several strategies have been developed to detect the calibration errors by the analysis of residues. The hyperspectral capability of OMI should be particularly valuable in detecting calibration errors. Using the strategies discussed in section 2.5, we expect that the effect of radiometric calibration errors on ozone can be reduced to less than 1%.

Instrument Noise

1% instrument noise at each of the two wavelengths used for total ozone retrieval leads to 6-9 DU noise in total ozone. For the expected noise of the OMI instrument we expect <2 DU (1σ) noise in total ozone at SCD of up to 3000.

2.4.4. Error Summary

Most of the error sources we have discussed above are systematic, i.e., the errors are repeatable given the same geophysical conditions and viewing geometry. However, most errors vary in a pseudo-random manner with space and time, so they tend to average out when data are averaged or smoothed. The best way to characterize these errors is as follows: the errors at any given location would have a roughly Gaussian probability distribution with standard deviation of about 2% at solar zenith angles less than 70°, increasing to 5% at 85°, with a non-zero mean. The means themselves will have a roughly Gaussian distribution with standard deviation of about 1% with non-zero mean of $\pm 2\%$ (due to error in ozone absorption cross-section). Conservatively, one should assume that the latter error distribution is not affected by the amount of smoothing, i.e., it remains the same whether one looks at monthly mean at any given location, daily zonal mean, monthly zonal mean, or even yearly means. Table 2-2 provides a summary of various error sources.

Table 2-2: Summary of Error Sources

Error Source	Single Pixel (% rms)		Zonal Mean (% rms)	Trend (%/decade)
	SCD<1500	SCD>1500		
O ₃ x-section	<2	<2	<2	0
Atm temp	0.5	2	0-1	0-0.5
0-20 km profile	1	2	<1	<0.5
20-40 km profile	<1	3	0-2	0-0.5
Cloud	0-2	0-2	<0.2	<0.1
Trop aerosol	1	<1	<0.2	<0.1
Strat aerosol/PSC	0-3	0-20	<1	<0.1
Instrument Noise	0.5	1	0	0
Inst calibration	<1.5	<2	<1.5	<1

2.5. Validation

Based on the TOMS experience, we propose three distinctly different validation techniques. The first line of defense against errors is to examine the residuals. A large variety of errors, both in the data processing software and algorithm are readily detected by examining the residuals. Next one does internal validation of the derived ozone itself. This includes examination of any suspicious dependency on viewing geometry, clouds, surface features, or discontinuities in space and time. Finally, one does external validation, in which one compares with ground-truth. We describe each of these three validation procedures in more detail below.

2.5.1. Analysis of Residuals

The purpose of the residue analysis is to find features in the residuals that differ from the features that are expected based on previous error analyses of the algorithm. For example, one expects that sea-glint and certain types of aerosols (smoke, dust and volcanic ash) would cause positive residuals at 365 nm. So, one would make a map of the 365 nm residuals to see if the large residuals occur at places where these features are expected to be present. If necessary, other satellite instruments or ground-based instruments that detect aerosols can be used to verify OMI's observations. Similarly, one expects large residues at shorter wavelengths to occur at large solar zenith angles when the assumed profile above 25 km differs significantly from the true profile. This can be verified using the two other instruments on EOS Aura that measure the ozone profile.

However, the most powerful application of the residuals is to find instrument artifacts, calibration errors, and drifts. This is best done by examining the residues in the tropics for scenes that contain bright clouds ($R > 40\%$). Under these conditions residues due to algorithmic artifacts (e.g., sea-glint, aerosols, ozone profile etc.) are minimized, so the instrument artifacts can be readily detected. For OMI, these artifacts are likely to be caused by the CCD detector array. Given the large number of elements involved, their characterization to a few tenths of a percent, required for accurate ozone retrieval, is an arduous task. The analysis of residuals is particularly useful to see if anything in the instrument has changed following launch. Accurate characterization of the instrument on the first day of operation is hampered by the fact that relative errors in ozone cross-sections are likely to produce $\pm 0.5\%$ wavelength dependent residuals, which makes it difficult to detect small errors in instrument calibration. However, since these errors would not change with time, time-dependent changes after launch should be readily detectable at better than 0.1% level [Joiner & Bhartia, 1997], allowing very high accuracy in the long-term monitoring of ozone.

2.5.2. Internal Validation

Internal validation is designed to catch errors that residue analysis might miss. We mention a few types of analyses that have proved extremely useful for TOMS.

The simplest type of analysis is the examination of the minimum reflectivity derived from the radiances to estimate the surface reflectivity of various types of scenes and then compare it with known values. The analysis is complicated by the fact that the surface reflectivity of almost all surfaces vary with solar zenith angle, so the analysis is most useful for looking at long-term instrument degradation by comparing data from the same month from different years.

Another useful analysis is to examine the consistency of zonal means of total O_3 derived separately from measurements made at different satellite zenith angles but in the same latitude band. OMI makes 60 measurements perpendicular to the satellite track with satellite zenith angles varying from 0 to $\pm 63^\circ$. One expects that in absence of errors the zonal means would show no systematic dependence with satellite zenith angle. Some of the errors that have been found with this method for TOMS are: errors in the computation of spacecraft roll angle and satellite zenith angle, errors due to stratospheric aerosols [Torres et al., 1995], sea-glint related errors, and view angle-dependent instrument calibration errors. This analysis would be of even greater importance for OMI, since different sets of CCD pixels are used for each view angle position. Therefore, errors in the characterization of these pixels would appear as systematic variation in zonal mean ozone with viewing angle.

Another powerful tool is the examination of the consistency of zonal means derived at very different solar zenith angles in the same latitude band. This opportunity arises only near summer solstice when the polar region is sunlit throughout the day. Under these conditions OMI can measure ozone twice at the same latitude, once during the ascending part of the orbit and again during the descending part. Since these measurements occur at very different solar zenith angles, the signal levels and slant column ozone density are quite different. Therefore, consistency of the zonal means derived from the two sides of the orbit provides a powerful check of algorithm and instrument performance.

2.5.3. External Validation

Though it is likely that most of the errors in the retrieval can be detected by internal checks described in the two previous sections, it is necessary to compare with ground-truth to provide a sanity check. There is a network of Dobson and Brewer instruments that currently operate across the globe. Although the quality of these stations vary considerably, in aggregate, they provide an excellent check of the overall data quality of satellite instruments. Comparison

with these instruments requires the generation of a match-up data set, containing those OMI pixels in which an operating ground-station is located. The small pixel size of OMI will make the spatial matching for these comparisons extremely precise.

However, one serious deficiency of the ground-based network is the lack of reliable data under cloudy and large SCD conditions when direct-sun measurements are not possible. As discussed earlier, these are precisely the conditions when the buv total ozone retrievals are most unreliable. To handle this problem, we are currently developing an improved algorithm to derive accurate total ozone from zenith-sky measurements made from the ground using a well-calibrated double monochromator, by applying the techniques developed for TOMS. Preliminary results indicate that it should be possible to derive accurate total ozone values under a wide variety of cloudiness conditions and aerosol loading, up to a solar zenith angle of 85°. The accuracy of these retrievals can be checked by ensuring that zenith-sky measurements are internally consistent (e.g., as a function of solar zenith angle, and with variation in cloudiness) and agree with direct-sun measurements when both types of measurements are possible.

2.6. References

- Ahmad, Z. and P. K. Bhartia, Effect of Molecular Anisotropy on the Backscattered UV Radiance, *Appl. Opt.*, 34, 8309-8314, 1995.
- Ahmad, Z., P. K. Bhartia and N. Krotkov, Properties of backscattered ultraviolet radiance in cloudy atmosphere, in preparation, 2002.
- Bass, A. M. and R. J. Paur, The ultraviolet cross-section of ozone, I, The measurements, in *Atmospheric Ozone*, edited by C. S. Zerefos and A. Ghazi, 606-610, D. Reidel, Norwood, Mass., 1984.
- Bates, D. R., Rayleigh scattering by air, *Planet. Space. Sci.*, 32, 785-790, 1984.
- Bhartia, P. K., J. R. Herman, R. D. McPeters and O. Torres, Effect of Mount Pinatubo Aerosols on Total Ozone Measurements From Backscatter Ultraviolet (BUV) Experiments, *J. Geophys. Res.*, 98, 18547-18554, 1993.
- Caudill, T.R., D. E. Flittner, B. M. Herman, O. Torres and R. D. McPeters, Evaluation of the pseudo-spherical approximation for backscattered ultraviolet radiances and ozone retrieval, *J. Geophys. Res.*, **102**, 3881-3890, 1997.
- Deirmendjian, D., Electromagnetic scattering on spherical polydispersions, Elsevier, 290, 1969.
- Greenblatt, G. D., J. J. Orlando, J. B. Burkholder and A. R. Ravishankara, Absorption Measurements of Oxygen Between 330 and 1140 nm, *J. Geophys. Res.*, 95, 18,577-18,582, 1990.
- Dave, J. V., Meaning of successive iteration of the auxiliary equation of radiative transfer, *Astrophys. J.*, 140, 1292-1303, 1964.
- Dave, J. V. and C. L. Mateer, A preliminary study on the possibility of estimating total atmospheric ozone from satellite measurements, *J. Atmos. Sci.*, 24, 414-427, 1967.
- Dave, J. V., Effect of Aerosols on the estimation of total ozone in an atmospheric column from the measurements of its ultraviolet radiance, *J. Atmos. Sci.*, 35, 899-911, 1978.
- Eck, T. F., P. K. Bhartia, P. H. Hwang, and L. L. Stowe, Reflectivity of the Earth's Surface and Clouds in Ultraviolet from Satellite Observations, *J. Geophys. Res.*, 92, 4287, 1987.
- Herman, B. M., and S. R. Browning, 1965, A numerical solution to the equation of radiative transfer, *J. Atmos. Sci.*, 22, 559-566, 1965.
- Herman, J. R., and E. A. Celarier, Earth surface reflectivity climatology at 340-380 nm from TOMS data, *J. Geophys. Res.*, 102, 28003-28011, 1997.

- Joiner, J., P. K. Bhartia, R. P. Cebula, E. Hilsenrath, R. D. McPeters, and H. W. Park, Rotational-Raman Scattering (Ring Effect) in Satellite Backscatter Ultraviolet Measurements, *Appl. Opt.*, 34, 4513-4525, 1995.
- Joiner, J. and P. K. Bhartia, Accurate determination of total ozone using SBUV continuous spectral scan measurements, *J. Geophys. Res.*, 102, 12,957-12,970, 1997.
- Klenk, K. F., P. K. Bhartia, A. J. Fleig, V. G. Kaveeshwar, R. D. McPeters, and P. M. Smith, Total ozone determination from the Backscattered Ultraviolet (BUV) experiment, *J. Appl. Meteorol.*, 21, 1672-1684, 1982.
- Mateer, C. L., D. F. Heath, and A. J. Krueger, Estimation of total ozone from satellite measurements of backscattered ultraviolet Earth radiance, *J. Atmos. Sci.*, 28, 1307-1311, 1971.
- McPeters, R. D. et al., Nimbus-7 Total Ozone Mapping Spectrometer (TOMS) Data Products User's Guide, NASA Reference Publication 1384, 1996.
- Rodgers, C. D., Inverse methods for atmospheric sounding: Theory and practice, World Scientific Publishing Co., 2000.
- Spurr, R. J. D., Discrete ordinate theory in a stratified medium with first order Raman scattering: a general quasi-analytic solution, in preparation, 2002.
- Torres, O., Z. Ahmad and J. R. Herman, Optical effects of polar stratospheric clouds on the retrieval of TOMS total ozone, *J. Geophys. Res.*, 97, 13015-13024, 1992.
- Torres, O., J. R. Herman, P. K. Bhartia, and Z. Ahmad, Properties of Mt. Pinatubo Aerosols as Derived from Nimbus-7 TOMS Measurements, *J. Geophys. Res.*, 100, pp. 14,043-14,056, 1995.
- Torres, O. and P. K. Bhartia, Impact of tropospheric aerosol absorption on ozone retrieval from backscattered ultraviolet measurements, *J. Geophys. Res.*, 104, 21569-21,577, 1999.
- Wellemeyer, C. G., S. L. Taylor, C. J. Seftor, R. D. McPeters and P. K. Bhartia, A correction for total ozone mapping spectrometer profile shape errors at high latitude, *J. Geophys. Res.*, 102, 9029-9038, 1997.

3. DOAS Total O₃ Algorithm

J.P. Veefkind and J.F. de Haan

Royal Netherlands Meteorological Institute, De Bilt, The Netherlands.

3.1. Overview

This chapter describes the algorithm for deriving the total column of ozone from OMI data using Differential Optical Absorption Spectroscopy (DOAS). The algorithm produces the total column of ozone as well as the so-called slant column for all OMI ground pixels, providing daily global coverage. The total column ozone is for direct use by the end user, whereas the slant column is intended for use for data assimilation and for combining data with other satellite sensors. The fit window used for the DOAS fit is 331.1 to 336.1 nm, which has been selected to minimize sensitivity to atmospheric temperature. The estimated accuracy of the total column ozone is 2-3%. For the slant column density the expected accuracy is better than 2%.

This chapter is organized as follows. In this section we give a brief introduction to the heritage of the product followed by a high level description of the product. In the next section (Section 3.2) we provide a description of the algorithm, followed by error analysis (Section 3.3). Section 3.4 describes how the product and the algorithm will be validated.

3.1.1. Heritage

Space-borne measurements of the ozone column have been performed operationally since the 1970s with the SBUV and TOMS series of instruments. These instruments measure the backscattered radiance in a few 1 nm wide bands. As described in the preceding chapter, ozone column is derived using radiances measured at two wavelengths, while other wavelengths are used for diagnostics and error correction. In 1994 the GOME instrument was launched. It is the first of a series of instruments that measure the UV-VIS with a high spectral resolution. The ozone column is derived from GOME by applying Differential Absorption Spectroscopy (DOAS) [Spurr, 1994; Burrows, 1999; Piters *et al.*, 2000]. DOAS was developed for ground based measurements of atmospheric trace gases, but can also be applied to measurements from space. DOAS derives the ozone column by fitting a reference ozone cross-section to the measured backscattered radiance. The present algorithm for OMI also uses the DOAS technique, but several important improvements have been made compared to the original GOME algorithm.

3.1.2. Product description

The OMI total ozone DOAS product is derived for OMI Level 1B data. In the global operational mode of OMI, the pixel size of the ozone product is $13 \times 24 \text{ km}^2$ at nadir, and the swath width is 2600 km, providing daily global coverage. Besides the global mode data, the algorithm will also ingest zoom-mode Level 1B data. In the zoom-mode, the pixel size is $13 \times 12 \text{ km}^2$ at nadir.

The main products of the OMI total ozone DOAS algorithm are the ozone vertical column density and the ozone slant column density. The vertical column density is the amount of ozone along a vertical path from the ground to the top-of-the-atmosphere. The slant column density is the amount of ozone along an average path that the photons travel from the Sun through the atmosphere to the satellite sensor. The slant column density concept is described in more detail in Section 3.2.1. Compared to the vertical column density, very little a priori information is needed to derive the slant column density. As it is a concise representation of the measured radiance spectrum, people from the data assimilation community have expressed a

need for the slant column density [Eskes *et al.*, 2001]. In addition, tropospheric ozone columns may be derived by combining OMI data with detailed information on the stratospheric ozone profile from a limb sounder. As no assumptions on the ozone profile are used for deriving the slant column density, it is preferred that this quantity is used for deriving the tropospheric ozone columns.

The requirement on the accuracy of the ozone vertical column density, as stated in the OMI Science Requirements Document [Levelt *et al.*, 2000], is 2% or 6 DU, whichever is larger. For the slant column density no accuracy requirement is given. However, as the slant column density is one of the parts needed to derive the vertical column density, the accuracy of the slant column density needs to be higher than that for the vertical column density.

3.2. Algorithm description

The OMI total ozone DOAS algorithm uses the Differential Optical Absorption Spectroscopy (DOAS) method. The algorithm consists of three steps. First, the DOAS method is used to fit the reference differential absorption spectrum of ozone to the measured Earth radiance spectrum and solar irradiance spectrum, to obtain the slant column density. In the second step the slant column density is translated into the vertical column density using the so-called air mass factor (AMF). The third step consists of a correction for cloud effects. In this section we describe each of each of these retrieval steps, including the physical background, as well as assumptions and *a priori* information used.

3.2.1. Slant Column Density

The first step in the ozone DOAS algorithm is to determine the slant column density. The slant column density is the amount of ozone along an average path that the photons travel from the Sun, through the atmosphere, to the satellite sensor. The slant column density is determined by fitting an analytical function to the measured Earth radiance and solar irradiance data. This fit is applied to data taken in a certain wavelength range, called the fit window. A polynomial function, which serves as a high-pass filter, is applied to account for scattering and absorption that vary gradually with the wavelength, e.g., scattering by molecules, aerosols, and clouds. The slant column density is derived from the filtered data, which contains spectral features of ozone in the fit window. Figure 3.1 shows a DOAS fit applied to GOME data.

Basic concept

A nadir-viewing instrument like OMI measures the radiance reflected by the Earth and the atmosphere. For spectral ranges where ozone causes the dominant spectral absorption features, the top-of-the-atmosphere reflectance (TOAR) can be described as a function of the ozone slant column density N_s :

$$\mathbf{r}(\mathbf{l}, \mathbf{q}_0, \mathbf{q}, \mathbf{j} - \mathbf{j}_0) = \frac{\mathbf{P} \mathbf{I}}{F_0} = P(\mathbf{l}) e^{-\mathbf{s}_{O_3}(\mathbf{l}) N_s} \quad [3-1]$$

where, \mathbf{r} is the top-of-the-atmosphere reflectance, \mathbf{I} is the Earth radiance, \mathbf{l} is the wavelength, \mathbf{q}_0 is the solar zenith angle; \mathbf{q} is the viewing zenith angle; $\mathbf{j} - \mathbf{j}_0$ is the relative Sun-satellite azimuth angle; $F_0(\mathbf{l})$ is the extraterrestrial solar irradiance per unit area of the atmosphere, $\mathbf{s}_{O_3}(\mathbf{l})$ is the ozone absorption cross section and $P(\mathbf{l})$ is a low order polynomial that acts as high-pass filter.

Equation [3-1] inspired by the well-known Lambert-Beer law and photon path distributions [Van de Hulst, 1980]. Numerical experiments using radiative transfer calculations have shown that for ozone absorption in the Earth atmosphere, equation [3-1] is an accurate approximation for wavelengths longer than approximately 320 nm.

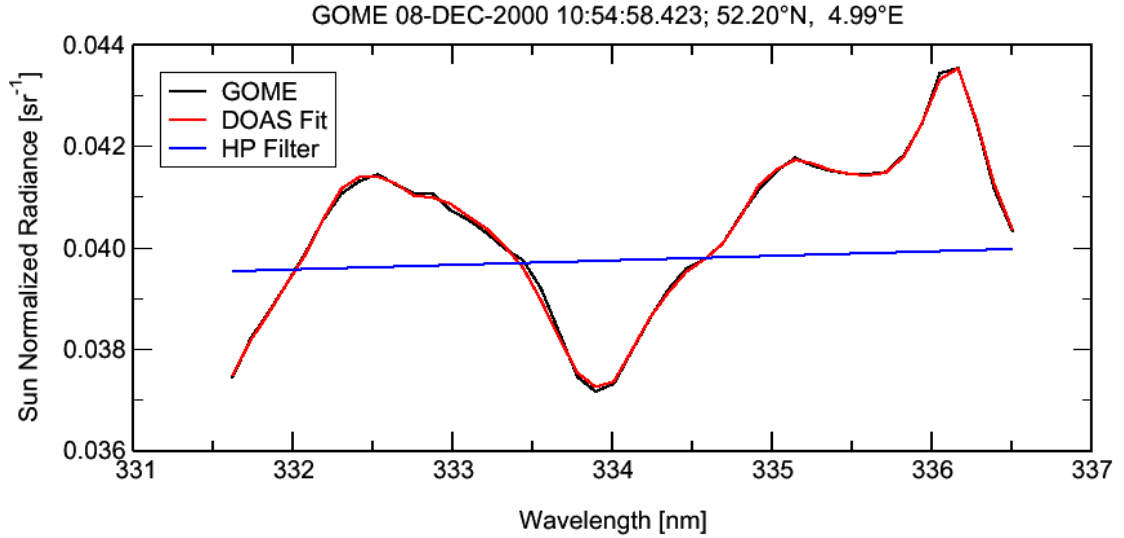


Figure 3.1 DOAS fit applied to GOME data measured over western Europe on December 8, 2000. The spectral resolution of the GOME data was decreased to the OMI spectral resolution. The black line shows the Sun normalized radiance measured by GOME, the red line shows the DOAS fit of the measured data. The blue line shows the high-pass filter that was used in the fit.

Ring effect

In equation [3-1] we assumed that the high-pass filtered TOAR is a function only of the ozone slant column density. However, as described in Chapter 1, the Ring Effect introduces high-resolution structures on the TOAR spectrum which may interfere with absorption features of trace gases. In this section we describe how we account for it.

The TOAR measured by an UV/VIS satellite instrument is the sum of contributions by elastic and inelastic scattered radiation:

$$\mathbf{r}(\mathbf{l}, \mathbf{q}_0, \mathbf{q}, \mathbf{j} - \mathbf{j}_0) = \mathbf{r}_{elastic}(\mathbf{l}, \mathbf{q}_0, \mathbf{q}, \mathbf{j} - \mathbf{j}_0) + \mathbf{r}_{inelastic}(\mathbf{l}, \mathbf{q}_0, \mathbf{q}, \mathbf{j} - \mathbf{j}_0) \quad [3-2]$$

The contribution of inelastic scattering accounts for photons that have encountered one or more inelastic scattering events. The inelastic contribution in [3-2] can be fitted using a reference Ring spectrum [Chance and Spurr 1997; Vountas et al. 1998]. Replacing the inelastic contribution in [3-2] by a reference Ring spectrum $I_{ring}(\mathbf{l})$ and a scale factor c_{Ring} , and replacing the elastic contribution by equation [3-1], the TOAR can be expressed as:

$$\mathbf{r}(\mathbf{l}, \mathbf{q}_0, \mathbf{q}, \mathbf{j} - \mathbf{j}_0) = e^{-s_{O_3}(\mathbf{l})N_s} P(\mathbf{l}) + c_{Ring} I_{Ring}(\mathbf{l}) / F_0(\mathbf{l}) \quad [3-3]$$

In the operational software, $I_{Ring}(\mathbf{l})/F_0(\mathbf{l})$ is replaced a differential Ring spectrum because, due to the polynomial, only differential spectral structures contribute. This differential Ring spectrum is calculated using the software 'RINGOMI' provided by K. Chance. This software is described in [Chance and Spurr 1997], except that the GOME slit function is replaced by the OMI slit function.

The reference Ring spectra on OMI resolution for the wavelength range used in ozone DOAS fitting, is shown in Figure 3.2. This figure shows that the reference Ring spectrum in radiance signal ($I_{Ring}(\mathbf{l})$) is smooth as compared to the reference Ring spectrum in reflectance signal ($I_{Ring}(\mathbf{l})/F_0(\mathbf{l})$). The structure in TOAR is primarily due to strong spectral structures in the solar spectrum. Since the Ring spectrum is now well understood, it can be accurately accounted for in the DOAS fit.

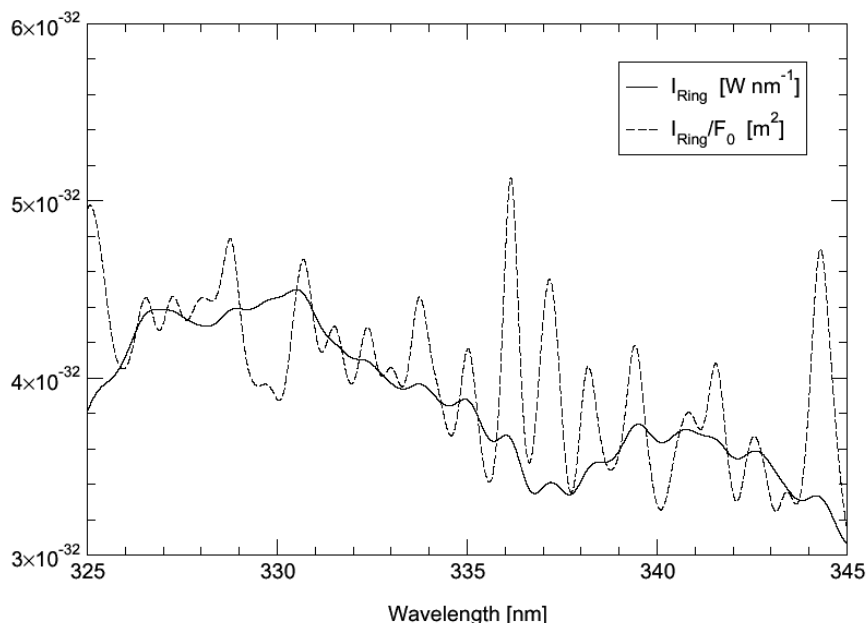


Figure 3.2: Ring effect as a function of wavelength. The solid line is the reference Ring spectrum expressed in radiance units, the dashed line is the ratio $I_{\text{Ring}}(\lambda)/F_0(\lambda)$. The data presented in this figure were calculated using the software “RINGOMI” provided by K. Chance.

Instrumental Errors

The OMI ozone DOAS algorithm uses OMI Level 1B data of the backscattered Earth radiance and the solar irradiance as input. These data will contain random and systematic errors. However, DOAS is not affected by systematic errors unless they produce structures that are correlated with ozone absorption spectrum. In this section, systematic radiometric and spectral calibration errors are discussed. Radiometric errors are due to errors in the conversion from the raw data to radiance or irradiance. Examples of conversion steps for OMI data are: subtraction of dark current from the raw data, straylight correction, quantum efficiency correction, etc.. A detailed overview of the corrections applied is given in the Level 0-1b ATBD [Van den Oord, 2001]. Spectral calibration errors are errors in the wavelength registration of the data.

In OMI, most of the optical path is the same for the Earth radiance and solar irradiance measurements. Dividing the measured Earth radiance by the measured solar irradiance will lead to a cancellation of errors due to components that are in the optical paths of both the radiance and irradiance measurement. The radiometric accuracy of the TOAR is therefore higher than for the separate radiance or irradiance measurement [Levelt *et. al*, 2000].

The DOAS method is insensitive to radiometric calibration errors that are multiplicative and constant with wavelength. However, the method is sensitive to additive radiometric errors (offsets). Offsets in the Earth radiance can be accounted for by adding a fit parameter c_a ¹ to equation [3-3]:

$$\mathbf{r}(\mathbf{l}, \mathbf{q}_0, \mathbf{q}, \mathbf{j} - \mathbf{j}_0) = e^{-\mathbf{s}_{\text{O}_3}(\mathbf{l})N_s} P(\mathbf{l}) + c_{\text{Ring}} I_{\text{Ring}}(\mathbf{l}) / F_0(\mathbf{l}) + c_a / F_0(\mathbf{l}). \quad [3-4]$$

Note that in the last term of equation [3-4] $F_0(\mathbf{l})$ is the solar irradiance measured by OMI.

¹ The behavior of the fit parameter c_a over the lifetime of OMI, may be used to monitor the long term stability of the instrument. It is not possible to add a fit parameter to account for offsets in the measured solar irradiance, because this results in an unstable fit. However, the solar irradiance is well known and the expected offset in the solar irradiance measurements is small

If the OMI radiance or irradiance data show radiometric errors with spectral structure in the DOAS fit window, it depends on the spectral features whether a correction can be made. If the spectral feature is weak, well characterized and doesn't interfere with the ozone absorption cross section, it may be possible to account for it in the fit. In this case, the spectral structure of the error is fitted in the DOAS equation using an extra fitting parameter, similar to the way the Ring effect is treated. Errors that interfere with the ozone absorption cross section cannot be corrected for. If this happens, another fit window should be used that does not show such an interference.

The spectral calibration for OMI is done using the Fraunhofer lines. The expected accuracy of this method is 1/100th of a pixel, corresponding to 0.0015 nm for the wavelength range where DOAS fitting of ozone can be applied. Given the expected spectral accuracy, alignment of wavelength grids using shift-and-squeeze techniques is not foreseen. DOAS fits on GOME spectra that were spectrally calibrated using the Fraunhofer lines (for example Figure 3.1) confirm that if this calibration method is used no shift-and-squeeze techniques are needed.

Fit window

In this section we describe how the fit window for ozone DOAS has been selected. Detailed studies were performed to find the optimum fit window for ozone with respect to the following [Veefkind, 2000a; Veefkind, 2000b, Veefkind, 2000c]:

- Temperature profile
- Instrument signal-to-noise
- Ozone profile
- Other trace gases
- Ring effect.

The conclusions of these studies are that the main drivers for the fit window are the sensitivity of the slant column density to atmospheric temperature and to instrument signal-to-noise. The temperature sensitivity is small for narrow fit windows in distinct wavelength regions [Veefkind, 2000a]. On the other hand, the effect of signal-to-noise is less for wider fit windows [Veefkind, 2000b]. The best compromise between temperature dependence and signal-to-noise was found to be a 5 nm wide window centered around 334.1 nm. Therefore, this fit window was chosen for the slant column density fit of ozone. This fit windows differs from the 325-335 nm window that is used for GOME [Spurr, 1994; Peters *et al.*, 2000]. Although the differential absorption of ozone is smaller compared to the GOME window, the effects of the instrument signal-to-noise on the slant column density are still below 1% [Veefkind, 2000b].

Fit Method

The slant column density is determined by fitting equation [3-4] to the measured TOAR for the fit window. The fit is performed using a least squares fitting procedure, which minimizes the merit function given by:

$$c^2 = \sum_{i=1}^N \left(\frac{y_{meas}(I_i) - y_{sim}(I_i)}{e_{meas}(I_i)} \right)^2, \quad [3-5]$$

where, $y_{meas}(I_i)$ is the measured TOAR, $y_{sim}(I_i)$ is the simulated TOAR radiance as given by Eq. [3-4] and $e_{meas}(I_i)$ is the precision of the measured TOAR. The fit window is between I_1 and I_N .

The simulated TOAR (Eq. [3-4]) is a non-linear function of the fit parameters. Therefore, a non-linear fit routine should be applied. A modified Levenberg-Marquardt method [More, 1978] as adapted from the SLATEC mathematical library [Fong *et al.*, 1993] is used for the non-linear fitting. Information on the quality of the fit is derived from the covariance matrix. The variance of the fitted parameters, as well as the correlation between them, is also obtained from the covariance matrix.

3.2.2. Air Mass Factor (AMF)

In DOAS the air mass factor is used to translate the slant column density into a vertical column density. The slant column density was described in detail in Section 3.2.1. The air mass factor M is defined as the ratio of the slant column density, N_s , and the vertical column density, N_v , i.e.,

$$M \equiv \frac{N_s}{N_v} \quad [3-6]$$

The DOAS fit results in one slant column density for the entire fit window. From the definition of the AMF (Eq. [3-6]) it is clear that there is also one AMF for a fit window.

The AMF depends on the Sun-satellite geometry, as well on the “state of the atmosphere”. With the latter it is meant that AMF depends on the ozone profile, on clouds and aerosol properties, on surface reflectivity properties etc.. Often, the AMF will vary approximately as the geometrical AMF, $M_g = \sec(\mathbf{q}) + \sec(\mathbf{q}_0)$. To eliminate most of the geometrical effects, it is convenient to introduce an effective AMF, M_e , defined as

$$M_e = \frac{M}{M_g}. \quad [3-7]$$

Computation

The AMF can be determined using a radiative transfer model and an OMI simulator. The radiative transfer model produces radiances for a model atmosphere. The OMI simulator is used to produce spectra with the resolution and sampling of OMI. We determine the slant column density by fitting DOAS to these spectra and divide by the known vertical column density to determine the airmass factor. The advantage of this procedure is that exactly the same DOAS fit is applied to the synthetic OMI spectra and to the measured OMI spectra. If the model atmosphere is representative of the ‘real’ atmosphere, this may lead to a cancellation of certain errors.

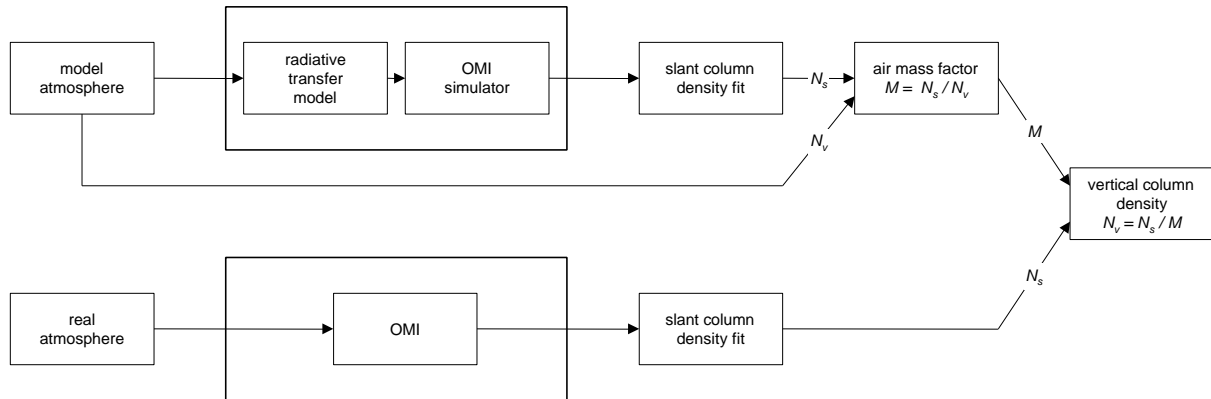


Figure 3.3 Schematic of the procedure to determine the AMF.

The AMF depends, among other parameters, on the ozone profile, as illustrated in Figure 3.4. This figure shows the effective AMF for a given Sun-satellite geometry and surface albedo, for 204 ozone profiles from the *Fortuin and Kelder [1998]* climatology. Although the ozone profiles vary strongly, the variations in the effective air mass factor are small (2% on the 2σ -level, as shown in Figure 3.4). It is noted that these variations depend on the Sun-satellite geometry and maybe larger for larger solar and viewing zenith angles.

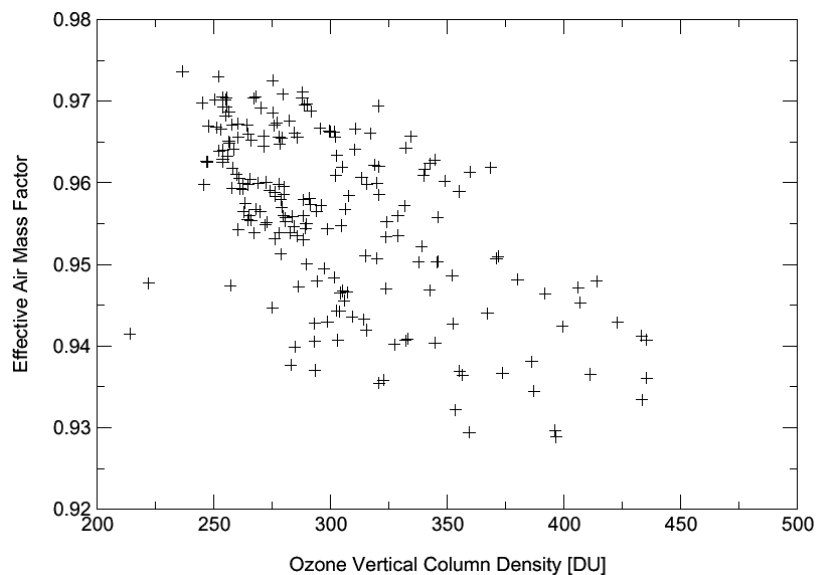


Figure 3.4. Effective AMF as a function of the vertical column density for 204 ozone profiles from the *Fortuin and Kelder [1998]* climatology. The AMF was derived using a 5 nm wide fit window centered around 334 nm. The solar zenith angle is 60° , the viewing zenith angle 46° and the relative azimuth angle 120° . The surface albedo is 0.05.

To reduce the uncertainty in the AMF due to the ozone profile, a slant column density dependent AMF is used. To derive a relation between the slant column density and the AMF, a set of ozone profiles is used that cover the natural variability of the ozone profile for a given location and time period. For each of these profiles the AMF is calculated for a given Sun/satellite geometry and surface properties. This procedure is illustrated in Figure 3.5. The left panel of Figure 3.5 shows the set of ozone profiles that are representative for 50°N for December. These profiles were derived from the *Fortuin and Kelder [1998]* ozone profile climatology, by taking the mean profile and perturbing it by adding or subtracting one and two

times the standard deviation for all the levels. The right panel of Figure 3.5 shows the effective AMF for each of the profiles, plotted as a function of the slant column density. As can be seen in this figure, the effective AMF varies almost linearly with the slant column density. This is used in the algorithm, by making the effective AMF a function of the slant column density, which is determined in the DOAS fit. This method thus reduces the uncertainty in the AMF due to ozone profile changes with respect to the climatology. The algorithm uses a look-up-table of effective AMFs. By using a look-up-table, no radiative transfer calculations have to be done on-line, which results in better performance.

Radiative transfer model

The radiative transfer model used for the simulations of spectra and, consequently, for the calculation of the AMFs (see Fig. 3.3) is the Doubling-Adding-KNMI (DAK) model [*De Haan et al.*, 1987; *Stammes et al.*, 1989; and *Stammes et al.*, 2000]. Single scattering properties of aerosol particles and PSCs are calculated with a Mie scattering code [*De Rooij and Van der Stap*, 1984] that generates coefficients for the expansion in generalized spherical functions. These functions can directly be read by the DAK code making efficient calculations for polarized light possible. Note that the T-matrix code for non-spherical particles of Mishchenko produces similar output in terms of generalized spherical functions, which makes calculations for non-spherical particles straightforward (see e.g. *Mishchenko and Travis* [1998]). The code has the advantage that it is fast for cloudy atmospheres, is well suited for polarized radiative transfer calculations and is very accurate for relatively simple atmospheric models such as homogeneous cloud layers. Severe disadvantages are that the code assumes a plane parallel atmosphere and no (quasi) spherical geometry can be used. Further, inelastic Raman scattering is not included in the code. We are currently contemplating the extension of the code with Raman scattering and a quasi spherical geometry, or to move on to another code that serves our needs better. Note that a change in code will only affect the look up tables and does not change the algorithm itself, which means that the code can be replaced at a relatively late moment.

Look-up-Table

The look-up-table contains the effective AMFs as function of Sun-satellite geometry, surface reflectivity, surface pressures and ozone profile. As mentioned above, the ozone profiles are taken from *Fortuin and Kelder* [1998]. Besides ozone, molecular scattering and absorption by NO₂ and BrO are accounted for in the radiative transfer calculations. Clouds are represented by Lambertian surfaces with an albedo 0.8, as recommended by *Koelemeijer and Stammes* [1999] (see also section 3.2.3).

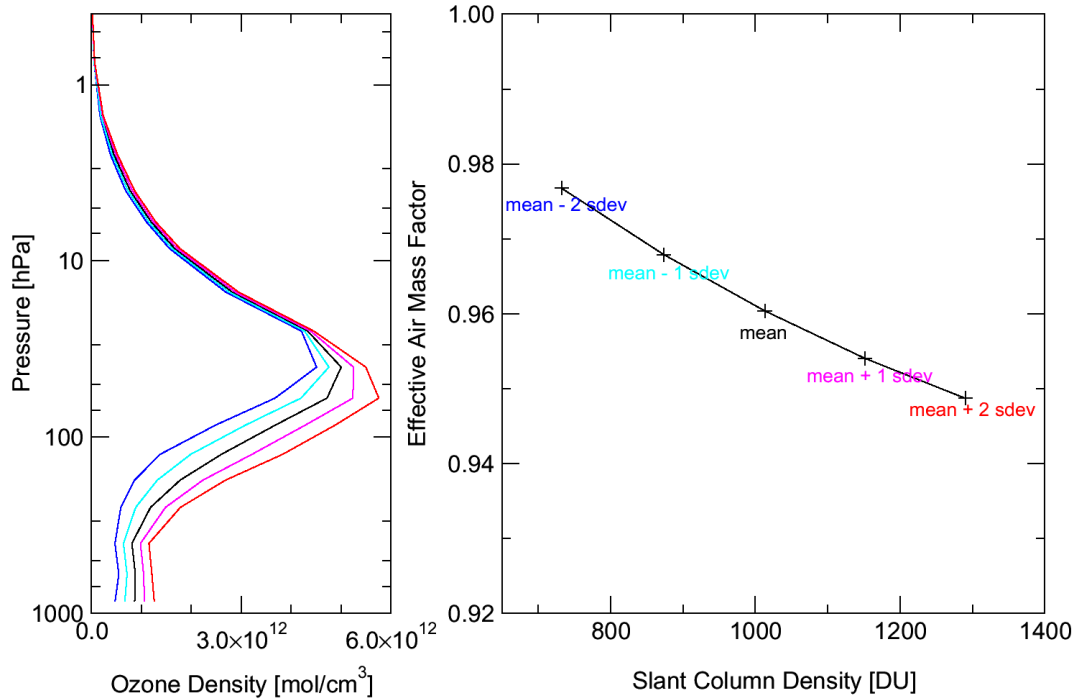


Figure 3.5. Left panel: Ozone density as a function of pressure for mean ozone profile, and mean plus or minus one or two times the standard deviation, for 50° N for December. The mean and standard deviations were taken from the Fortuin and Kelder [1998] ozone profile climatology. Right panel: Effective AMF computed for the ozone profiles shown in the left panel, plotted as a function of the slant column density. The Sun-satellite geometry is: solar zenith angle 60°; viewing zenith angle 46°; and relative azimuth angle 150°. The surface albedo is 0.05.

Table 3.1. Specification of the air mass factor look-up-table dimensions.

Dimension name	Min. value	Max. value	Number of entries
Solar zenith angle	0°	85°	12
Viewing zenith angle	0°	60°	6
Relative azimuth angle	0°	180°	10
Surface reflectivity	0	0.8	5
Surface pressure	100 hPa	1050 hPa	2
Latitude	-90°	+90°	17
Month	1	12	12
Ozone profile	na	na	3

The AMF is obtained by interpolation in the look-up table. In Table 3.1 the dimensions of the look-up table are presented, as well as the foreseen number of entries for each dimension. The inputs that are needed for the interpolation in this look-up table are taken from the following sources. The solar and viewing zenith angles are taken from the Level 1b data. The relative azimuth angle is computed from the solar and viewing azimuth angles as given in the Level 1b data. The surface reflectivity is determined from a monthly climatology. Initially the surface reflectivity climatology determined by TOMS will be used [Herman and Celarier, 1997], but eventually this will be replaced by a climatology determined by OMI. The surface pressure will be determined from the terrain height, as contained in the Level 1b data. The AMF look-up tables will also be interpolated to the latitude and the date of the measurement. Interpolation between the mean and perturbed ozone profiles is done using the method outlined above, using the slant column density as input.

3.2.3. Cloud Correction

In case of a cloudy or partly cloudy pixel, part of the ozone column is covered by clouds. Therefore, a cloud correction is needed, which is described in this section. First we describe the basic cloud model, then the computation of the AMF for a partly cloudy pixel, followed by a description of the correction for the so-called ghost column. Finally, we discuss the computation of the total vertical column density.

Cloud Model

To calculate the AMF for a cloudy conditions a cloud model is necessary. To determine the AMF for cloudy conditions, the cloud fraction and cloud pressure from the OMI O₂-O₂ cloud product are used. For consistency, it is important to use the same cloud model as used in the cloud product. This cloud model represents clouds by opaque Lambertian surfaces with an albedo of 0.80, placed at the cloud pressure. It was found by *Koelemeijer and Stammes* [1999] that this value for the cloud albedo gives the best results for ozone retrieval using DOAS. It is also consistent with the TOMS 340/380 reflectance ratio, as discussed in Chapter 2. This cloud model considers all clouds to be thick, single layer clouds. Partly cloudy pixels are treated as the weighted sum of a clear and a cloudy pixel. Pixels that are fully covered with thin clouds are represented by partly cloudy pixels with a thick cloud. Using this cloud model, the AMFs for fully cloudy conditions are determined using the method described in section 3.2.2. The offline calculated AMFs are stored in a look-up-table. This look-up-table has the same dimensions as listed in Table 3.1, with the difference that the surface pressure is replaced by the cloud pressure and there is a single value of 0.8 used for the albedo of the clouds.

Air Mass Factor for Partly Cloudy Conditions

Partly cloudy pixels are treated as the weighted sum of a clear and a cloudy pixel. In good approximation, the AMF of a partly cloudy pixel is the area and radiance weighted sum of the AMF of a clear and a cloudy pixel:

$$M = w \cdot M_{cloudy} + (1 - w) M_{clear}, \quad [3-8]$$

where w is the weighting factor, M_{cloudy} is the AMF for a cloudy pixel and M_{clear} is the AMF for a clear pixel. The AMFs for clear and cloudy conditions are taken from the look-up-tables described above. The weighting factor w in Eq. [3-8] is the fraction of the photons that originates from the cloudy part of the pixel. w can be expressed as:

$$w = \frac{f_c \langle I_{cloudy}(p_c) \rangle}{\langle I \rangle}, \quad [3-9]$$

where f_c is the cloud fraction, $\langle I_{cloudy}(p_c) \rangle$ is the average radiance over the fit window for a pixel that is fully covered with a cloud that is located at pressure p_c , and $\langle I \rangle$ is the average measured radiance for the pixel. The cloud weighting factor w is calculated offline as function of Sun/satellite geometry, surface albedo and pressure, and cloud fraction and pressure, and stored in a look-up-table.

Ghost Column

The cloud model treats cloud as an opaque Lambertian surface of albedo 0.8. We call the amount of ozone below this surface the “ghost column”. It is computed by integrating the ozone profile from the surface to the cloud pressure. The profiles are taken from the *Fortuin and Kelder* [1998] climatology. Using the standard deviations provided in this climatology, the ghost column is made a function of the slant column density, in a similar way as the AMF is a function

of the slant column density (see Section 3.2.1). As is the case for the AMF, the ghost column will also be determined by interpolation to the latitude and date of the measurement.

Total Vertical Column Density

For the computation of the total vertical column density, three cases can be distinguished:

- cloud-free pixels
- cloud covered pixel
- partly cloudy pixels.

For a cloud free pixel the total vertical column density N_t is given by :

$$N_t = \frac{N_s}{M_{clear}}, \quad [3-10]$$

where N_s is the slant column density and M_{clear} is the AMF for clear atmosphere.

For a cloudy pixel the total vertical column density is given by:

$$N_t = \frac{N_s}{M_{cloudy}} + N_g, \quad [3-11]$$

where N_g is ghost column density. For a partly cloudy pixel the total vertical column density is given by:

$$N_t = \frac{N_s + w \cdot M_{cloudy} \cdot N_g}{M}, \quad [3-12]$$

where the AMF M is determined according to equation [3-8]. For a cloud-free scene, Eq. [3-12] reduces to Eq. [3-10], and for fully cloudy pixels it reduces to Eq. [3-11].

3.3. Error Analysis

In this section the error analysis for the OMI ozone DOAS product is presented. The sensitivity of the output product is tested for the following sources of error

- forward models errors
- a priori errors
- instrument errors.

As already discussed in Section 3.2, there are three main steps in the DOAS algorithm: computation of the slant column density, computation of the AMF, and cloud correction. The sensitivity of these steps to the various errors is very different. Therefore, the error sensitivity of the main steps are treated separately in Sections 3.3.1, 3.3.2 and 3.3.3. All errors are combined in Section 3.3.4, to obtain the error sensitivity of the end product. Finally, in Section 3.3.5 we will focus on errors for some exceptional cases, such as desert dust, biomass burning, and polar stratospheric clouds.

3.3.1. Slant column density

The slant column density fits an analytical function to the measured Sun normalized radiance spectrum. Before applying this fit, the measured OMI solar irradiance spectrum has to

be interpolated to the wavelength grid of the radiance measurement. Besides the OMI spectra, reference spectra of ozone and Ring effect are used in the fit.

Forward model errors

The forward model that is used is the analytical function that is fitted to the measured radiance spectrum. The absorption by BrO, SO₂, and NO₂ are ignored in this fit. The effect of neglecting these gases in the slant column density fit was tested by fitting simulated OMI spectra with low and high concentrations of these gases. These test show that the error due to neglecting BrO, SO₂ and NO₂ is generally less than 0.5%, and is mainly caused by variations in BrO and NO₂.

***A priori* errors**

The a priori information that is used are reference spectra of the ozone cross section and the Ring effect. These spectra have to be convoluted with the measured OMI slit function. The ozone cross section is temperature dependent, so an effective temperature of ozone is assumed.

The accuracy of the ozone cross sections is estimated to be 1% [Bass and Paur, 1984]. Therefore, the error in the slant column density is estimated to be 1%. Errors due to inaccuracies in the Ring spectrum are expected to be negligible. The DOAS technique only uses the spectral features over a fit window, and is thus insensitive to errors in the absolute absorption cross section due to for example offsets. The one-to-one conversion of uncertainty in the absolute cross section to uncertainty in the slant column density is therefore probably on the safe side. Before applying the reference cross section to OMI data, it has to be convoluted with the instrument spectral response function (slit function). The OMI spectral response function will be measured using a new technique. The expected error in the response function is expected to be of the order 1-10% for the region within one times the full width half maximum. The error in the slant column density due to the error in the slit function is estimated to be of the order 0.1%.

The fit window is optimized such that the temperature dependence is minimal. The sensitivity of the slant column density was tested by changing the effective temperature by 10° K. This test showed that for the present fit window choice the resulting change in the slant column density is less than 0.3%.

Instrument errors

There are different instrument effects that have to be considered:

- radiometric noise
- radiometric additive factor
- radiometric multiplicative factor
- spectral structure
- spectral calibration error
- spectral stability

The radiometric noise of OMI in the 330 – 340 nm range is expected to be of the order 1000. For the proposed fit window centered around 334.1 nm and 5 nm wide, the expected error in the slant column density due to noise is less than 1% [Veefkind, 2000b].

As discussed in Section 3.2.1, a radiometric additive factor (offset) in the radiance measurement that is constant over the entire fit window is accounted for in the DOAS fit function. This is not the case for the solar irradiance measurements, but offsets in the solar

irradiance spectrum are not expected. If such offsets do occur they can easily be corrected for, since the solar irradiance can be measured with a high signal-to-noise and there are several other instruments that can be used for comparison. Hence, the error in the slant column due to additive errors is expected to be negligible.

Section 3.2.1 discusses the effect of multiplicative errors (scale factors) that are constant over the fit window. The DOAS fit function can deal with this kind of error, so no effect on the slant column density is expected.

The effect of instrumental spectral structures is very hard to assess, as it strongly depends on the exact spectral features and how well they can be characterized. If the spectral structures are smaller than $1 \cdot 10^{-4}$, as required according to the SRD [Levelt *et al.*, 2000], the effect on the slant column density will be negligible. After the performance testing of the OMI instrument, information will be available on the magnitude and shape of residual spectral structures. When this information becomes available, the error due to residual spectral features will be re-assessed.

The DOAS method is sensitive to errors in the spectral calibration. The spectral calibration for OMI is done using the Fraunhofer lines in the solar irradiance and Earth radiance spectra. Using this method, the spectral calibration uncertainty is estimated to be less than $1/100^{\text{th}}$ of a pixel, which for the UV-2 channel is 0.0015 nm. The error in the slant column density due to a spectral calibration error of $1/100^{\text{th}}$ of a pixel is less than 1%.

Due to temperature variations of OMI, the wavelength grid varies over an orbit. Therefore, the wavelength grid of the earth radiances differs from that of the solar irradiances. The maximum shift between the Earth radiances and solar irradiances (the spectral stability) is expected to be less than $1/20^{\text{th}}$ of a pixel. To determine the slant column density, the radiance and irradiance are brought onto the same wavelength grid, which involves interpolation. The effect of spectral stability was tested by shifting the wavelength grid of the solar irradiance, and is estimated to be less than 0.25% for a spectral stability of $1/20^{\text{th}}$ of a pixel.

3.3.2. Air mass factor (AMF)

The AMF is determined for clear and cloud covered pixels by interpolating in a pre-calculated look-up table, as described in Section 3.2.2. The following is a summary of errors in computing the AMF.

Forward model errors

In the radiative transfer model calculations that are performed to construct the AMF look-up-table, scattering and absorption by aerosol particles is ignored. For boundary layer aerosol, the error in the AMF for normal aerosol loads is estimated to be 0.2%. The effect of absorbing aerosol layers at higher altitude, for example desert dust or smoke layers, is larger. These cases are discussed in Section 3.3.5.

Clouds are represented in the forward model calculations by Lambert surfaces with an albedo of 0.8. As shown by *Koelemeijer and Stammes* [1999] and *Koelemeijer* [2001], this approximation results in differences of the order of 1% for the AMF for ozone as compared to more sophisticated cloud models. It is clear that this error only occurs when computing the AMF for the cloud covered part of the pixel.

The plane-parallel approximation used in the present DAK model and the restriction to elastic scattering may give rise to substantial errors, but these will be (nearly) eliminated by extending the code or moving to a more suitable radiative transfer code.

A priori errors

The a priori information that is used to determine the AMF for the cloud free part of the pixels is the surface reflectivity and the ozone profile. For the cloud covered part of the pixel the cloud pressure and the ozone profile is used.

The sensitivity of the AMF on the ozone profile was estimated from latitudinal and seasonal variations of the AMF as computed for the Fortuin and Kelder climatology. Using the relation between the AMF and the slant column density in a similar way as discussed in Section 3.2.2, the error in the AMF can be estimated. The results show that the sensitivity of the AMF on the ozone profile increases with the geometrical AMF. The maximum error in the AMF due to the ozone profile is estimated as 2%, whereas the average error is estimated to be less than 0.5%.

For the cloud free part of the pixel, the AMF depends on the surface reflectivity. The seasonal variation of the surface reflectivity in the UV is on average 0.03. Assuming that the accuracy of the surface reflectivity is of this order, the resulting error in the AMF is less than 0.3%.

The sensitivity of the AMF for a cloud covered pixel was estimated from the variations in the AMF as a function of the cloud pressure. For clouds at an altitude of 1 km altitude an error of 100 hPa in the cloud pressure results in an 0.6% error in the AMF. For clouds at 10 km altitude this error has increased to 3%. The average error is estimated as 1%.

For a cloud free pixel, the total error in the AMF is estimated to be 0.6%, for a cloudy pixel the error is estimated to be 1.5%.

3.3.3. Cloud correction

In the cloud correction step, the amount of ozone below the cloud (ghost column) is calculated using an ozone profile climatology and the cloud pressure. The a priori error in the ozone profile climatology was estimated by looking at the standard deviations at each level, as supplied as part of the climatology. This error in the ghost column is estimated to be 25%. The error in the ghost column due to an error of 100 hPa in the cloud pressure is of the order 4 DU. For typical conditions, the total error in the ghost column is estimated to be 40%.

Table 3.2. Error estimates for the OMI ozone DOAS product.

Source	Total Error [%]	Relative Error [%]
Slant Column Density		
Other trace gases	0.5	
Absorption cross section	1	
Instrument response function	0.1	
Atmospheric temperature	0.3	0.3
Instrument signal-to-noise	1	1
Instrument spectral calibration	1	
Instrument spectral stability	0.25	
Air mass factor		
Aerosols	0.2	0.2
Clouds	1	1
Ozone profile	0.5	0.5
Surface reflectivity	0.3	
Cloud pressure	1	1
Cloud fraction	0.8	0.8
Cloud Correction		
ghost column	40	40

Vertical Column Density		
Clear	2.1	1.2
Partly Cloudy	2.5	1.7
Cloudy	3.0	2.2

3.3.4. Error Budget

The error estimate for the total vertical column density is derived from the error estimates of the slant column density, the AMF, and ghost column. The error in the slant column density is 1.8%. The expected accuracy of the AMF depends on the cloud fraction. The accuracy of the cloud fraction is expected to be better than 0.1 [Levelt *et al*, 2000]. This results in an error in the AMF of the order 0.8%. The total error in the AMF is 1.0% for a cloud free pixel, for a cloudy pixel this is 1.7%. For a partly cloudy pixel an error of 1.4% is expected.

For a cloud free pixel the vertical column density is computed by dividing the slant column density by the AMF. The total error of the vertical column density for this case is 2.1%. For a cloud covered pixel this error increases to 3.0%, due to the uncertainty in the ghost column. For partly cloudy pixels, the error will be in between the value for the clear and cloudy case, and is estimated to be 2.5%.

For determining trends in ozone, the relative error is important. The relative errors are defined as errors that can vary for two measurements for the same location for two successive days. This criterion was used to determine which of the errors in Table 3.2 are relative errors. For some error sources, like for example the spectral calibration, it is quite arbitrary to what extent this error of relative nature. For these arbitrary cases, the error was marked to be fully of relative nature, making the budget for relative errors in Table 3.2 a conservative estimate. As can be seen in Table 3.2, the relative error of the vertical column density is 1.2% for a cloud-free pixel, 2.2% for a cloudy pixel and 1.7% for a partly cloudy pixel. Thus, for cloudy conditions, the relative error is dominated by errors related to clouds.

3.3.5. Exceptional Cases

In some exceptional cases the error in the ozone column can be considerably larger than the errors in the error budget (Section 3.3.4). Here, the effect of desert dust aerosols, biomass burning, polar stratospheric clouds, and large solar zenith angles are discussed.

Desert Dust

Desert dust can be transported in elevated layers over thousands of kilometers away from the source region. This situation is frequently observed over the equatorial Atlantic during late summer and fall. Scattering and absorption by these desert dust aerosols change the radiative properties of the atmosphere, and thus affect the AMF. To quantify the effect of ignoring these aerosols in the AMF calculations, retrievals were performed on simulated OMI spectra with and without desert dust. Simulated spectra were generated for desert dust layers at 2.5 and 3.5 km altitude. The optical thickness of these layers was 1.0, and the single scattering albedo was 0.8. These calculations show that the effect of ignoring desert dust aerosols yields an underestimation of the ozone vertical column density of 0.4 to 0.8% for the layer at 2.5 km, and 0.9 to 1.4% for the layer at 3.5 km.

Biomass Burning

Biomass burning and forest fires are an important source of absorbing aerosols. However, besides increased column amounts of absorbing aerosols, biomass burning also causes increased amounts of tropospheric ozone. Both the presence of absorbing aerosols and the increased

tropospheric ozone levels will cause an underestimation of the vertical column density of ozone. To estimate both effects, simulations were performed with biomass burning aerosols and increased ozone concentrations in the lowest three kilometers of the atmosphere. Aerosols with a single scattering albedo of 0.9 and an optical thickness of 1.0 were assumed. Tropospheric ozone levels were increased with 20 DU. These simulations show that each effect causes an underestimation of the ozone vertical column density of about 4%. The combined effect of having both absorbing aerosols and increased ozone levels gives an underestimation of 8-9%.

Polar Stratospheric Clouds

The effect of polar stratospheric clouds (PSCs) depends strongly on the optical thickness of the PSC layer and on the PSC layer altitude. Also, the effect increases with increasing solar zenith angle. To quantify the effect of PSCs on the retrieval of the total ozone column, a study was conducted that tested different PSC types at two altitudes [Veeffkind, 2002]. These altitudes were chosen just below and just above the ozone maximum. The results of this study show that for the most frequently observed type of PSCs (Type I), which are characterized by a typical optical thickness of 0.01, the maximum error in the ozone column is less than 3 %. It is noted that approximately 90 % of all PSCs are of Type I. For Type II PSCs, which have a typical optical thickness of 0.04, the maximum error is 11 % and on average the error is less than 0.5 %. The errors are largest for PSCs of Type III, which have a typical optical thickness of 0.4. For this type the error can be as large as 40 %, but on average the error is still below 5 %. Also, it is noted that less than 1 % of all PSCs are of Type III.

Large Solar Zenith Angles

Large solar zenith angles ($>80^\circ$) are especially important for observing ozone hole conditions. The error in the ozone vertical column density is larger than for normal geometries due to the following effects:

- Decreased instrument single-to-noise
- Large variations in the ozone profiles
- Large temperature variations
- Decreased sensitivity for tropospheric ozone
- Errors in the radiative transfer models due to spherical effects of the atmosphere.

Although none of the effects listed above will dominate, the combination of all these effects will lead to larger errors for high solar zenith angles than for normal Sun/satellite geometries. As a first order estimate, we expect the errors in the ozone vertical column density to increase to 5%. TOMS and GOME experience show that these errors increase with solar zenith angle, and are of the order 5-10% [Lambert *et al.*, 1999].

3.4. Validation

In this section two kinds of validation are considered: algorithm validation and product validation. In algorithm validation synthetic OMI data is used. The results of the algorithm are compared to the 'true' values. These 'true' values are known from the model atmosphere that was used for generating the synthetic data set. The advantage of algorithm validation is that we have full control over the synthetic input data, so that effects of certain errors can be tested separately. The disadvantage is that not all errors can be tested for. In product validation real

OMI data is used. The results are compared to other independent measurements of the same quantity, the so-called correlative data set. The advantage of product validation is that it is a true end-to-end validation of the product, involving all possible error sources. The disadvantage is that the correlative data set may have a different coverage, or may not be available at the time of the OMI measurement. Also, product validation depends strongly on the quality of the correlative data set. It is also noted that product validation can only be done after the EOS Aura launch.

The scope of this section is to give an overview of the validation plan on a high level. For product validation, all details are given in the Aura Validation Plan [*Froidevaux et al.*, 2001].

3.4.1. Algorithm validation

In the Science Requirements Document for OMI-EOS [*Levelt*, 2000] the required accuracy for the products are given based on algorithm validation. The algorithm validation is thus important to check whether these requirements are met. Therefore, the synthetic data sets should be as realistic as possible, using an state-of-the-art radiative transfer model and an accurate OMI simulator. The synthetic data set should cover realistic atmospheric profiles, including clouds and aerosols, and should cover all part of the globe for all seasons.

The use of two synthetic data sets are foreseen. The first synthetic data set is provided by the algorithm developers of the product. It is a limited data set of which the main purpose is to perform validation of all sub-parts of the algorithm. An important part of the error assessment in Section 3.3 was performed using this synthetic data set. The second data will be provided by the OMI US team leader. This data set should cover several orbits of synthetic OMI data. With this data set an end-to-end test will be performed. The requirements stated in the Science Requirements Document for OMI-EOS will be checked using this data set. Also, the robustness of the algorithm will be tested.

Also the use of GOME data, converted to the spectral resolution and sampling of OMI, is foreseen. Such quasi-OMI data may be used for robustness testing, as well as for comparison between the standard GOME algorithms results and the OMI algorithm results.

3.4.2. Product validation

In product validation three phases can be distinguished: the initial checkout, the core validation and the long term validation. The initial checkout phase will be done for the first months during which the OMI instrument is operational. It will provide a first impression of the quality of the data product. A limited number of correlative data will be used in this phase, covering different parts of the globe.

In the core validation a detailed comparison is done between the data products and correlative data sets. The core validation should cover the entire globe and should be performed for different seasons. Given the large uncertainties under cloudy conditions or in the presence of PSCs or large aerosol loadings, it is recommended to put special emphasize on validation measurements in these conditions. One of the problems foreseen in the core validation phase is that the accuracy of the data product is similar to, or better than those of the correlative data sets. Therefore, the analysis of times series of comparisons between the OMI data product and correlative data will be very important. Also, in this validation phase data assimilation should be considered, to overcome the common problem of mismatches in both space and time between OMI data and correlative data. Although collocated data set are preferred for the validation, data assimilation can be used as a tool to build statistics more rapidly. The core validation should cover several months of data. To give an unbiased judgment of the product, the core validation should be performed by others than the product developers.

As one of the objectives of the OMI mission is to determine trends in the ozone layer, long-term product validation is of crucial importance. Long term validation should include comparisons of trends from satellite measurements and from ground based measurements. To quickly detect changes in the product, data assimilation is an important tool. With data assimilation, the statistical information is much quicker available than when correlative data sets alone are used.

A pre-launch product validation is possible by using GOME data, converted to OMI spectral resolution. Data produced by the algorithm using these quasi-OMI data can be compared to correlative data sets to get a first impression of the accuracy of the data product.

3.5. Acknowledgments

For the work described in this chapter the DAK radiative transfer code was used, which has been made available to us by P. Stammes (KNMI).

3.6. References

- Bass and Paur. The ultraviolet cross-sections of ozone. I. The measurements. II - Results and temperature dependence, In *Proc. Quadrennial Ozone Symp.*, Chalkidiki, Greece, Eds. C. Zefros and A. Ghazi. Reidel, Dordrecht, 606p., 1986
- Burrows, J.P., M. Weber, M. Buchwitz, V. Rozanov, A. Ladstätter-Weissenmayer, A. Richter, R. De Beek, R. Hoogen, K. Bramstedt, K.W. Eichmann, M. Eisinger, and D. Perner, The Global Monitoring Experiment (GOME): Mission concept and first scientific results, *J. Atmos. Sci.*, Vol 56, 151-175, 1999.
- Chance, K. and R.J.D. Spurr, Ring Effect Studies: Rayleigh Scattering, Including Molecular Parameters for Rotational Raman Scattering, and the Fraunhofer Spectrum, *Applied Optics* 36, 5224-5230, 1997.
- De Haan, J.F., P.B. Bosma, and J.W. Hovenier, The adding method for multiple scattering calculations of polarized light, *Astron. Astrophys. Vol 183*, 371-391, 1987
- De Rooij, W.A., van der Stap, C.C.A.H., 1984, Expansion of Mie Scattering Matrices in Generalized Spherical Functions, *Astron. & Astrophys. Vol 131*, 237-248
- Eskes et al.. A new approach to GOME NO₂. In: *Final report of the project "Sciamachy Data Assimilation"*, Beleidscommissie Remote Sensing (BCRS) project 4.1/AP-09, February 2001.
- Fortuin J.P.F., and H. Kelder, An ozone climatology based on ozonesonde and satellite measurements, *J. Geophys. Res.*, Vol 103, NO. D23, 31,709-31,734, 1998.
- Fong, K.W., T.H. Jefferson, T. Suyehiro and L. Walton, Guide to the SLATEC Common Mathematical Library, available at: <http://www.netlib.org/slatec/guide>, 1993.
- Froidevaux, L., Douglass, A. (Eds.), Earth Observing System (EOS) Aura Science Validation Plan, Version 0.9, 2001.
- Grainger, J.F., and J. Ring, Anomalous Fraunhofer line profiles, *Nature* 193, 762, 1962.
- Herman, J.R., and E.A. Celarier, Earth surface reflectivity climatology at 340-380 nm from TOMS data, *J. Geophys. Res.*, Vol 102, 28003-28011, 1997.
- Koelemeijer, R.B.A., and P. Stammes, Effects of clouds on ozone column retrieval from GOME UV measurements, *J. Geophys. Res.*, Vol 104, NO. D7, 8,281- 8,294, 1999.
- Koelemeijer, R.B.A., Effect of Lambert surface approximation for clouds on the air mass factor of ozone in the UV, KNMI memo, March 7, 2001.
- Lambert, J.C., M. van Roozendaal, M. de Maziere, P.C. Simon, J.P. Pommereau, F. Goutail, A. Sarkissian and J.F. Gleason, Investigation of the Pole-to-Pole performance of spaceborne atmospheric chemistry sensors with the NDSC, *J. Atmos. Sci.*, Vol. 56, 176-193, 1999.

- Levelt P.F., and co-authors, Science Requirements Document for OMI-EOS, RS-OMIE-KNMI-001, Version 2, ISBN 90-369-2187-2, 2000.
- Mishchenko, M.I., and L. D. Travis, Capabilities and limitations of a current FORTRAN implementation of the T-matrix method for randomly oriented, rotationally symmetric scatterers, *J. Quant. Spectrosc. Radiat. Transfer*, Vol 60, 309-324, 1998
- More, J. J., The Levenberg-Marquardt algorithm: implementation and theory. In Numerical Analysis Proceedings (Dundee, June 28 - July 1, 1977, G. A. Watson, Editor), *Lecture Notes in Mathematics 630*, Springer-Verlag, 1978.
- Piters, A.J.M., P.J.M. Valks, R.B.A. Koelemeijer, and D.M. Stam, GOME Ozone Fast Delivery and value-Added Products, Version 3.0, *KNMI Report*, GOFAP-KNMI-ASD-01, KNMI, De Bilt, The Netherlands, 2000.
- Spurr, R., GOME Level 1 to 2 Algorithms Description, DLR Technical note ER-TN-DLR-GO-0025, Oberpfaffenhofen, Germany, 1994.
- Stammes, P., J.F. de Haan, and J.W. Hovenier, The polarized internal radiation field of a planetary atmosphere, *Astron. Astrophys. Vol 225*, 239-259, 1989
- Stammes, P., Spectral radiance modelling in the UV-Visible range, to appear in: *IRS 2000: Current problems in Atmospheric Radiation*, Eds. W.L. Smith and Y.M. Timofeyev, A. Deepak Publ., Hampton (VA), 2001
- Van de Hulst, H.C., Multiple Light Scattering. Tables, Formulas and Applications. Academic Press, San Diego, Ca., pp 573-577, 1980.
- Van den Oord, G.H.J., Voors, R.H.M., and J. de Vries, The Level 0 to 1B processor for OMI radiance, irradiance, and calibration data, In: *OMI ATBD Vol 1, Chapter 3*, Ed: P.F. Levelt, 2001.
- Veefkind, J.P., Temperature effects on ozone slant column density, draft 2, *Tech. Rep.*, TN-OMIE-KNMI-234, KNMI, De Bilt, The Netherlands, 2000a.
- Veefkind, J.P., Effects of instrument signal-to-noise on ozone DOAS, *Tech. Rep.*, TN-OMIE-KNMI-239, KNMI, De Bilt, The Netherlands, 2000b.
- Veefkind, J.P., Effect of ozone profile shape on the slant column density, *Tech. Rep.*, TN-OMIE-KNMI-232, KNMI, De Bilt, The Netherlands, 2000c.
- Veefkind, J.P., Effects of polar stratospheric clouds on the retrieval of OMI DOAS total ozone, *Tech. Rep.*, SN-OMIE-KNMI-321, KNMI, De Bilt, The Netherlands, 2002. Vountas, M., Rozanov, V.V., and Burrows, J.P. 1997. Ring Effect: Impact of rotational Raman scattering on radiative transfer in Earth's Atmosphere, *Journal of Quantitative Spectroscopy and Radiative Transfer*, Vol. 60, No. 6, 943-961, 1998.

4. Ozone Profile Algorithm

Roeland F. van Oss¹, Robert H. M. Voors¹ & Robert D. J. Spurr²

¹Royal Netherlands Meteorological Institute, De Bilt, The Netherlands

²Harvard-Smithsonian Center for Astrophysics, Cambridge, USA

4.1. Overview

In Chapter 1 we discussed the information contained in the buv radiances regarding the vertical distribution of ozone. The retrieval of the ozone profile from a buv spectrum constitutes an ill-posed non-linear inversion problem, similar to those that appear in many satellite retrieval problems. There are now standard procedures for solving such problems [Rodgers, 2000]. Our approach is based on the Optimal Estimation (OE) technique [Rodgers, 2000], which involves the use of a forward model to calculate the radiances and the Jacobian with respect to the state vector (a vector of quantities that one plans to retrieve), *a priori* information about the state vector, and *a priori* and measurement error covariance matrices. In the following sections we describe this procedure in more detail.

4.1.1. Historical Background

Singer & Wentworth [1957] first suggested that ozone profile information could be extracted from satellite buv measurements. In April 1970 the BUV instrument on the Nimbus-4 satellite started operational measurements of ozone profiles using this technique. Since then 6 similar instruments have flown on NASA and NOAA satellites, and this measurement series is expected to continue until 2010. Though these instruments have undergone three generations of improvement (BUV, SBUV, SBUV-2), they all have made measurements in twelve 1-nm wide wavelengths bands between 250 and 340 nm. The operational algorithm (version 6), however, uses only 8 wavelengths between 250 and 306 nm (313 nm is added at large solar zenith angles) and derives profiles using single-scattering component of the measured radiances [Bhartia *et al.*, 1996] rather than the total radiances. The multiple-scattering component, which is assumed to be dependent on total ozone only, is estimated using a look-up table. A key feature of this algorithm is that it makes the *a priori* assumption that the column ozone above 2 hPa has a power-law relationship with atmospheric pressure. It was established early in the history of buv measurements that the single-scattering radiative transfer integral has an analytical solution when one makes this approximation [Rawcliffe and Elliott, 1966; Thomas and Holland, 1977; McPeters, 1980]. In the lower stratosphere, the algorithm constructs *a priori* profiles using independently determined total ozone (from the longer wavelengths) and a database of standard profiles that vary with total ozone. It is well known that the ozone profile in the lower stratosphere at a given latitude is highly correlated with total ozone.

A new SBUV algorithm (version 8) is currently under development at NASA. This algorithm proposes a more traditional implementation of the OE technique using seasonal and latitude dependent climatology as *a priori* rather than assuming the power-law and using total ozone. Also, the algorithm will extend the longest wavelength to 318 nm, and will use total radiances rather than their single scattering. Though this algorithm is expected to improve BUV retrievals in the lower stratosphere, its performance in the upper stratosphere compared to version 6 is not yet known; as it will depend upon whether the power-law or the climatology produces a better *a priori* in the mesosphere. If the validation results support the former, a hybrid algorithm may turn out to be more appropriate.

Though the OMI profile algorithm described in this chapter is conceptually similar to the SBUV V8 algorithm, the implementation details differ significantly. A key difference between

the two algorithms is that the OMI algorithm will take advantage of the hyperspectral capability and higher signal-to-noise (at $\lambda > 300$ nm) of the instrument to improve the information content in the lower stratosphere and troposphere compared to SBUV. The OMI algorithm is based on the experience with GOME, which measures backscattered radiances at wavelength between 240 and 790 nm with 0.1-0.2 nm sampling (Burrows *et al.*, 1999). A number of teams have applied OE for GOME ozone profile retrieval, and there is also an algorithm based on Phillips-Tikhonov regularization [Chance *et al.*, 1997; Munro *et al.*, 1998; Van der A *et al.*, 1998; Hoogen *et al.*, 1999; Hasekamp and Landgraf, 2001]. All ozone profile retrieval algorithms for GOME use radiative transfer models (RTM) that simulate the total radiance (single plus multiple scattering) for a given atmospheric state. The algorithms differ mainly in the choice of RTM, though they all employ the scalar approximation (i.e., neglect polarisation). All algorithms utilise the higher spectral resolution of GOME and use hundreds of wavelengths compared to 10 for SBUV V8. The high spectral resolution and extension to 330 nm (compared to 318 nm for SBUV V8) allow these algorithms to take advantage of the large temperature dependence of ozone absorption cross-section in the Huggins band [Bass and Paur, 1985] to retrieve information about tropospheric ozone [Chance *et al.*, 1997; Spurr, 2001].

For OMI we have selected the LIDORTA RTM [van Oss & Spurr, 2001b] to compute the buv radiation. It has a fast and accurate linearisation scheme to compute the Jacobian with respect to the state variables. It is expected that this algorithm will be used at KNMI to process current GOME data as well as data from future instruments in the GOME series.

4.1.2. Processing Overview

The OMI ozone profile processing software uses level 1 radiance/irradiance as the primary input and provides the optimal estimate of the ozone profile and its associated retrieval diagnostics, as the primary output. Figure 4.1 shows the high-level flow diagram.

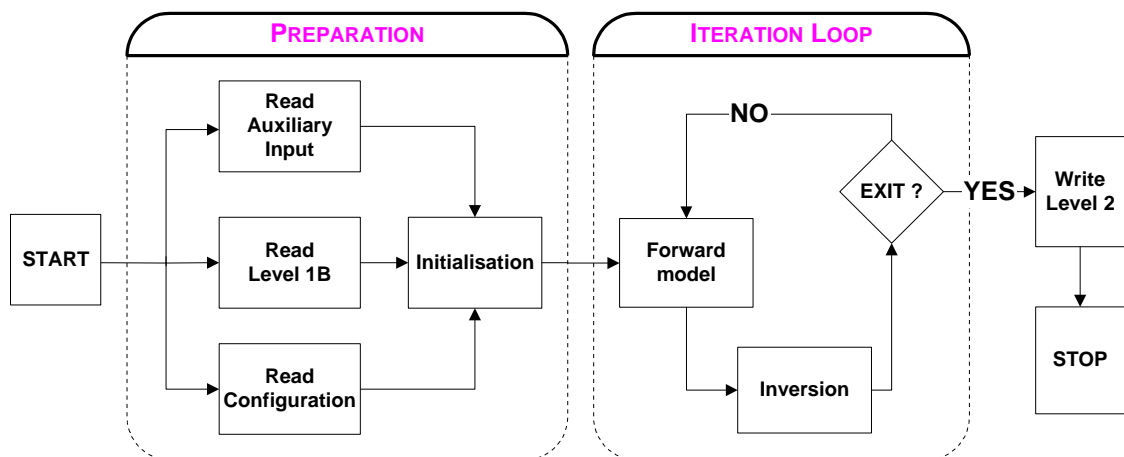


Figure 4.1 High level flow diagram of the KNMI ozone profile algorithm for OMI

Aside from the configuration input file (control and input settings for the algorithm), there are at least three auxiliary input files: (i) a short file containing cloud parameters generated by a separate OMI algorithm, (ii) one or more level 2 files of previously retrieved ozone profiles to be used as first-guess values, and (iii) real-time meteorological data from a numerical weather prediction model. In the Initialisation Step, forward model input data are assembled (atmospheric profiles, reference spectra, surface parameters, viewing geometry, instrument parameters), the

initial state vector is constructed, and the *a priori* state vector and error covariance matrix are selected. The Forward Model Step simulates the radiances as measured by OMI in the fitting window, and computes the Jacobian of these radiances with respect to state vector parameters. In the Inversion Step the next guess for the optimal estimate is computed (along with error statistics) from simulated radiances, Jacobian, *a priori* information plus statistics, and the measurement vector with its error statistics. The algorithm exits the iteration loop if convergence is achieved, but returns to the entry point of the iteration loop if not.

4.1.3. Product Description

The main level 2 product from this algorithm is the vector of ozone profile elements, given as layer ozone amounts in Dobson Units [DU] in 19 layers (Table 4.1). Associated with each retrieved profile, the product also contains the *a priori* profile, the prior error covariance, the solution (posterior) error covariance (the main diagnostic), and the averaging kernel matrix. Comparing prior and posterior covariances enables the user to assess the information added by measurements, while the averaging kernels provide information on the vertical resolution of the reported profile. Other diagnostics (Table 4.2) will include residuals at 5 nm wide wavelength bands, the final RMS and cost function values and the number of iterations. From the Scientific Requirements Document (SRD) [Levelt *et al.*, 2000], the accuracy requirements are 10% (stratosphere) and 30% (troposphere), with vertical resolution 5 km and 10 km, respectively. A number of auxiliary parameters will also be in the product, including the tropospheric aerosol optical depth, surface albedos, NO₂ total column density, cloud fraction values and a Ring spectrum parameter. In addition, some reference information (surface pressure, for example) and quality control flags will be supplied.

The auxiliary parameter values are not to be considered as ‘optimal-quality’ OMI products since the current retrieval method and spectral window choice are optimised for the ozone profile and not for the auxiliary parameters. Their values are included in the product because they are part of the state vector and we deem it necessary to provide full information on the retrieval result.

Close to nadir the level 2 product will be specified for ground pixels of size 50x50 km²; this footprint represents an average of three OMI UV1 scenes in the flight direction, slightly exceeding the requirement in [Levelt *et al.*, 2000]. For off-nadir observations the ground pixel will be larger in the across-track direction. With the 2600 km OMI swath, global coverage is achieved in one day under normal operating conditions; the product will also be generated for the spatial zoom-in mode of viewing. Geolocation information for the level 2 product will be taken selectively from level 1 values, taking into account the scene averaging.

Table 4.1 Main output products of the ozone profile algorithm

PRODUCT	UNITS	DIMENSIONS
Ozone profile	DU	19 layers
Error on Ozone profile	DU	19 layers
Error correlation coefficients	Unitless	171 values
Averaging Kernel	Unitless	19 x 19 layers
A priori ozone profile	DU	19 layers
A priori error on ozone profile	DU	19 layers
A priori Error correlation coefficients	Unitless	171 values

Table 4.2 Auxiliary output products of the ozone profile algorithm

PRODUCT	UNITS	DIMENSIONS
Fit residuals	Unitless	12 values
RMS of fit	Unitless	1 values
Cost function of fit	Unitless	1 values
Number of iterations	Unitless	1 values
NO₂ total column	DU	1 value
SO₂ total column	DU	1 value
Effective cloud fraction: UV1	Unitless	1 value
Effective cloud fraction: UV2	Unitless	1 value
Cloud top pressure	hPa	1 value
Effective surface albedo	Unitless	1 value

4.2. The forward model

4.2.1. Introduction

The forward model consists of two parts: (1) the radiative transfer model (RTM) that computes the radiances at the entrance of the instrument, (2) the instrument model (IM) that simulates the OMI level 1 radiance values derived from the calibration of raw data taken by the OMI instrument. The RTM has two parts. The single-scattering component and its Jacobian are computed separately using high vertical resolution ozone profiles. The multiple scattering component is computed at lower vertical resolution using LIDORTA- an RTM developed specifically to permit fast computation of radiances and the Jacobian for a nadir-viewing UV instrument. The latter have traditionally been estimated by finite-difference methods, but recent developments in radiative transfer theory [Rozanov *et al.*, 1998, Spurr *et al.*, 2001] have allowed Jacobians to be evaluated by analytic means. LIDORTA implements the linearised discrete ordinate radiative transfer theory developed by Spurr [2001]. It is a specialised adaptation of the more general LIDORT code. The main difference between the codes is that LIDORTA employs analytic solutions for the four- and six-stream options [van Oss & Spurr, 2001b].

In the following we describe the atmospheric set-up for the RTM (4.2.2), followed by a description of the single scattering RTM and the LIDORTA RTM (4.2.3). In this section we also deal with accuracy and optimisation aspects of the RTM. In Section 4.2.4, we describe the Instrument Model.

4.2.2. Atmospheric state input to the RTM

For input, the RTM requires the following: a pressure grid, atmospheric profiles and cross-sections of trace gases (ozone and interfering species such as NO₂ and SO₂), aerosol profiles and optical parameters, surface reflection parameters, cloud parameters, solar and viewing polar and azimuth angles, the wavelength grid and the solar irradiance at these wavelengths. The vertical grid is consist of 19 layers with bottom pressures at 1000, 700, 500, 300, 200, 150, 100, 70, 50, 30, 20, 10, 7, 5, 3, 2, 1, 0.5, and 0.3 hPa. The actual surface pressure replaces the nominal 1000 hPa level. For cloudy and partially cloudy scenes, the cloud-top pressure replaces the nearest pressure level.

Trace Gas Databases

For ozone distributions, the basic source is the global climatology of Fortuin & Kelder [1999], which provides ozone mixing ratios at 19 pressure levels for each month at 17 latitude

bands. It also provides full error statistics. The current baseline for the ozone cross section reference spectrum is the temperature-parameterised data set of *Bass & Paur* [1985], corrected according to *Chance* [2001] and *Orphal* [2001]. For NO₂ and SO₂, we take an initial distribution profile from the AFGL data set [*Anderson et al.*, 1986]. NO₂ cross-sections are taken from the reference data set of *Vandaele* [1998], SO₂ cross section from the HITRAN molecular database [*Rothman et al.*, 1992]. For Rayleigh cross sections and depolarisation values, empirical formulae are used based from *Bates* [1984].

Aerosols

The LOWTRAN 7 [*Berk et al.*, 1989] database of aerosol models is used in the forward model. Database vertical profiles of aerosol optical properties (optical thickness, single scattering albedo and phase function moments) are interpolated to the RTM pressure and wavelength grids. The aerosol regime is selected based on surface type (land or ocean), season and lower atmosphere humidity profile.

Temperature/humidity

The temperature profile is required for the determination of ozone cross sections. It is not used to calculate layer optical thickness values; in hydrostatic equilibrium, the pressure difference can be related directly to the column number density of air. Humidity is needed to select the proper tropospheric and boundary layer aerosol models, and also to calculate the molecular mass of air in the equation of hydrostatic equilibrium. Forecast global fields for both these quantities are available from numerical weather prediction models.

Clouds

We expect to get cloud top pressure and an initial cloud fraction from the OMI cloud retrieval algorithm. The treatment of clouds in the forward model assumes a Lambertian reflective surface at cloud top for the cloudy fraction of the pixel. The cloud-top albedo is fixed at 80%. We assume that cloudy and clear parts of a pixel do not exhibit significant 3-D radiative transport effects and thus are treated independently. The influence of polar stratospheric clouds (PSC) on the retrieval needs further study. However, as is indicated elsewhere in this ATBD (total ozone DOAS retrieval) the chance of encountering PSCs that may potentially hamper the retrieval (thick PSCs above the ozone maximum) is very low. If the presence of such clouds is detectable, the ozone profile will be flagged as suspect in such cases.

Surface

For the surface reflectance condition, the baseline RTM treatment assumes a Lambertian reflecting surface over land. Initial and *a priori* values are taken from a surface albedo database [*Herman and Celarier*, 1997]. The surface pressure will be taken from meteorological forecast data and will be taken as the lowest retrieval level. The ground height (from a topographical database) is also required.

4.2.3. Radiative transfer model (RTM)

Given the atmospheric profiles and the cross sections, a set of optical parameters is defined for each layer; this set constitutes the basic input to the radiative transfer model for a single wavelength. These optical parameters are: layer optical thickness and single scattering albedo, and a sufficient number of phase function expansion coefficients. The RTM further requires the solar irradiance at each wavelength to compute the earth radiance. The radiative

transfer problem is solved using separate models for the single and multiple scattered components.

Single-scattering RTM

The single-scattered radiance at TOA and the associated Jacobian is computed using an analytic solution that includes the attenuation due to the spherical shell atmosphere along the photon path [*van Oss & Spurr, 2001b*]. The phase function is specified to high accuracy by using a sufficient number of phase function moments. This procedure is similar to the *Nakajima-Tanaka* correction [1988], included in the latest DISORT version (version 2).

Multiple-scattering RTM

The LIDORTA [*van Oss & Spurr, 2001b*] discrete-ordinate RTM is used for the multiple scattering computations. In an atmosphere divided into a number of optically uniform adjacent layers, the radiative transfer equation (RTE) is first solved for each layer; this is followed by the application of boundary conditions to match the radiation field at layer interfaces. The atmosphere is illuminated by a downward-directed parallel beam of sunlight. The diffuse radiation (excluding the attenuated direct solar beam) is solved for the whole atmosphere. Atmospheric sphericity effects on the direct beam attenuation are treated with the pseudo-spherical "average secant" approximation [*Caudill et al., 1997, Spurr, 2001*]. Polarisation is not considered in the RTE solution. A separate look-up table, described later, is used to correct for this neglect.

For a given wavelength λ we define for each layer p (where $p = 1, \dots, P$): ω_p , the single scattering albedo (ratio of the total scattering and extinction coefficients); $\Delta\tau_p = \tau_p - \tau_{p-1}$, the layer optical thickness for total extinction. τ is the vertical co-ordinate; τ is zero at the top of the atmosphere. Each atmospheric layer is further characterised by a set of phase function Legendre moments $\mathbf{b}_{l,p}$. The RTE for unpolarised diffuse light is:

$$\begin{aligned} \mathbf{m} \frac{dI(\mathbf{m}, \mathbf{f}, t)}{dt} &= I(\mathbf{m}, \mathbf{f}, t) - J(\mathbf{m}, \mathbf{f}, t) \\ J(\mathbf{m}, \mathbf{f}, t) &= \frac{w}{4p} \iint P_s(\mathbf{m}, \mathbf{f}, \mathbf{m}', \mathbf{f}') I(\mathbf{m}', \mathbf{f}') d\mathbf{m}' d\mathbf{f}' + \\ &\quad \frac{w}{4p} P_s(\mathbf{m}, \mathbf{f}, -\mathbf{m}_0, \mathbf{f}_0) I_0 \exp(-st) \end{aligned} \quad [4-1]$$

where \mathbf{m} is the cosine of the polar angle, \mathbf{j} is the azimuth angle and P_s is the phase function for scattering. The source function J comprises the scattered diffuse radiation (first term) and the primary scattering (second term). The direct solar beam has extraterrestrial irradiance I_0 , polar direction $-\mathbf{m}_0$ and azimuth \mathbf{j}_0 . The factor σ in the exponential is the average secant multiplier that accounts for the attenuation of the solar light in a spherical-shell geometry.

Eq. [4-1] is solved by first expanding the diffuse intensity field and the phase functions in a Fourier series in the cosine of the relative azimuth angle $\mathbf{j} - \mathbf{j}_0$, and then by approximating the polar angle integration of the diffuse scatter term with a summation using a double-Gauss quadrature scheme [*Chandrasehkar, 1960*]. We use N to denote the number of half-space streams in the summation. For one Fourier term in the general case, the resulting set of coupled linear differential equations is usually solved using standard numerical packages [*Stamnes et al., 1988*]. For $N=2$ and $N=3$ (the 4- and 6-stream cases), the RTE solutions can be written down directly without recourse to numerical tools [*van Oss & Spurr, 2001b*].

Solutions for all layers are combined using a set of boundary conditions: (a) continuity of the radiance field at layer interfaces, (b) no downwelling diffuse light at TOA, and (c) a Lambertian reflectance condition at the bottom of the atmosphere (BOA). The resulting linear system for the unknown integration constants is solved with the help of special band-matrix LU-decomposition routines from the LAPACK suite [Anderson *et al.*, 1995]. This completes the discrete ordinate solution at quadrature directions and at every optical depth in the atmosphere. To derive the radiance at TOA at an arbitrary viewing direction (\mathbf{q}, \mathbf{f}) , we substitute the discrete ordinate solution at the quadrature streams in the multiple scatter integrals in the original RTE, and integrate the latter. The result is:

$$I(0, \mathbf{m}, \mathbf{f}) = I_{surf}(\mathbf{t}_p, \mathbf{m}, \mathbf{f})e^{-\tau_p/m} + \sum_{p=1}^P \Lambda_p(\mathbf{m}, \mathbf{f})e^{-\tau_{p-1}/m} \quad [4-2]$$

Expressions for the source term Λ_p in layer p may be found in literature [Stamnes *et al.*, 1988]. In the first term, the upwelling radiance I_{surf} at BOA follows directly from the surface boundary condition.

Computation of Jacobians

The retrieval requires the Jacobian of the TOA radiance with respect to all elements of the state vector. These state elements influence the radiance through their effect on the optical input parameters (the vertical grid of optical thickness, single-scatter albedo and phase function moments). We define the state vector element x_q (x_q might be the ozone partial column in that layer, or e.g. the aerosol optical thickness) affecting the optical input parameters in layer q only. We write down the explicit derivative of Eq. [4-2]:

$$\frac{\partial I(0, \mathbf{m}, \mathbf{f})}{\partial x_q} = \frac{\partial}{\partial x_q} \left\{ I_{surf}(\mathbf{t}_p, \mathbf{m}, \mathbf{f})e^{-\tau_p/m} + \sum_{p=1}^P \Lambda_p(\mathbf{m}, \mathbf{f})e^{-\tau_{p-1}/m} \right\} \quad [4-3]$$

Using the chain rule for differentiation, this derivative can be written as a function of the derivatives of the surface radiance, the optical thickness values and the layer source functions. Further repeated applications of the chain-rule then express these components in terms of the derivatives $\frac{\partial \mathbf{D}\mathbf{t}_p}{\partial x_p}$, $\frac{\partial \mathbf{w}_p}{\partial x_p}$ and $\frac{\partial \mathbf{b}_{l,p}}{\partial x_p}$ which express the basic variation in atmospheric optical properties. These derivatives are the basic input for the model, depending on the specific choice of x_q .

Because of the linearity of the discrete ordinate equations, it can be shown that the boundary value problem for the derivatives of the integration constants and the constants themselves is essentially the same; only the right-hand source vector is different. Integration constant derivatives are then simply found by back-substitution; there is no need for further matrix inversion. The Jacobian can be determined exactly without any additional numerical computation other than that used to determine the original radiance solution; the RTM needs to be called just once to deliver the complete set of radiance derivatives in addition to the radiance itself. This represents a very substantial saving in computational effort compared with the repeated calls to the RTM required to calculate Jacobians using finite-difference methods. Also, since the Jacobian solution is analytic, there are no problems about accuracy that often arise when dealing with ad-hoc finite-difference estimates. Further details on the linearisation procedure and the derivation of Jacobians can be found in [Spurr *et al.*, 2001] for the general N -stream case, and [van Oss & Spurr, 2001b] for the faster 4 and 6-stream analytic solutions.

Sphericity correction at large viewing angle

OMI has an instantaneous viewing angle of 114° at the satellite, corresponding to a swath width of 2600 km. For large off-nadir viewing directions, the ordinary pseudo-spherical calculation is insufficiently accurate for viewing zenith angles greater than about 30° - 35° . To remedy this, we must employ source function integration as in Eq. [4-2], but along the line-of-sight instead of the vertical. A straightforward sphericity correction procedure has been developed for this situation [*van Oss & Spurr, 2001b*]. The technique is similar to that found in *Caudill et al. [1997]*. The exact single scatter radiance/Jacobian solutions are found explicitly for all solar rays scattering once into the line-of-sight. LIDORTA multiple scatter source function contributions and derivatives are calculated for the geometries at the start and finish of the atmospheric line of sight path; values for other points are interpolated with no significant loss of accuracy. The default will be to use this correction for all viewing directions; this ensures consistency and avoids possible spurious radiance jumps.

Polarisation Correction

Ideally, radiative transfer in the UV/visible should be modelled using the full Stokes 4-vector representation. It has been shown that the scalar RTM approximation (only the intensity component of the Stokes vector) introduces errors up to 10% for the radiance at TOA [*Mischenko et al., 1994, Stammes, 1994, Lacis et al., 1998*]. The error is largest when solar and viewing directions are at right angles. The effect of this error source on retrieved ozone profiles is large enough to require a correction for the polarisation RTM error (see Section 4.5.3). A full-Stokes RTM that generates simultaneous radiances and Jacobians is currently not available. Vector RT models are presently too time-consuming to be useful in an operational algorithm such as the present one for OMI (~16 times slower for the full Stokes vector treatment). For OMI, we use the scalar LIDORTA model, with a lookup table containing polarisation errors for all relevant conditions to be encountered. A doubling/adding vector model [*de Haan et al. 1987*] is used to construct the look-up table; entries are expressed as the relative difference in the radiances computed in the 4-vector and scalar-only treatments. The operational prototype look-up table will be classified by geometry (5 values for the scattering angle, 4 for the solar zenith angle), surface albedo (4 values), surface pressure (2 values) ozone profile (20 global profiles for 4 seasons and 5 latitude zones), total ozone (2 values for every global profile) and finally 40 wavelengths between 290 and 330 nm spaced at 1 nm. After correction, there is a residual radiance error due to the unknown profile shape. This error reaches a maximum of 0.3% around 320 nm. The effect on the profile accuracy is discussed in the error analysis section (4.5).

Ring effect

As described in Chapter 1, the Ring effect produces spectral structure in the TOA reflectance spectrum that must be accounted for. Initially, we propose to use a pre-calculated Ring spectrum derived from a high-resolution solar reference spectrum [*Chance & Spurr, 1997*]. Amplitude for the Ring spectrum is included as an auxiliary parameter in the state vector. More accurate characterisation of the Ring effect by a suitable forward model calculations [e.g., *Vountas et al., 1998*] may be added later.

4.2.4. Instrument Model

The IM operates on radiance (and Jacobian) spectra at the entrance of the instrument as simulated by the RTM and its linearisation. In the OMI algorithm we use:

$$S_i = P_{add}^n(I') + P_{mul}^m(I') \int_{\Delta I} dI \int_0^{\infty} dI' R_i(I, I') I(I'). \quad [4-4]$$

Where, S_i is the radiance value for spectral pixel i as it will appear in the level-1 product, ΔI is the spectral bin size, R_i is the instrument response function, and P_{add}^n and P_{mul}^m are low-degree polynomials in wavelength accounting for possible additive and multiplicative errors. The multiplicative polynomials will correlate strongly with continuum-type signatures due to smooth particulate scattering or surface reflectance; for this reason we will not consider it in first prototype. For the additive polynomial, we take a linear form (offset and tilt); this is subject to verification pending the use of real data. Details of the response functions await results from calibration measurements of the instrument. For the error analysis in Section 4.5 we have used a flat-top form: $R(I, I') \sim 2^{-x}$, $x = (2(I - I')/FWHM)^4$, with $FWHM$ as specified in [Fokker Space, 2000].

4.3. Inverse model

4.3.1. The problem of inversion

When the number of profile elements to be retrieved exceeds the number of independent profile elements that can be retrieved, a naive least squares fitting produces meaningless results for real and noisy spectra. Small-scale variations in atmospheric quantities that are poorly constrained by the measurement will cause noise amplification, resulting in spurious retrieved values often showing strong oscillations. Two methods for circumventing this ill conditioning can be distinguished: (i) limiting the number of profile elements to be retrieved, and (ii) regularising the inversion problem. The first option can be realised by fitting profile elements at a limited number of carefully chosen levels in accordance with the restricted profile information in the measurement. This would require a specification of the shape of the profile between the layers. The use of a fixed vertical grid would be non-optimal for most cases.

Regularisation suppresses noise amplification by using information from a source other than the measurement. Regularisation is achieved by adding a second term to the least squares cost function J to be minimised:

$$J = (\mathbf{y}_m - F(\mathbf{x}))^T S_y^{-1} (\mathbf{y}_m - F(\mathbf{x})) + R(\mathbf{x}) \quad [4-5]$$

Here, \mathbf{y}_m is the measurement vector of radiances, \mathbf{x} is the state vector of parameters to be retrieved, $F(\mathbf{x})$ is the radiance calculated by the forward model and S_y is the error covariance matrix. $R(\mathbf{x})$ is some function of the state that returns a large amplitude for 'undesirable' solutions. Two choices for the regularisation are commonly used for atmospheric retrievals; these are the Phillips-Tikhonov [Hasekamp & Landgraf, 2001] and Optimal Estimation (OE) methods [Rodgers, 2000]. In OE, the $R(\mathbf{x})$ term is derived from the application of Bayes' theorem. This states that the probability density function (PDF) of the state is proportional to the PDF of the measurement given the state, multiplied by the PDF of the state prior to the measurement. The measurement changes the likely outcomes for the state vector elements, since it provides extra information on top of that already available from prior information. When the PDFs are all Gaussian distributions, the most probable state (the Optimal Estimate) minimises the cost

function Eq. [4-5] with the regularisation term: $R(\mathbf{x}) = (\mathbf{x} - \mathbf{x}_a)^T S_a^{-1} (\mathbf{x} - \mathbf{x}_a)$. Here \mathbf{x}_a is the *a priori* state vector and S_a the prior covariance matrix.

4.3.2. Finding the Optimal Estimate

The optimal estimate minimises the cost function with the regularisation term: Eq. [4-5]. This value can be found by iteratively applying:

$$\begin{aligned} \mathbf{x}_{i+1} &= \mathbf{x}_a + D_y [\mathbf{y}_m - \mathbf{y}_i - K_i (\mathbf{x}_a - \mathbf{x}_i)] \quad \text{with} \quad D_y = S_{i+1} K_i^T S_y^{-1} \quad \text{and} \\ S_{i+1} &= (K_i^T S_y^{-1} K_i + S_a^{-1})^{-1} \end{aligned} \quad [4-6]$$

where $K_i = (\partial F / \partial \mathbf{x})_i$ is the Jacobian at state \mathbf{x}_i ; K^T the transpose of the Jacobian, $\mathbf{y}_i = F(\mathbf{x}_i)$ and \mathbf{x}_{i+1} is the updated state vector. The matrix D_y is known as the matrix of contribution functions; the solution error covariance is given by S_{i+1} . The iteration starts with some initial estimate of the state, and terminates when convergence has been reached. We employ two convergence criteria. The primary criterion is that the difference between the error-weighted lengths of two consecutive state vectors, i.e. $S_x^{-1/2} (\mathbf{x}_i - \mathbf{x}_{i-1})$, should be below a fixed threshold. Investigations have shown that a maximum difference of 1% in gives good results for all cases. The second convergence criterion to be met is that the change in the cost function between two consecutive iterations should be less than some predefined value. We have adopted 1%, which appears to work fine. These two criteria combine convergence tests in both state space and measurement space. The final value of the solution error covariance matrix is the main source of diagnostic information for the retrieval.

The actual computation of the optimal estimate is performed by using linear transformations $\mathbf{x}' = V^T S_a^{-1/2} (\mathbf{x} - \mathbf{x}_a)$ and $\mathbf{y}' = U^T S_y^{-1/2} (\mathbf{y}_m - \mathbf{y}_i)$, where U and V are unitary matrices resulting from the singular value decomposition (SVD) of the scaled Jacobian: $K' = S_y^{-1/2} K S_a^{1/2}$. In terms of primed variables, elements of the optimal estimate vector are given by:

$$x'_{\text{OE},j} = \frac{\mathbf{I}_j y'_j + x'_{j,a}}{\mathbf{I}_j^2 + 1} \quad [4-7]$$

Here, \mathbf{I}_j are the singular values resulting from the SVD. A useful measure of the number of independent linear combinations of the state vector elements that can be retrieved from the addition of measurements is given by the degrees-of-freedom-for-signal (*DFS*) indicator, defined by:

$$DFS = \sum_j \frac{\mathbf{I}_j^2}{1 + \mathbf{I}_j^2} \quad [4-8]$$

If N is the dimension of the state vector, we have $DFS = N$ if the measurement completely determines the state, and $DFS = 0$ if there is no information at all in the measurement.

4.4. Implementation of the operational algorithm

4.4.1. Level 1B Input and Usage

The basic level 1B data comprise a calibrated solar spectrum and spectra of calibrated geolocated radiances; each spectrum comes with a wavelength grid, error estimates and status flags. In the geolocation record, solar and line-of-sight viewing angles are specified at the

spacecraft, satellite height and earth radius are specified for the sub-satellite point, and for each nadir-view footprint, only the centre co-ordinates (surface latitude and longitude) are given.

As noted in Section 4.1.3, radiance spectra from three UV1 ground pixels will be co-added in the flight direction; the measurement noise is effectively reduced by a factor of $\sqrt{3}$. Since the algorithm uses information from the wavelength region between 270 and 330 nm, it is necessary to combine information from the UV1 channel (270-310 nm) and the UV2 channel (310-365 nm). Along the swath, these channels have different ground pixel sizes; a UV1 pixel is roughly -- but not exactly -- twice the size of a UV2 pixel [*Fokker Space, 2000*]. Therefore, two UV2 pixels will not fit in a single UV1 pixel. From the spectra of the two or three UV2 pixels that partially overlap a UV1 pixel an area-weighted average spectrum is constructed and used in the retrieval. The L2 cloud product will help in providing a good first guess for the effective surface albedos for each of the ground pixels.

The South Atlantic Anomaly (SAA) is expected to cause an increase in the number of transient pixels in an exposure. These pixels will be flagged in the level 1B product and will not be taken into account in the ozone profile algorithm. The reduced number of useful wavelengths in the spectrum will decrease the amount of information as e.g. expressed in the DFS.

4.4.2. Determination of measurement error covariance

It is important to realise that the error covariance S_y , introduced in Eq. [4-5], includes both the measurement noise and modelling errors. If modelling parameters influence the sensitivity of the retrieval of ozone, one can either put them in the state vector or include them in the error covariance. For a single retrieval these approaches are equivalent [*Rodgers, 2000*]. However, if systematic errors are constant in time, their contribution to the ozone retrieval error can be reduced.

In the remaining part of this chapter we will use the abbreviation MME (Modelling and Measurement Error) for this combined error. Ignoring the modelling error would put too much weight on the measurement term in the cost function Eq.[4.5] and give an incorrect retrieval result. We refer to the section on the error analysis (4.5) for more details and for more realistic estimates for these errors, which are specified for the OMI ozone profile retrieval.

4.4.3. Definition of the state vector and a priori

The state vector elements describing the ozone profile are the 19 values: $x_i = \log[c_i/c_{i,a}]$ defined on the pressure grid. Here, c_i is the partial column of ozone in layer i , $c_{i,a}$ is the *a priori* value. The logarithm in the definition of these elements is based on the log-normal shape of the *a priori* ozone variability; furthermore, it is most suited to the assumption of Gaussian statistics for the *PDFs*.

There are 6 other atmospheric state vector elements: 1 surface albedo, 2 effective cloud fractions, 1 NO₂ total column density and 1 SO₂ total column density, and 1 tropospheric aerosol optical depth. We also include 1 Ring spectrum parameter and 2 coefficients for the additive instrument polynomial; there are 9 auxiliary parameters and 28 elements in total. Separate effective cloud fractions are required for each OMI channel. This adjustment is necessary mainly because of the scene-mixing that occurs with the juxtaposition of OMI UV1 and area-averaged UV2 footprints. Radiance differences due to these spatial aliasing effects can be up to a few percent in case of rapidly varying radiances along the swath (e.g. due to clouds). If left uncorrected, this can result in errors of tens of percents in the tropospheric ozone profile. We deal with this by allowing the state vector to contain two separate cloud fractions, one for each channel.

For initial values of the ozone profile elements, we use a previously retrieved profile read in as part of the auxiliary data. For initial values of the other atmospheric state vector elements,

we use the atmospheric state inputs defined in Section 4.2.2. The initial cloud fractions for both channels are taken to be the averaged UV2 value obtained from the appropriate cloud retrieval results read in as auxiliary input. Initial values for the Ring parameter and the additive polynomial coefficients are all zero.

For the *a priori* ozone profile, we use the data of *Fortuin & Kelder* [1999]. Since the standard deviations are not included in this climatology, we defer to an older version [*Fortuin & Langematz*, 1995] to obtain the diagonal elements of the covariance matrix. For the cross-correlations we use a fixed matrix for all months and latitudes based on a re-examination of the source data of the climatology [*Timmermans*, 2000]. For the errors in the auxiliary parameters, we use 50% for the NO₂ column, 50% for the aerosol optical depth, 50% for the surface albedos and 20% for the cloud fractions (all figures TBC). For the remaining auxiliary parameters, 50% relative *a priori* error is assumed. *A priori* errors on all auxiliary parameters are assumed uncorrelated with each other, and also uncorrelated with any of the ozone profile elements.

4.4.4. Performance Considerations

Forward Model Efficiency

LIDORTA is fast and efficient with $N = 4$ or 6 discrete ordinate streams (CPU varies roughly with N^2); the use of analytic discrete ordinate solutions also improves the efficiency. For the vast majority of atmospheric scenarios relevant to OMI ozone profile retrieval, four streams are usually sufficient to ensure that radiances and weighting functions are calculated to a level of accuracy that matches the measurement uncertainty. In scenarios where there is a strong aerosol presence in the troposphere, and for retrievals that use wavelengths beyond 320 nm, the six-stream option is necessary to achieve accuracy levels of 0.5% for radiances.

For shorter wavelengths in the UV where single scatter dominates (<295 nm), a minimum of 20 layers per pressure decade is required for single scatter radiance errors <0.1%. The 19-layer pressure grid is too coarse to achieve the desired accuracy: this is due to the occasional large differences between optical parameters at adjacent layers. This violates the assumption that the layers can be approximated as being homogeneous. To remedy this, each layer is split into a number of sub-layers and the optical parameters at the sub-layers are found by linear interpolation.

For the multiple-scatter LIDORTA computation, the 19 retrieval layers give the required accuracy level for the wavelength ranges and atmospheric and viewing conditions relevant to this algorithm. Since the speed of a LIDORTA run is proportional to the cube of the number of layers, the use of a coarse grid for multiple scatter represents a large gain in computational speed. Furthermore, an efficient calculation of radiances from the clear and clouded parts of the pixel has been implemented in the LIDORTA code; discrete ordinate RTE solutions for all layers above the cloud top are required for both calculations, and need to be computed once only (CPU saving of ~25%). Finally, calculations for multiple geometries as required for the sphericity correction for large off-nadir viewing angles are also performed with minimum redundancy.

Fitting Window; size and binning

At short wavelengths (270-300 nm) the broad shape of the reflectance spectrum contains information on the vertical distribution of ozone; pixel radiances over several neighbouring wavelengths can be averaged without compromising the retrieval. This binning step significantly decreases the number of simulations required by the forward model. For the majority of the scenes, averaging 7 spectral pixels introduces no significant loss of accuracy.

Above 300 nm, ozone cross-sections exhibit spectral fine structure superimposed on a slowly decreasing component; here, application of wavelength binning would result in significant loss of information and we make full use of the spectral resolution of OMI.

The DFS indicator Eq.[4.8] can be used to optimise the upper wavelength limit of the fitting window [van Oss & Spurr, 2001a]. Figure 4.2 shows DFS values plotted against upper wavelength limit for two solar zenith angles with two different temperature profiles: a tropical and an Antarctic profile. Also, the decrease of the DFS, in case a realistic value for the MME (taking into account calibration and model errors) is taken instead of only the instrument noise, is shown. The lower wavelength limit is fixed at 270 nm. There is a substantial increase in information with the inclusion of wavelengths above 300 nm, and the tropospheric temperature sensitivity becomes apparent above ~ 313 nm. There is little increase in DFS beyond about 330 nm, suggesting that the inclusion of wavelengths above this threshold will not significantly enhance the retrieval.

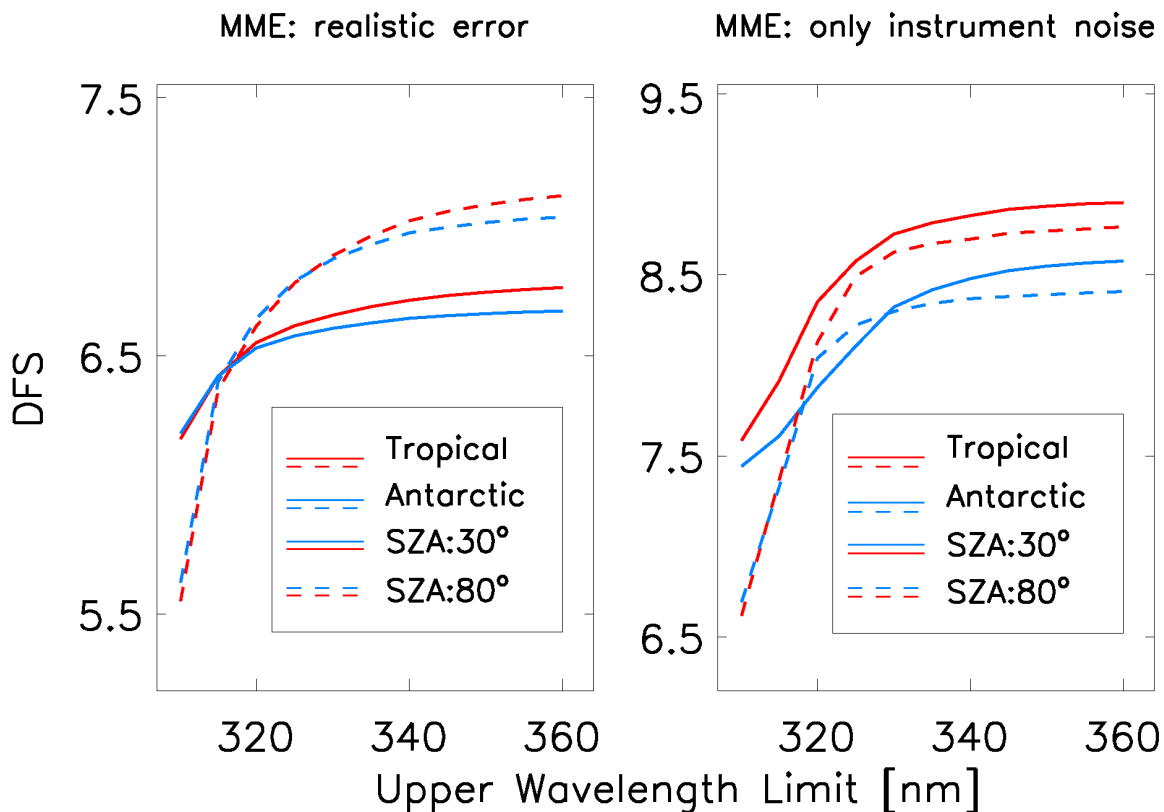


Figure 4.2 Degrees of Freedom for signal (DFS) as a function of upper wavelength limit, for two values of the solar zenith angle and two ozone profiles. The right panel treats the case where the measurement error consist of the instrumental noise only, whilst for the left panel the error has been increased by 0.5% of the radiance. We may conclude that beyond 330 nm no significant increase in DFS is seen and that the increase in measurement error limits the temperature sensitivity of the retrieval.

If the upper wavelength limit increases, the influence of other error sources on the retrieval increases. There is a trade-off between the extra information that is present in the spectra by considering longer wavelengths and the enhanced error due to these sources. The results of the error analysis (Section 4.5) allow us to make a sensible choice of upper wavelength of 330 nm.

Number of iterations

The number of iterations in the optimal estimation formalism is under most circumstances reduced by a judicious choice of the first guess profile; this is the reason for choosing a previously retrieved value for an adjacent scenario.

4.5. Error analysis

4.5.1. Sources of error in the retrieval

Following *Rodgers* [2000] we express the optimal estimate of the state x_{OE} in terms of the “true” value of the state vector x_{true} plus errors. This is accomplished by substituting $y_m = F(x_{true})$ in the asymptotic version of Eq. [4-6] (with $i \rightarrow \infty$) and linearising the forward model around the solution, giving:

$$x_{OE} \approx x_{true} + (A - I)(x_{true} - x_a) + D_y \mathbf{e}_y \quad [4-9]$$

The matrix $A = D_y K$ is the set of averaging kernels, and it connotes the sensitivity of the retrieval to the true state. I is the identity operator in state space. In a perfect retrieval the averaging kernels (rows of A) are delta functions; in real life, the width (FWHM) of these kernels is a measure of the vertical resolution of the profile retrieval. D_y is the matrix of contribution functions. The second term on the RHS of Eq. [4-9] denotes the *smoothing error*. The remaining error \mathbf{e}_y can be split into three components: $\mathbf{e}_y = \mathbf{e}_{me}$ (*measurement error*: random and systematic) + \mathbf{e}_{jme} (*forward model error*) + \mathbf{e}_{mpe} (*model parameter error*). These error components are mapped into profile errors by multiplication with the contribution functions.

The averaging kernels for scenario 2 (see Table 4.3) are plotted in Figure 4.3. Note that due to the definition of the state vector, the kernels give the relative variation of the *retrieved* ozone column in one layer due to a relative variation in the *true* value of another layer. The top panel shows the kernel for the 19-layer retrieval grid. Note that the kernels for the layers below 50 hPa do not look good: they do not peak at the right layer and show a large dependence on the profile around the ozone maximum. A better behaviour is obtained by adding several layers together, as shown in the bottom panel. The averaging kernels are shown for a new grid, consisting of 11 layers: the first six layers are grouped into a new bottom layer, layers 7, 8 and 9 are collected to form the next layer and layers 18 and 19 together form the new top layer. All other layers are left intact. The coarse-grid kernels illustrate the increase in quality of the retrieved profile when the tropospheric ozone values are added together.

Advanced users who require the maximum amount of profile information are advised to use the 19-layer retrieval result, the a priori values, the averaging kernels and the relation between them, given in Eq. [4-9]. Other users may not want to use the averaging kernels and are recommended to use the 11-layer grid layer ozone columns. The error covariances of the two grids are related through:

$$S_{11} = L S_{19} L^T, \quad [4-10]$$

with S_{11} the error covariance for the 11-layer grid and S_{19} for the 19-layer grid; L is the transformation matrix expressing the addition of ozone layer columns.

Smoothing Error

The smoothing error gives the difference between the true and retrieved state due to (i) limited vertical resolution of the retrieval (broad averaging kernels) and (ii) influence of the *a priori*. The contribution S_{se} to the solution covariance from this error component can be

estimated by using the *a priori* covariance matrix for the state covariance: $S_{se} = (A - I) S_a (A - I)^T$. The presence of smoothing error indicates that the retrieved profile is not an estimate of the true profile itself, but rather an estimate of a well-defined transformation of the true profile. When validating the retrieved profile, it is sometimes convenient to omit the smoothing error contribution. If so, this requires knowledge of the averaging kernels, the *a priori* and Eq. [4-9] to be able to relate the retrieval results to the truth.

Measurement error contribution

The effect of measurement error on the retrieved profile is given by $\mathbf{e}_{me} = (x_{OE} - x_{true})_{noise} = D_y \mathbf{e}_y$. The random (noise) contribution to \mathbf{e}_y generates a solution covariance component of the retrieval noise, $S_{noise} = D_y S_y D_y^T$, contributing to the retrieved profile error.

Model parameter errors

Retrieval error due to this source of uncertainty is given by $\mathbf{e}_{mpe} = (x_{OE} - x_{true})_{parameter} = D_y K_b \mathbf{D}b$, where K_b is the sensitivity of the forward model to the model parameter b and $\mathbf{D}b$ is the error in the model parameter itself. If $\mathbf{D}b$ is a random error, the solution error covariance component for this model parameter error is given by $S_{parameter} = D_y K_b S_b K_b^T D_y^T$. Model parameter errors can be both random and systematic.

Forward model errors

Here, the error on the profile is given by $\mathbf{e}_{fme} = (x_{OE} - x_{true})_{fme} = D_y \mathbf{D}f$, where $\mathbf{D}f$ is the forward model error due to an incorrect or inaccurate representation of the physics of the problem. This is a systematic source of error.

Non-orthogonality of errors

In addition to the partial ozone columns, the state vector includes additional parameters (see Section 4.4.3). The non-orthogonality of the individual partial columns is substantial, indicating that the retrieved values are not fully independent. This is expressed above in the smoothing error. Of interest is also the non-orthogonality between ozone and non-ozone elements in the state vector. As is the case of ozone itself, this can be studied by looking at the averaging kernels. At the time of writing, we are in the process of implementing additional state vector elements, so the extent of this non-orthogonality cannot yet be studied. If it is significant, it will be reported in the data product.

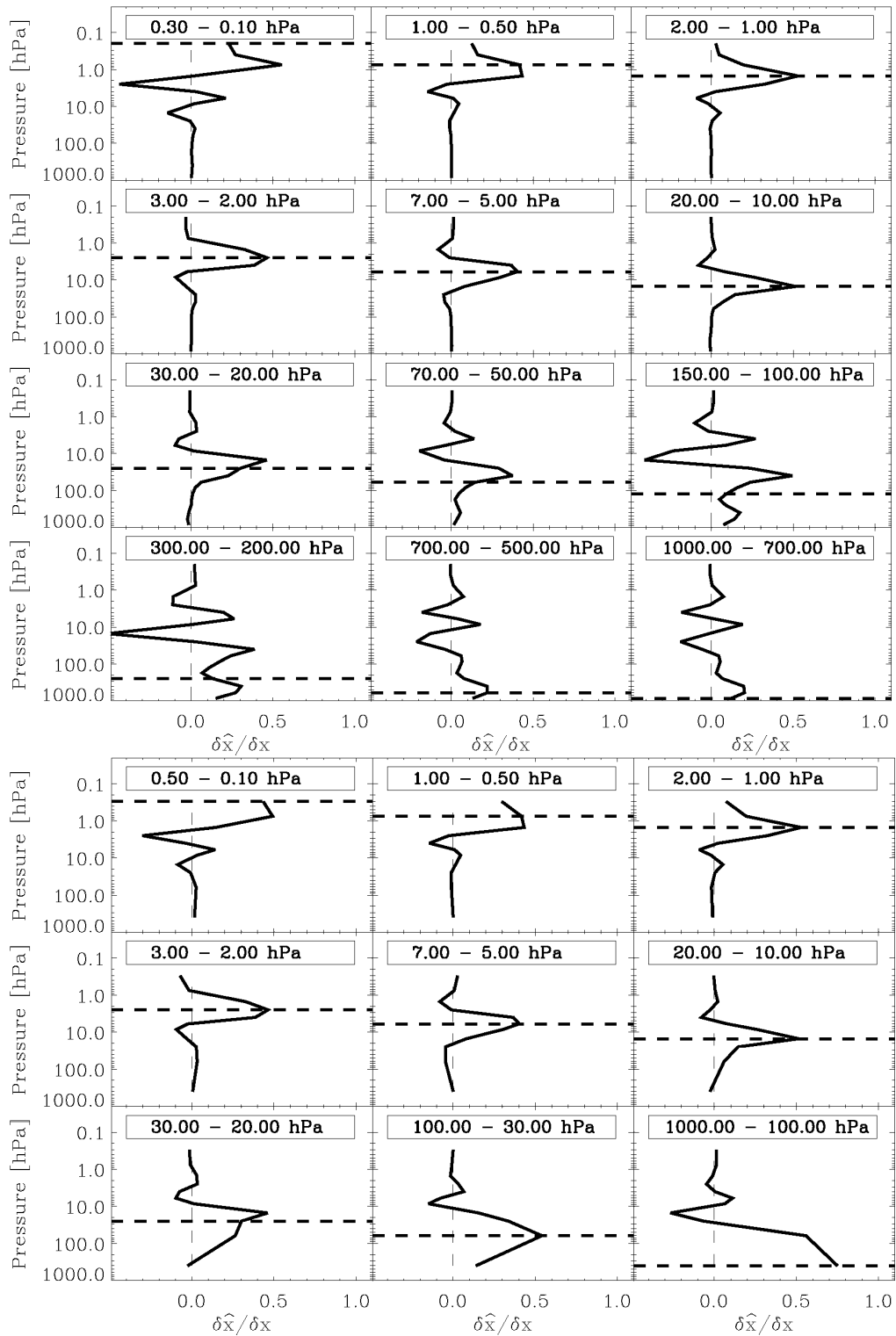


Figure 4.3 A selection of the averaging kernels for the 19-layer retrieval (Upper Panel) and for the profile on a coarse grid consisting of 11 layers (Lower Panel). The coarse-grid profile has been obtained by adding the 6 layers below 100 hPa, the two layers between 100 and 30 hPa and the two top layers. The other layers are unchanged. The averaging kernels for the coarse grid show the desired behavior – a small influence of ozone outside the layer on the retrieval –, whilst the tropospheric kernels of the original grid indicate that the tropospheric part of the retrieved profile cannot be interpreted without taking these kernels into account. The dashed horizontal line denotes the mid-level of the retrieval layer.

4.5.2. Test data set: Input configuration

For error assessments, we perform one inversion step of the optimal estimation loop in order to investigate the response of the retrieval system, given measurement and *a priori* statistics and other sources of error as noted above. The iterative update is not performed. To calculate errors, we require the matrices of averaging kernels and contribution functions from the inversion step, and Jacobians from the forward model step.

The error computation is performed for a number of representative cases that cover the full range of possible OMI measurements. We have: three cloud fractions 0.0, 0.2 and 1.0, two ozone profiles (AFGL- Tropical and - Mid-Latitude Winter), two solar zenith angles q_0 ² (30°, 80°), two relative azimuth angles f (0°, 180°) and two viewing angles q (10°, 50°). The following parameters are the same for all scenarios: surface albedo (0.05), cloud top albedo (0.8), cloud top pressure (700 hPa) and wavelength range (270 – 330 nm). This constitutes a total of 48 scenarios, listed in Table 4.3. *A priori* ozone profiles are selected from the climatology: latitude = 15°, month = March, for the Tropical profile and latitude = 45°, month = January, for the Mid-Latitude Winter profile. The state vector comprises only the 19 ozone partial columns and the surface albedo; for the purposes of this study, cloud fraction is treated as a model parameter.

Table 4.3 List of scenarios for error analysis. *p* denotes the type of AFGL standard ozone profile: *tro* (TROPICAL) and *mlw* (Mid-latitude Winter); *cf* stands for cloud fraction; the three angles f , q and q_0 are defined in the text.

	<i>p</i>	<i>cf</i>	f	q	q_0		<i>p</i>	<i>cf</i>	f	q	q_0		<i>p</i>	<i>cf</i>	f	q	q_0
1	tro	0	0	10	30	17	tro	1	0	50	30	33	tro	0.2	180	10	80
2	mlw	0	0	10	30	18	mlw	1	0	50	30	34	mlw	0.2	180	10	80
3	tro	0.2	0	10	30	19	tro	0	180	50	30	35	tro	1	180	10	80
4	mlw	0.2	0	10	30	20	mlw	0	180	50	30	36	mlw	1	180	10	80
5	tro	1	0	10	30	21	tro	0.2	180	50	30	37	tro	0	0	50	80
6	mlw	1	0	10	30	22	mlw	0.2	180	50	30	38	mlw	0	0	50	80
7	tro	0	180	10	30	23	tro	1	180	50	30	39	tro	0.2	0	50	80
8	mlw	0	180	10	30	24	mlw	1	180	50	30	40	mlw	0.2	0	50	80
9	tro	0.2	180	10	30	25	tro	0	0	10	80	41	tro	1	0	50	80
10	mlw	0.2	180	10	30	26	mlw	0	0	10	80	42	mlw	1	0	50	80
11	tro	1	180	10	30	27	tro	0.2	0	10	80	43	tro	0	180	50	80
12	mlw	1	180	10	30	28	mlw	0.2	0	10	80	44	mlw	0	180	50	80
13	tro	0	0	50	30	29	tro	1	0	10	80	45	tro	0.2	180	50	80
14	mlw	0	0	50	30	30	mlw	1	0	10	80	46	mlw	0.2	180	50	80
15	tro	0.2	0	50	30	31	tro	0	180	10	80	47	tro	1	180	50	80
16	mlw	0.2	0	50	30	32	mlw	0	180	10	80	48	mlw	1	180	50	80

4.5.3. Error analysis results

We report ozone profile errors for twelve retrieval layers (the first 5 tropospheric layers, then every other stratospheric layer), giving the scenario-averaged RMS.

Table 4.4 shows the smoothing and measurement error contributions to the ozone profile error. The measurement errors include: a wavelength shift of 1/30th pixel in UV1 and UV2, an offset error in the radiance with a magnitude of 2% of the radiance at 270 nm, and a multiplicative error of 1% in the radiance at all wavelengths. All these error sources are included in the overall accuracy assessment in Section 4.6.

Table 4.5 shows the errors in the retrieved profile due to model parameter errors. We consider errors in the Rayleigh cross section, the ozone cross section, the layer averaged temperature, the cloud top pressure, the aerosol optical thickness, the SO₂ amount in the boundary layer (BL) and in the stratosphere (due to volcanic eruption), and the NO₂ column.

² solar and viewing angles are defined at the instrument

Table 4.6 gives the profile errors due to errors in the radiative transfer model: the 4- and 6-stream approximation, neglect of Ring effect, neglect of polarisation and the residual error after the use of the polarisation look-up table.

All model parameter error sources, except the aerosol error, are included in the overall accuracy assessment. The magnitude of the aerosol optical depth error has led us to include the aerosol optical depth as an element in the state vector.

Figure 4.4 shows the four most important contributions to the total error: multiplicative calibration error, 6-stream forward model error, residual polarisation error and the error in the ozone cross section.

Figure 4.5 shows four large errors that are accounted for in the retrieval (4-stream, Ring and polarisation), or only occur under special circumstances (volcanic SO₂).

Table 4.4 List of smoothing error and measurement errors for indicated layers. Errors are given in percent. Errors included in the overall accuracy assessment are shown in **boldface**.

	1000- 700	700- 500	500- 300	300- 200	200- 150	100- 70	50- 30	20- 10	7- 5	3- 2	1- 0.5	0.3- 0.0
Smoothing	25.4	18.5	26.1	24.1	22.7	11.2	4.1	2.0	2.7	2.5	4.8	14.8
1-scale UV1 1/30 pix	3.2	3.4	5.4	4.9	3.4	1.8	1.1	0.5	0.3	0.2	0.1	0.1
1-scale UV2 1/30 pix	1.0	1.0	1.6	2.4	2.7	1.5	0.4	0.3	0.2	0.1	0.1	0.1
Radiance Offset 2% at 270	0.1	0.0	0.0	0.0	0.1	0.0	0.1	0.0	0.1	0.3	1.9	3.1
Radiance Multipl. 1%	2.8	2.8	3.5	2.7	1.6	1.3	0.9	0.9	1.3	1.6	2.0	1.9

Table 4.5 Profile errors due to model parameter errors. Errors are given in percent. In the first 8 rows, the errors are systematic. In the second 7 rows (below the dashed line), model parameter errors are regarded as random, and table entries here are the relative changes in standard deviations (square roots of the diagonal elements of the solution covariance) of the profile elements. In each case S_b is treated as diagonal with elements $(Db)^2$. Errors included in the overall accuracy assessment are shown in **boldface**.

	1000- 700	700- 500	500- 300	300- 200	200- 150	100- 70	50- 30	20- 10	7- 5	3- 2	1- 0.5	0.3- 0.0
Rayleigh Cross sect. 1%	0.4	0.4	0.7	0.9	0.9	0.5	0.3	0.4	0.9	1.2	1.3	1.1
Ozone Cross sect. 1%	1.8	2.0	3.6	2.8	1.6	2.0	1.8	0.6	0.3	0.5	0.5	0.5
Temperature 5K	1.0	1.0	1.2	0.6	0.6	0.4	0.1	0.1	0.1	0.3	0.5	0.4
Cloud-top 100 hPa	0.7	0.7	0.9	0.8	0.5	0.2	0.2	0.1	0.0	0.0	0.0	0.0
Aerosol opt. thickness. 20%	1.8	1.9	2.5	2.7	2.3	0.9	0.4	0.5	0.4	0.6	0.6	0.4
SO ₂ in BL 1DU	1.9	2.1	2.8	2.7	2.0	0.5	0.4	0.1	0.1	0.0	0.0	0.0
SO ₂ at 15 km 100 DU	685	785	1108	1142	896	303	163	61	35	17	8.5	21
NO ₂ column 0.5 DU	0.7	0.8	1.0	0.9	0.6	0.2	0.1	0.0	0.0	0.0	0.0	0.0
-----	-----	-----	-----	-----	-----	-----	-----	-----	-----	-----	-----	-----
Rayleigh Cross sect. 1%	2.6	2.8	6.0	7.4	7.7	3.9	1.7	1.2	1.5	1.2	1.1	2.3
Ozone Cross sect. 1%	2.3	2.4	3.5	3.9	4.0	2.8	1.9	1.6	1.8	1.6	1.5	2.2
Temperature 5K	0.9	0.9	1.4	1.4	1.3	0.7	0.3	0.3	0.3	0.3	0.3	0.6
Cloud-top 50 hPa	0.9	1.0	1.4	1.2	0.9	0.4	0.2	0.1	0.1	0.0	0.0	0.0
Aerosol opt. thickness. 10%	4.6	4.6	6.7	6.5	5.9	3.0	1.2	0.7	0.5	0.3	0.3	0.5
SO ₂ column 100%	0.8	0.8	1.2	1.1	0.9	0.4	0.2	0.1	0.1	0.0	0.0	0.0
NO ₂ column 100%	0.9	0.9	1.3	1.1	0.8	0.5	0.3	0.1	0.1	0.0	0.0	0.1

Table 4.6 Profile errors due to systematic forward model errors **Df**. Errors are given in percent. Both the 6-stream and the residual polarisation errors are included in the overall accuracy assessment. The magnitude of the 4-stream errors leads to the selection of the 6-stream model in the retrieval algorithm. The Ring effect will be accounted for by including a Ring parameter in the state vector. Errors included in the overall accuracy assessment are shown in **boldface**.

	1000- 700	700- 500	500- 300	300- 200	200- 150	100- 70	50- 30	20- 10	7- 5	3- 2	1- 0.5	0.3- 0.0
4-stream vs. 20-stream	7.3	8.7	16.9	19.7	17.3	6.2	3.2	1.7	0.8	0.4	0.2	0.4
6-stream vs. 20-stream	1.3	1.5	3.2	3.9	3.7	2.0	0.9	0.5	0.2	0.1	0.1	0.1
Absence of Ring	8.1	6.5	8.4	16.5	20.8	10.3	2.8	2.0	1.5	0.7	0.5	0.9
Scalar vs. Vector	13.1	13.7	17.6	15.4	10.3	3.0	2.1	1.0	0.6	0.2	0.1	0.2
Residual after correction	2.0	2.2	2.7	2.2	1.4	0.4	0.5	0.3	0.3	0.1	0.0	0.1

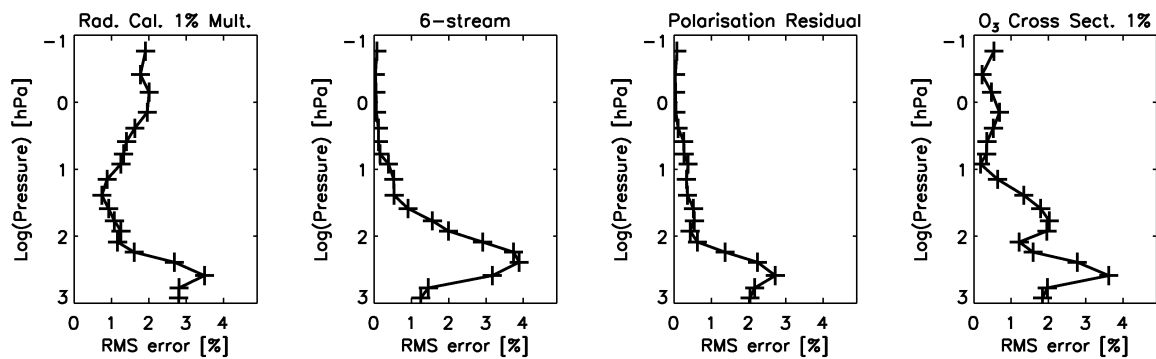


Figure 4.4 Main error contributions to the total ozone profile error; multiplicative error in the radiance (1%), 6-stream radiative transfer error, the residual error after using the polarisation look-up table and the error in the ozone cross section.

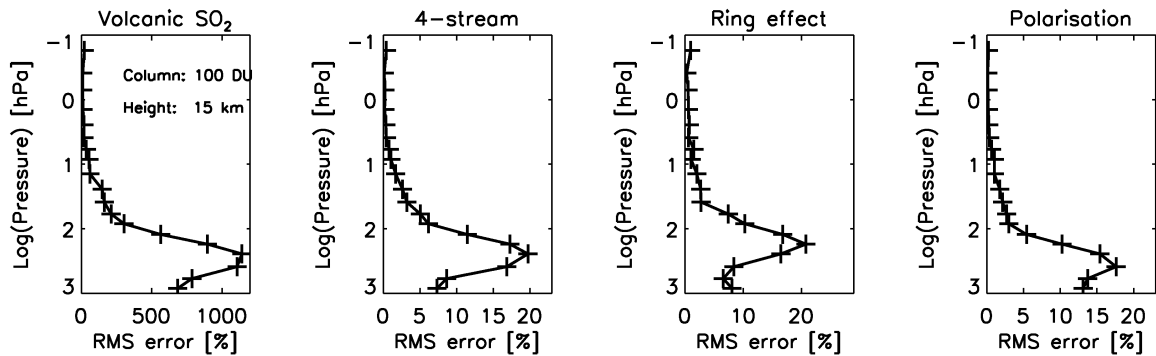


Figure 4.5 Errors on the retrieved ozone profile which do not contribute to the total error budget. In case of a volcanic eruption, the level 2 data will be flagged. The other three error sources are shown here to justify our choice of using 6-stream in the radiative transfer model, to include a Ring spectrum in the fitting and to use a look-up table for the polarisation error in the radiative transfer.

4.6. Discussion

In Table 4.7, the RMS errors of all errors that contribute to the accuracy of the retrieved profile are shown; with and without the smoothing error. The table also includes the accuracy requirements from the SRD [Levelt *et al.*, 2000]. We conclude that these requirements are met for all but two layers, for this specific choice of error sources, in case the smoothing error is included. For the 70-100 mbar layer and the top layer, the required accuracy is not met. Without the smoothing error all requirements are met. Note that a dominant error contribution comes from the multiplicative radiance measurement errors. Our assumptions on their magnitudes may turn out to be inaccurate after launch. Another dominant source is the uncertainty in the ozone cross sections.

Table 4.7 Total RMS error (with and without the smoothing error) of all applicable errors, compared with the values in the OMI Science Requirements Document.

	1000- 700	700- 500	500- 300	300- 200	200- 150	100- 70	50- 30	20- 10	7- 5	3- 2	1- 0.5	0.3- 0.0
A priori error	27.8	22.5	38.1	46.0	45.8	26.5	12.7	12.3	14.2	13.4	12.7	24.8
Total error	7.4	7.6	12.3	11.7	10.0	5.6	3.1	1.9	2.0	2.6	5.2	8.1
Total error, including smoothing error	26.5	20.0	28.9	26.8	24.8	12.6	5.2	2.7	3.4	3.6	7.0	16.9
SRD requirements	30.0	30.0	30.0	30.0	30.0	10.0	10.0	10.0	10.0	10.0	10.0	10.0

The smoothing error is relevant when one ignores the information contained in the averaging kernels. Using the averaging kernels gives the reward of smaller profile errors. This is especially relevant for the use of the profile in assimilation.

In this document, we present result of the error analysis for an upper wavelength of 330 nm. We have performed the same analyses using upper wavelengths of 320 and 340 nm, respectively. The results show that the errors due to 4- and 6-stream, aerosols and clouds, increase with increasing wavelength. We conclude that an upper wavelength of 330 nm provides the best trade-off between information content (see Section 4.4.4) and error reduction.

The vertical resolution of the retrieved ozone profile of 5 and 10 km, in stratosphere and troposphere respectively, as stated in the SRD is somewhat smaller than the widths of the averaging kernels in Figure 4.3 (using the US96 standard atmosphere to relate pressure to altitude). More realistic values for the resolution are 15 km in the troposphere and 7 km in the stratosphere, below 2 hPa.

4.7. Validation

The first phase of algorithm validation concerns algorithm verification. For this, the algorithm is provided with synthetic test data sets computed with the forward model as used in the algorithm; with full control over the Level 1 input, it is then possible to test all error effects separately. The OMI instrument model provides measurement error, which should be as realistic as possible. Results from the error analysis are summarized in the previous section for a wide range of scenarios applicable to OMI. This phase can also be extended by using synthetic data constructed from a different (but also state-of-the-art) RTM, and performing end-to-end tests on the retrieval.

The second phase involves a test data set provided the OMI US team leader; this set will cover several orbits of OMI data. This phase involves end-to-end testing, and the requirements stated in the SRD will be checked using results from these retrievals. This is a good test for the robustness of the algorithm.

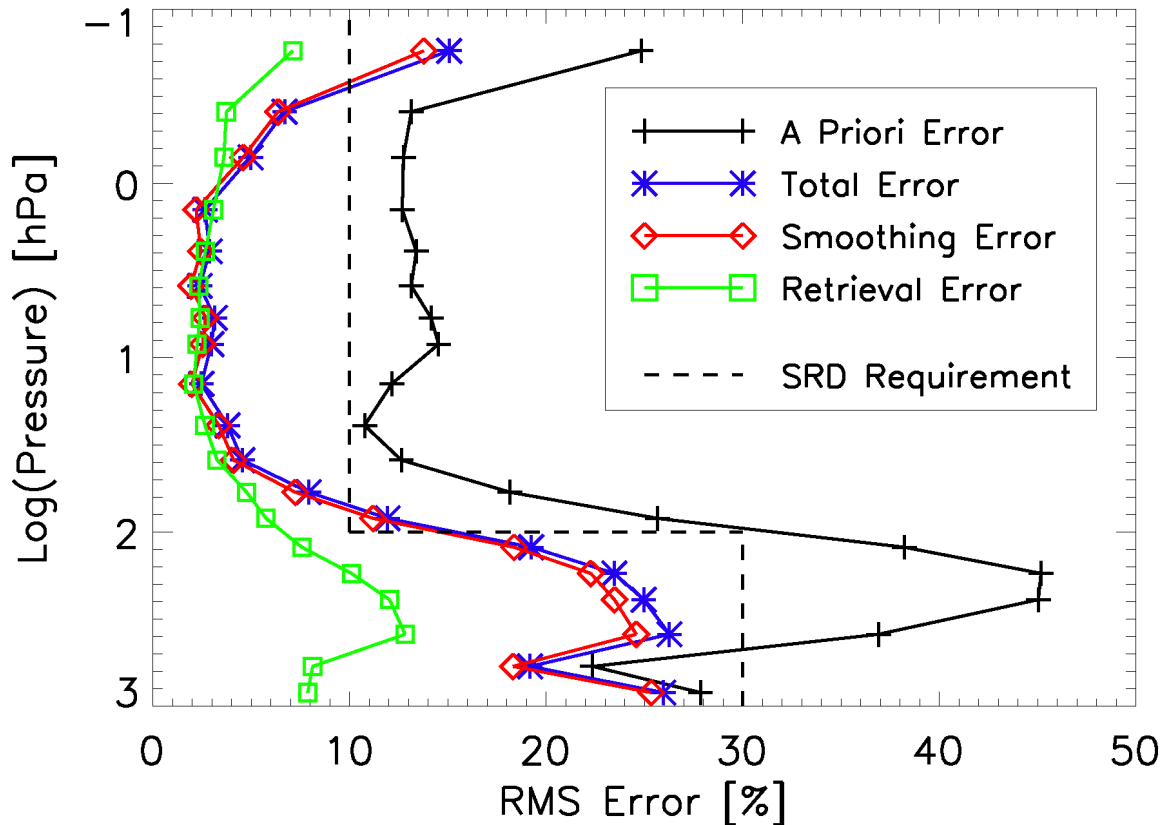


Figure 4.6 Summary of relevant errors for the ozone profile retrieval. The retrieval leads to an error reduction from a priori values (black line) to posterior values (Total error: blue line). The total error comprises the smoothing error (red line) and the error resulting from the presented error analysis (green). The dashed line represents the requirements as stated in the SRD (Level et al., 2000).

The third phase is properly called product verification and starts during the post-launch commissioning phase after the initial checkout of the instrument has been completed. Real OMI data are used and the level 2 ozone profile products compared with external data provided as part of a dedicated validation program for the OMI products. Other groups not directly involved in the algorithm development will perform this validation. This exercise lasts for the duration of commissioning phase, and will involve detailed comparisons for several months of OMI data. Long-term external validation will continue during the remainder of the instrument's lifetime.

Acknowledgement: We would like to thank Johan de Haan for his critical reading of the document and for invaluable suggestions for improvements.

4.8. References

- Anderson, G.P., S.A. Clough, F.X. Kneizys, J.H. Chetwynd, E.P. Shettle, *AFGL atmospheric constituent profiles*, 1986, in: Environmental research papers, no. 954, Air Force Geophysical Laboratory, AFGL-TR-86-0110
- Anderson, E., Z. Bai, C. Bischof et al., "*LAPACK User's Guide*", Society for Industrial and Applied Mathematics, Philadelphia, 2nd edition, 1995
- Bass, A.M., R.J. Paur, "*The UV cross-sections of ozone: 1. Measurements in atmospheric ozone.*", 1985, in: Proceedings of the quadrennial ozone symposium, p.606-616.
- Bates, D.R., "*Rayleigh scattering by air*", Planet. Space Sci. 32, 785-790, 1984
- Berk, A., L. S. Bernstein, D. C. Robertson, "*MODTRAN: A moderate resolution model for LOWTRAN-7*", GL-TR-89-0122, Geophysics Laboratory, Hanscom AFB, MA 01732, 1989.
- Bhartia, P.K., R.D. McPeters, C.L. Mateer, L.E. Flynn, C. Wellemeyer, "*Algorithm for the estimation of vertical ozone profiles from the backscattered ultraviolet technique*", J. Geophys. Res 101, 18793-18806, 1996
- Burrows, J.P. et al. "*The Global Ozone Monitoring Experiment (GOME): mission concept and first scientific results*", J. Atmos. Sci. 56, 151-175, 1999
- Chance, K.V., R.J.D. Spurr, "*Ring effect studies: Rayleigh scattering, including molecular parameters for rotational Raman scattering and the Fraunhofer spectrum*", Applied Optics 36, 5224-5230, 1997
- Chance, K.V., J. P. Burrows, D. Perner, W. Schneider, "*Satellite measurements of atmospheric ozone profiles, including tropospheric ozone, from ultraviolet/visible measurements in the nadir geometry: a potential method to retrieve tropospheric ozone*", J. Quant. Spectrosc. Radiat. Transfer 57, 467-476, 1997
- Chance, K.V., Wavelength calibration corrected Bass & Paur Ozone cross sections, private communication, 2001
- Chandrasekhar, S., "*Radiative Transfer*", Dover, New York, 1960
- Caudill, T.R., D.E. Flittner, B.M. Herman, O. Torres, R.D. McPeters, "*Evaluation of the pseudo-spherical approximation for backscattered ultraviolet radiances and ozone retrieval*", J. Geophys. Res. 102, 3881-3890, 1997
- De Haan, J., P. Bosma, J. Hovenier, "*The adding method for multiple scattering calculations of polarized light*", Astron. Astrophys. 181, 371-391, 1987
- Fokker Space, "*DM Performance Test Results Analyses Report*", RP-OMIE-0000-FS-351, 2000
- Fortuin, J.P.F., U. Langematz, "*An update on the global ozone climatology and on concurrent ozone and temperature trends*", in Atmospheric Sensing and Modelling, ed. R.P. Santer, Proc. SPIE 2311, 207-216, 1995
- Fortuin, J.P.F., H. Kelder, "*An ozone climatology based on ozonsonde and satellite measurements*", J. Geophys. Res 103, 31709-31734, 1999
- Grainger, J.F., J. Ring, "*Anomalous Fraunhofer line profiles*", Nature 193, 762, 1962
- Hasekamp, O., J. Landgraf, "*Ozone profile retrieval from backscattered ultraviolet radiances: The inverse problem solved by regularization*", J. Geophys. Res, in press, 2001
- Herman, J.R., E.A. Celarier, "*Earth surface reflectivity climatology at 340-380 nm from TOMS data*", J. Geophys. Res 102, 28003-28011, 1997
- Hoogen, R., V.V. Rozanov, J.P. Burrows, "*Ozone profiles from GOME satellite data: Algorithm description and first validation*", J. Geophys. Res. 104, 8263-8280, 1999.

- Joiner, J., P.K. Bhartia, R.P. Cebula, E. Hilsenrath, R.D. McPeters, H. Park, “*Rotational Raman scattering (Ring effect) in satellite backscatter ultraviolet measurements*”, *Applied Optics* 34, 4513-4525, 1995.
- Lacis, A.A., J. Crowdry, M. I. Mischenko, B. Cairns, “*Modeling errors in diffuse sky radiation: Vector vs. scalar treatment*”, *Geophys. Res. Lett.* 25, 135-138, 1998
- Landgraf, J., O. Hasekamp, M. Box, T. Trautmann, “*A Linearized Radiative Transfer Model for Ozone Profile Retrieval Using the Analytical Forward-Adjoint Perturbation Theory Approach*”, in preparation, 2001
- Levelt, P.F. et al., “*Science Requirements Document for OMI-EOS*”, RS-OMIE-KNMI-001, Version 2, 2000
- McPeters, R. D., The behavior of ozone near the stratopause from 2 years of BUV observations, *J. Geophys. Res.*, 85, 4545-4550, 1980.
- Mischenko, M.I., A. A. Lacis, L. D. Travis, “*Errors induced by the neglect of polarization in radiance calculations for Rayleigh-scattering atmospheres*”, *J. Quant. Spectrosc. Radiat. Transfer* 51, 491-510, 1994
- Munro, R., Siddans, R., Reburn, W.J., Kerridge, B.J., “*Direct measurement of tropospheric ozone distributions from space*”, *Nature* 392, 168-171, 1998
- Nakajima, T., M. Tanaka, “*Algorithms for radiative intensity calculations in moderately thick atmospheres using a truncation approximation*”, *J. Quant. Spectrosc. Radiat. Transfer* 40, 51-69, 1988
- Orphal, J., “*A Critical Review of the Absorption Cross-sections of O₃ and NO₂ in the 240-790 nm Region. Part 1. Ozone.*” Draft Version March 29, 2001. Prepared for ESA-ESTEC.
- Rawcliffe, R.D., and D. D. Elliott, Latitude distribution of ozone at high altitudes, deduced from a satellite measurement of the Earth’s radiance at 2840Å, *J. Geophys. Res.*, 71, 5077-5089, 1966.
- Rodgers, C.D., “*Retrieval of atmospheric temperature and composition from remote measurements of thermal radiation.*”, *Rev. Geoph. Sp. Phys.* 14, 609-624, 1976
- Rodgers, C.D., “*Characterisation and error analysis of profiles retrieved from remote sounding experiments.*”, *J. Geophys. Res* 95, 5587-5595, 1990
- Rodgers, C.D., “*Inverse methods for atmospheric sounding*”, World Scientific Publishing Pte Ltd, New York, 2000
- Rothman, L.S., et al., “*The HITRAN molecular database: Editions of 1991 and 1992*”, *J. Quant. Spectrosc. Radiat. Transfer* 48, 469-507, 1992
- Roazanov, V.V., T. Kurosu, J.P. Burrows, “*Retrieval of atmospheric constituents in the UV-visible: A new quasi-analytical approach for the calculation of weighting functions*”, *J. Quant. Spectrosc. Radiat. Transfer* 60, 277-299, 1998
- Roazanov, A.V., V.V. Roazanov, J.P. Burrows, “*Combined differential-integral approach for the radiation field computation in a spherical shell atmosphere: Nonlimb geometry*”, *J. Geophys. Res.* 105, 22937-22942, 2000
- Singer, S.F., R.C. Wentworth, “*A method for the determination of the vertical ozone distribution from a satellite*”, *J. Geophys. Res.* 62, 299-2308, 1957
- Spurr, R.J.D., *Linearized Radiative Transfer Theory*, Proefschrift Technische Universiteit Eindhoven, 2001
- Spurr, R.J.D., T.P. Kurosu, K.V. Chance, A linearised discrete ordinate radiative transfer model for atmospheric remote sensing retrieval, *J. Quant. Spectrosc. Radiat. Transfer* 68, 689-735, 2001
- Spurr, R.J.D. “*Simultaneous radiative transfer derivation of intensities and weighting functions in a general pseudo-spherical treatment*”, *J. Quant. Spectrosc. Radiat. Transfer*, in press, 2001

- Stammes, P., “*Errors in UV reflectivity and albedo calculations due to neglecting polarisation*”, Proc. of SPIE, Atmospheric Sensing and Modelling, Vol. 2311, p.227-235, 1994
- Stammes, K, S.-C. Tsay, W. Wiscombe, K. Jayaweera, “*Numerically stable algorithm for discrete-ordinate-method radiative transfer in multiple scattering and emitting layered media*”, Applied Optics 27, 2502-2509, 1988
- Thomas, R. W. L., and A. C. Holland, Simple relationship between the UV radiation backscattered by the earth’s atmosphere and the vertical ozone profile, *Appl. Opt.*, 16, 2581-2583, 1977.
- Timmermans, R., 2000, *private communication*
- Twomey, S., “*On the deduction of the vertical distribution of ozone by ultraviolet spectral measurements from a satellite*”, J. Geophys. Res. 66, 2153-2162, 1961
- Vandaele, A.C., C. Hermans, P.C. Simon et al., “*Measurements of the NO₂ absorption cross-sections from 42,000 cm⁻¹ to 10,000 cm⁻¹ (238-1000nm) at 220K and 294K*”, J. Quant. Spectrosc. Radiat. Transfer 59, 171-184, 1998
- van der A, R., R.F. van Oss, H. Kelder, “*Ozone profile retrieval from GOME data*”, in Satellite Remote Sensing of Clouds and the Atmosphere III, Jaqueline E. Russel, Editor, Proceedings of SPIE Vol. 3495, 221-229, 1998
- van Oss, R., R.J.D.Spurr, “*Sensitivity and error assessment of operational ozone profile retrieval algorithms for the GOME and GOME-2 remote sensing spectrometers*”, in preparation, 2001a
- van Oss, R., R.J.D.Spurr, “*Fast and accurate 4 and 6 stream linearised discrete ordinate radiative transfer models for ozone profile remote sensing retrieval*”, J. Quant. Spectrosc. Radiat. Transfer, in press, 2001b
- Vountas, M., V.V. Rozanov, J.P. Burrows, “*Ring effect: impact of rotational Raman scattering on radiative transfer in Earth’s atmosphere*”, J. Quant. Spectrosc. Radiat. Transfer 60, 63-77, 1998
- Wiscombe, W.J., “*The delta-M method: rapid yet accurate radiative flux calculations for strongly asymmetric phase functions*”, J. Atmos. Sci. 34, 1408-1422, 1977

5. Tropospheric O₃ Residual

Jack Fishman, NASA Langley Research Center, Hampton, Virginia, USA
Sushil Chandra, NASA Goddard Space Flight Center, Greenbelt, Maryland, USA
Jerald Ziemke, SGT, Greenbelt, Maryland, USA

5.1. Overview

Over the past decade, several research groups have focused on methods to extract information about the troposphere from satellite measurements. Tropospheric information from total ozone measurements is obtainable if the assumption is valid that stratospheric ozone variability occurs on relatively large spatial scales whereas tropospheric variability takes place on smaller scales [Fishman et al., 1990; Ziemke et al., 1998, Hudson and Thomson 1998]. Once the quasi-static stratospheric ozone distribution had been established in each of the above studies, TOMS (Total Ozone Mapping Spectrometer) total ozone measurements were used to infer information about the troposphere. The resultant distribution derived from this method has been referred to as the “tropospheric ozone residual” (TOR).

When Aura is launched, HIRDLS, MLS, and OMI will be capable of providing information about the distribution of stratospheric ozone. HIRDLS will provide daily stratospheric ozone distributions with a horizontal resolution of ~400 km x 500 km and will be the instrument from which we will initially determine the stratospheric ozone distribution. Using these data in conjunction with the daily analysis of tropopause height, integrated stratospheric ozone columns can be constructed. These fields are then subtracted from the total ozone distributions generated from OMI measurements to determine the daily distribution of the TOR.

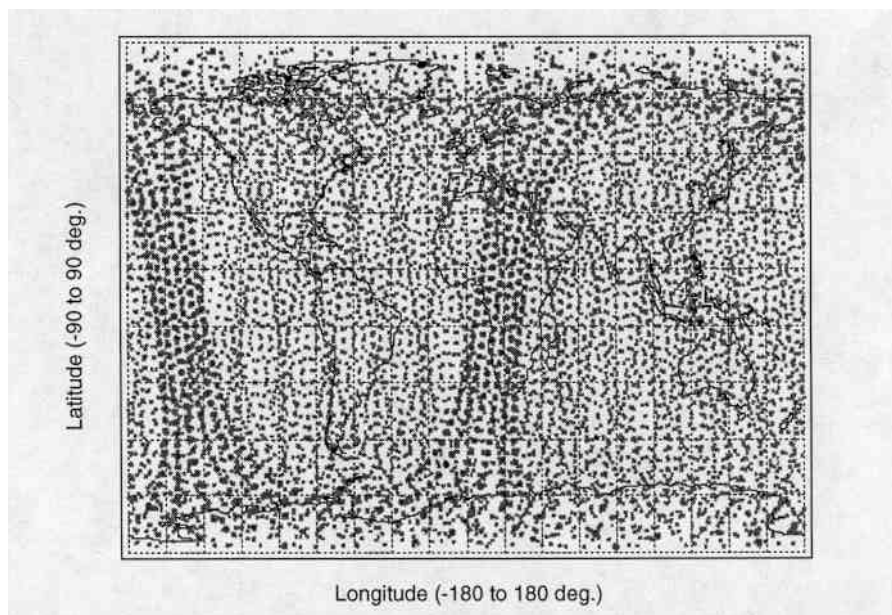


Fig 5-1: Distribution of HIRDLS profiles for a typical day

5.2. Proposed TOR Algorithm Using Data from OMI and HIRDLS

To apply the TOR method of Fishman et al. [1990], ozone vertical profiles from HIRDLS will be used. A typical day coverage from HIRDLS is shown in Figure 5-1. In addition, a daily global data set of tropopause height, which will be obtained from the meteorological analyses of the Goddard Data Assimilation Office (DAO). Currently, this data product is produced on a 1° by 1° grid, but should be available with a resolution of 0.5° by 0.5° resolution by the time Aura is launched.

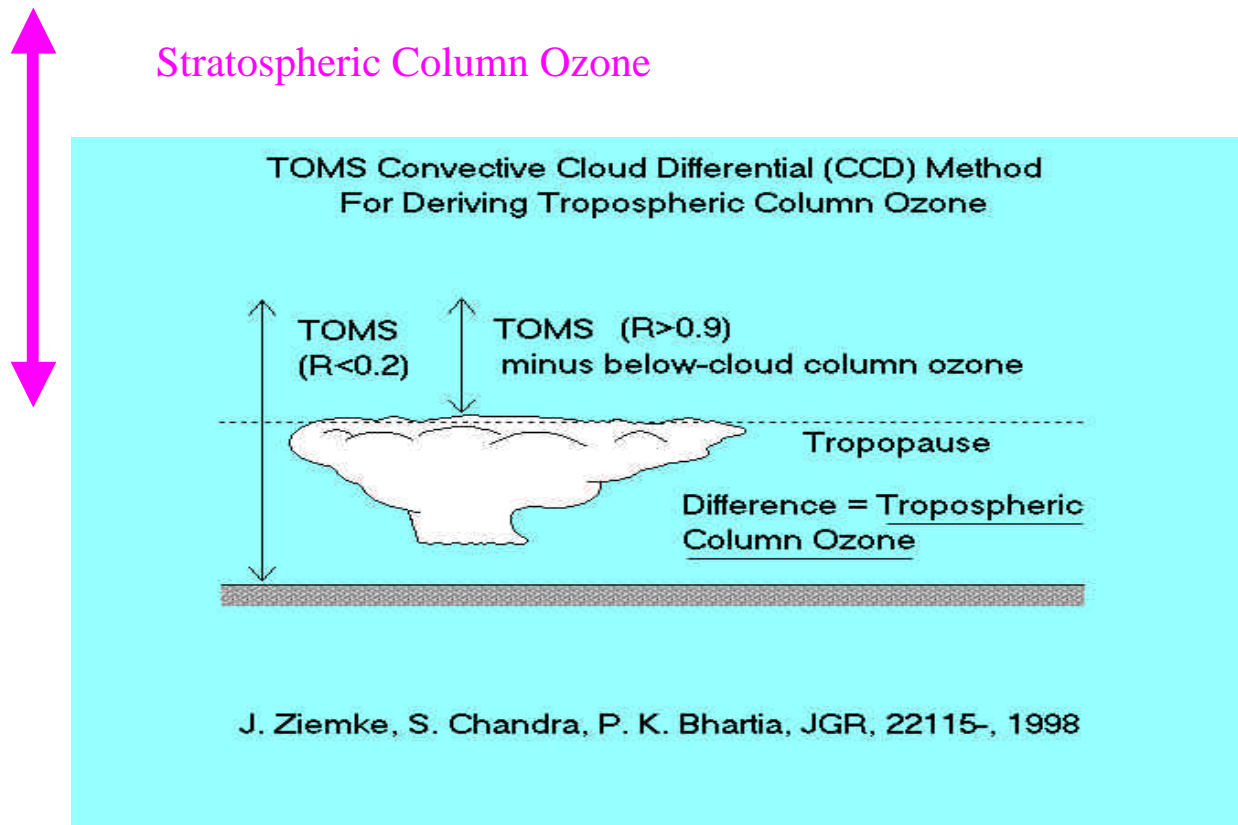


Figure 5-2 Schematic showing how stratospheric ozone amount is determined from OMI data using the Convective Cloud Differential technique.

Application of the TOR algorithm must consider the fact these data sets have very different vertical and horizontal resolution and sampling. OMI horizontal resolution varies from 13 km x 24 km at nadir to about ~100 km at the extreme off-nadir for total ozone. The averaging volume for HIRDLS for each data sample is 1-km vertical x 10 km across x 300 km along line-of-site. The integration of ozone above the tropopause is straightforward as long as the spatial gradient of the height of the tropopause is not varying significantly. In regions of high temporal variability of the height and position of the tropopause, (e.g., in regions near the existence or the development of a tropopause fold) the TOR methodology cannot be applied.

To ensure consistency between ozone derived from HIRDLS and OMI, the amount of ozone in the stratosphere (stratospheric column ozone or SCO) will be calculated using the convective cloud differential (CCD) technique shown in Figure 5-2 [Ziemke et al., 1998]. In this technique the stratospheric ozone column can be estimated by retrieving the amount of column ozone above locations where convective clouds are present. At these locations, the amount of stratospheric ozone derived from HIRDLS will also be calculated to derive the ratio between the

SCO calculated using the two values. Figure 5-3 illustrates the relationship between the SCO values derived using the CCD technique applied to existing TOMS data and SCO amounts determined from other existing instruments: HALOE and MLS. As can be seen from this figure, the three data sets track each other very well on a monthly basis, but there is a relatively constant offset in the average amounts using the two methods.

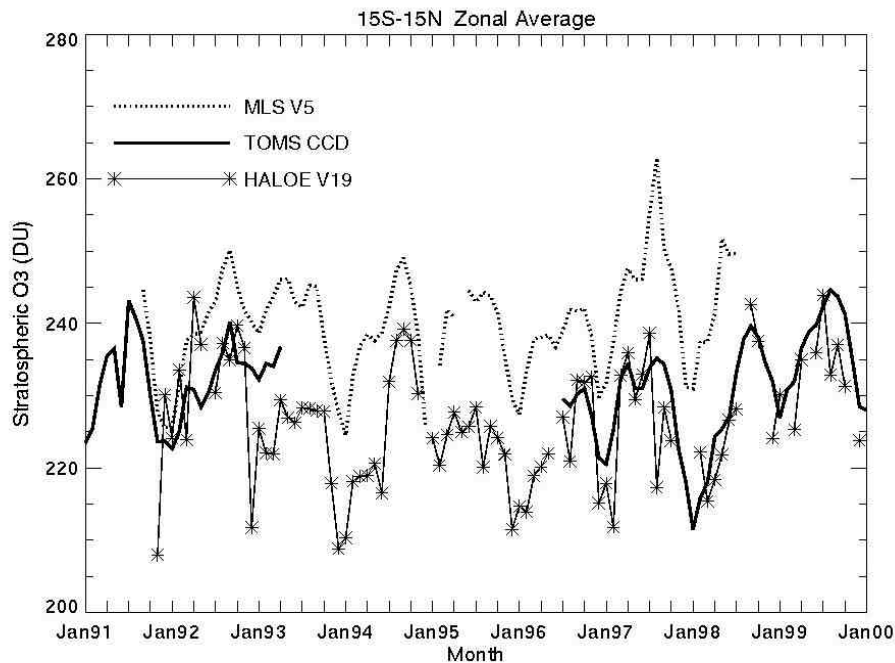


Figure 5-3: Relationship between SCO derived from TOMS using CCD technique and SCO derived from MLS and HALOE vertical profiles.

Once the SCO field is calculated from the HIRDLS measurements, all values will be normalized using the ratio calculated from the direct comparison with the SCO values generated from the CCD technique using OMI data. These normalized values will then be subtracted from the total ozone fields determined from the OMI measurements. An analogous method using TOMS and MLS data is depicted in Figure 5.4. These values, indicated by the thick solid lines in each of the four panels, is compared with tropospheric column ozone amounts derived from ozonesonde measurements at four stations.

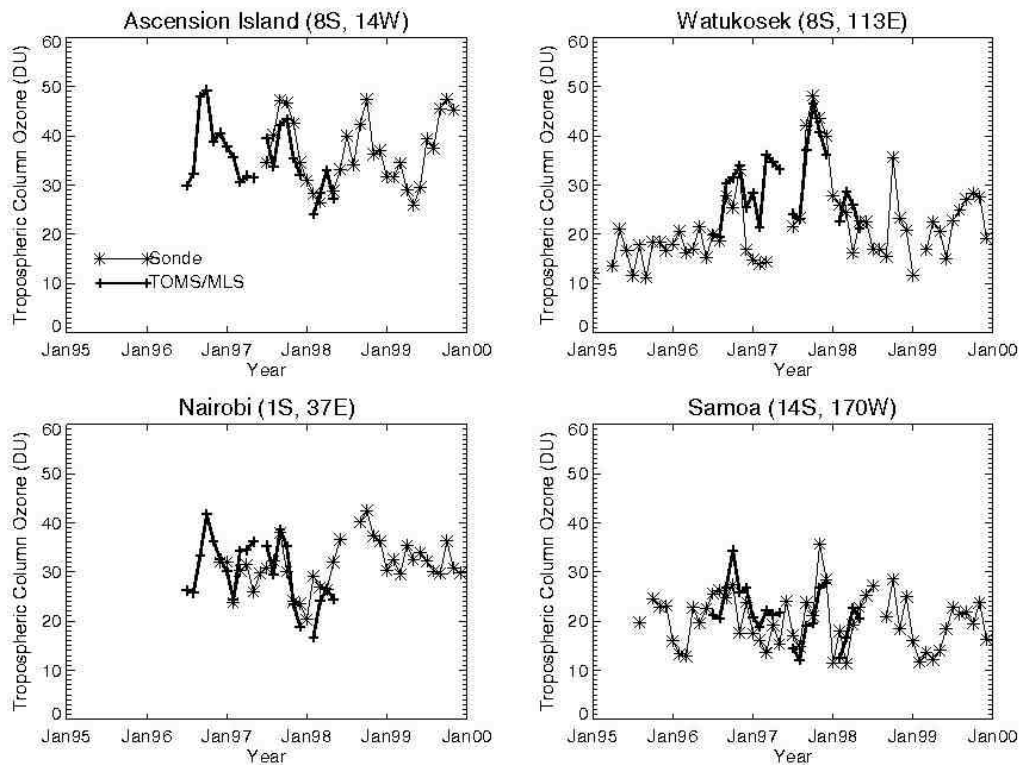


Figure 5-4 Comparison of corrected TCO data from TOMS/MLS with ozonesonde measurements at selected stations.

Whereas the four stations depicted in Figure 5.4 are located in the tropics, where the CCD values from TOMS are calculated, Figure 5.5 shows the comparison of this method at middle latitudes. The favorable agreement indicates that the method can be extrapolated to higher latitudes. The data in this figure using the same method of calculation, however, have been influenced by information in the lower stratosphere—a common problem in the interpretation of such measurements to a fixed pressure height. When the height of the tropopause is below the fixed pressure, amounts are strongly influenced by the relatively few times when lower stratospheric ozone is included in the tropospheric amount. With the greater vertical resolution in the vicinity of the tropopause using HIRDLS, we anticipate better measurements down to the true height of the tropopause.

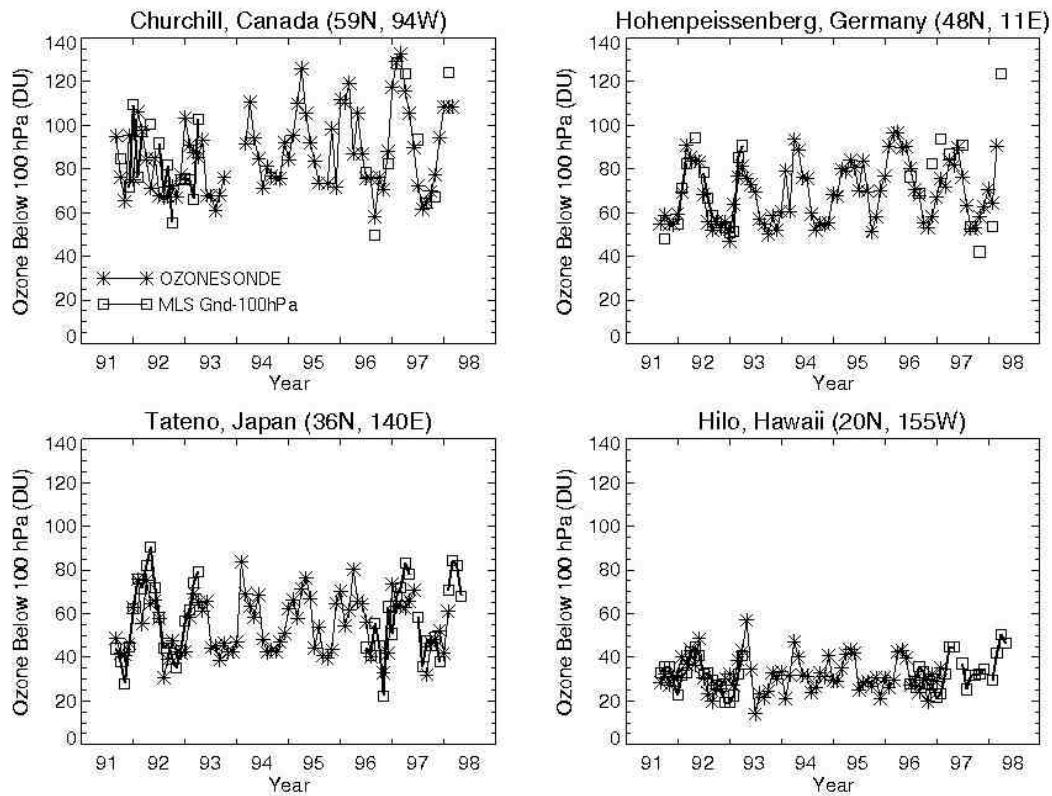


Figure 5-5 Comparison of corrected TCO data from TOMS/MLS with ozonesonde measurements at selected stations.

A regional depiction (Equator to 50°N; 90°E to 180°W) of the TOR for a specific day is illustrated in Figure 5-6. Superimposed on the color-contoured TOR distribution is the distribution of tropopause height plotted in hPa. For illustrative purposes, the 200-hPa line is shown as thick white line. This depiction uses TOMS and SBUV measurements employing the empirical correction described in Fishman and Balok [1999]. As can be seen from this figure, the tropopause height gradient shows relatively little variability south of ~35°N. In the preparation of the daily TOR values envisaged to be produced using OMI and HIRDLS measurements, we anticipate calculating these fields only in regions where the tropopause height determination can be done without ambiguity.

5.3. Error Analysis

The accuracy of the tropospheric ozone column derived from the methods described above is dependent on a number of factors, which depend on the potential errors from a number of other instruments and data products. For the residual techniques, the errors can be broken down into four components: error in the total ozone column amount derived from OMI; error in the derivation of the SCO measurements from other instruments, error in interpolation of SCO to the OMI pixel, and error in tropopause height. We discuss these errors below.

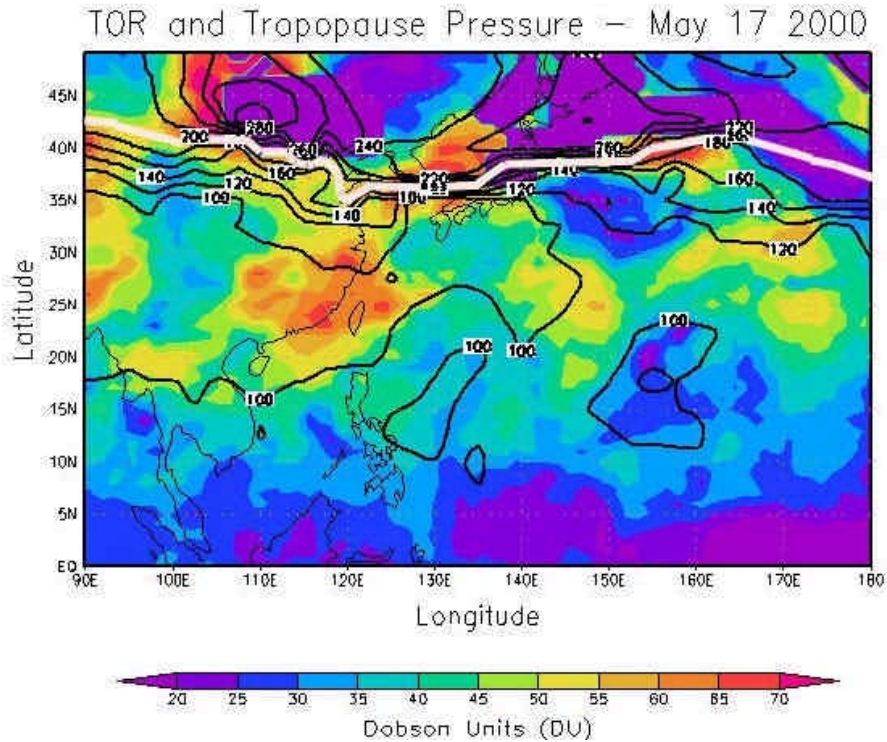


Figure 5-6: Distribution of Tropospheric Ozone Residual and tropopause height pressure calculated for a specific day over the western Pacific Ocean.

5.3.1. OMI Total O₃ Error

As discussed in Chapter 2, at low to moderate solar zenith angles ($<75^\circ$), the principle error source in OMI total ozone algorithm comes from the fact that the UV radiation received by OMI loses sensitivity to tropospheric ozone (due to Rayleigh scattering and clouds). Therefore, high tropospheric ozone causes total ozone to be underestimated and vice versa. Using ozonesonde profiles, the estimated rms error in OMI total ozone retrieval at solar zenith angles less than 75° is $\sim 1\%$, which will lead to about 10% rms error in tropospheric ozone. However, since this error is roughly anti-correlated with tropospheric ozone column, it would lead to underestimation of tropospheric ozone variation. One can apply an efficiency correction [Ziemke et al., 2001] assuming that lower tropospheric ozone is correlated with the total tropospheric column, however, this may lead to some overestimation of tropospheric O₃ variation.

5.3.2. Error in Stratospheric Column Ozone (SCO)

The accuracy of the stratospheric column amounts derived from MLS and HIRDLS is not known at this time. Currently, one of the greatest unknowns is the effect of inhomogeneity in the ozone profile along the line-of-sight (LOS) on the limb profilers. These effects get worse as one goes below the ozone density peak, where the ozone mixing ratio drops very rapidly with altitude. In this region, inhomogeneity at a given altitude can introduce spurious or “ghost” signals at a lower altitude. The MLS algorithm team has determined that these problems can be significantly reduced by taking advantage of the fact that the MLS measurements along the LOS are nearly contiguous. (MLS LOS coincides with the Aura satellite’s orbital track). The MLS team plans to retrieve blocks of up to 100 profiles at one time, so inhomogeneity effects are directly built into the retrieval algorithm. However, HIRDLS sampling is not optimum to apply similar type of correction. Given the complexity in modeling these effects, the magnitude of the errors will only be apparent after direct comparison of HIRDLS and MLS profiles with ground-truth. In principle, high horizontal resolution OMI profiles, despite their low vertical resolution, could be useful for assessing and correcting the inhomogeneity errors in MLS and HIRDLS, and in extreme cases flagging the data as unreliable.

Finally, it should be noted that owing to its higher vertical resolution HIRDLS should detect the tropopause better than MLS; on the other hand, MLS is not affected by aerosols and is far less sensitive to clouds than HIRDLS, so it is likely to be more reliable near the tropopause.

5.3.3. Interpolation Errors

Based on our experience in deriving tropospheric ozone using SAGE and other low sampling instruments, we expect that HIRDLS and MLS sampling would not be a significant error source in the tropics, or in the subtropics. However, at higher latitudes when planetary wave activity is strong interpolation errors are likely to be significant and any product derived during such synoptic situations would be flagged. Some of this error can be reduced by using the OMI profiles, as discussed in section 5.2. Later versions of the algorithm may use more sophisticated interpolation schemes, such as Bayesian maximum entropy (BME) spatiotemporal interpolation [e.g., Christakos, 1998; Christakos and Vyas, 1998] instead of the methods that have been employed in Fishman and Balok [1999]. Preliminary results using SBUV observations to derive global total ozone fields by incorporating a knowledge of 200-hPa geopotential height distribution have shown encouraging promise in the reconstruction of total ozone maps and then compared with those derived from TOMS [Christakos, unpublished data, 2001]. This method will be explored using simulated MLS ozone profiles in conjunction with DAO tropopause height analyses to provide an improved SCO data product to be used in conjunction with total ozone fields from OMI to produce TOR fields in the middle latitudes.

5.3.4. Error in Tropopause Height

Finally, we have to consider inaccuracy in determining the height of the tropopause. The tropopause height information will be obtained through GSFC’s DAO. The accuracy of this product has never been examined, but in regions where the height of the tropopause should remain fairly constant over a several-day period, the inaccuracy of this product should not contribute errors of more than 1-3 DU since ozone number densities are usually very low in the upper troposphere. In regions where the tropopause is highly variable (normally in regions of a strong jet stream and changing synoptic conditions), the TOR cannot be computed with a high degree of confidence and such points would be flagged [e.g., see discussion in Fishman et al., 1996a].

5.4. Validation

5.4.1. Comparison with Ozonesondes

We anticipate that there will be a validation plan using existing ozonesonde sites to compare the ozone measurements with ozone measurements derived from satellite overpasses. The sonde data employed for this task will include tropospheric ozone profile measurements from the World Ozone and Ultraviolet Radiation Data Centre (WOUDC) and Southern Hemisphere Additional Ozonesondes (SHADOZ). Measurements from SHADOZ are tropical while measurements from WOUDC are primarily extratropical.

5.4.2. Coordinated Aircraft Campaigns

Using an airborne UV-DIAL system [e.g., see Browell et al., 1996], horizontal gradients of tropospheric column ozone can be obtained over domains of several thousands of kilometers over a typical flight day. Figure 5-7 shows a comparison of the integrated ozone obtained from such a system during a transit flight from Puerto Rico to California during the TRACE-A (Transport and Atmospheric Chemistry near the Equator—Atlantic) field mission in 1992 [Fishman et al., 1996b]. The regional TOR distribution using the technique described in Fishman et al. [2001] is shown in the top panel with the flight path of the NASA DC-8 aircraft depicted by the black dots, where the DC-8's position is marked every 15 minutes, a distance of ~200 km. As the plane flies at an altitude of 9.5-11.5 km during this transit, the UV-DIAL system is capable of obtaining vertical profiles with a vertical resolution of 300 m below the aircraft and 450 m above the aircraft at an accuracy of better than 5% when the profiles are averaged over a 5-minute period (~70 km horizontal resolution). From knowledge of the tropopause height along the flight path readily determinable from the zenith lidar data, the profiles can be integrated throughout the troposphere to produce a tropospheric ozone column amount. At flight level, in situ ozone concentrations are used [Gregory et al., 1996] and extrapolated to fill in the profile near the airplane where the differential lidar technique does not provide usable information [Browell et al. 1996].

The bottom panel compares the tropospheric column amounts from the UV-DIAL measurements with the TOR values shown in the top panel. From this comparison, it can be seen that certain components of the UV-DIAL data agree very well and that nearly all the UV-DIAL and TOR measurements agree to within 10 DU of each other. In addition, both data sets show equivalently low values over San Juan and over the California coast. Both data sets also show an ozone maximum over the Gulf of Mexico. The TOR distribution indicates another broad region of higher ozone over Arkansas and northern Texas that the DC-8 clips en route, but only slightly elevated ozone amounts are indicated by the DC-8 measurements.

Although these types of validation flights are perhaps the most useful for obtaining ground truth, it also has to be noted that they cannot be exactly coincident in time. Whereas the DC-8 measurements required 7.5 hours, most of the data from which the TOR were computed could have been obtained from two orbits, separated by ~90 minutes. Furthermore, the spatial resolution of the tropopause height data used in these calculations was obtained from an analysis with ~250 km resolution and the data were linearly interpolated between two sets of measurements separated by 12 hours. All of these factors decrease the absolute accuracy of a direct comparison, but can be improved through the use of data assimilation. Improvements using the Goddard Data Assimilation Office to derive time-varying tropopause height fields will be explored before the launch of OMI.

Tropospheric Ozone Residual
 Latitude: 10N to 40N
 October 26, 1992 (TRACE-A Flight No. 19) Longitude: 125W to 65W

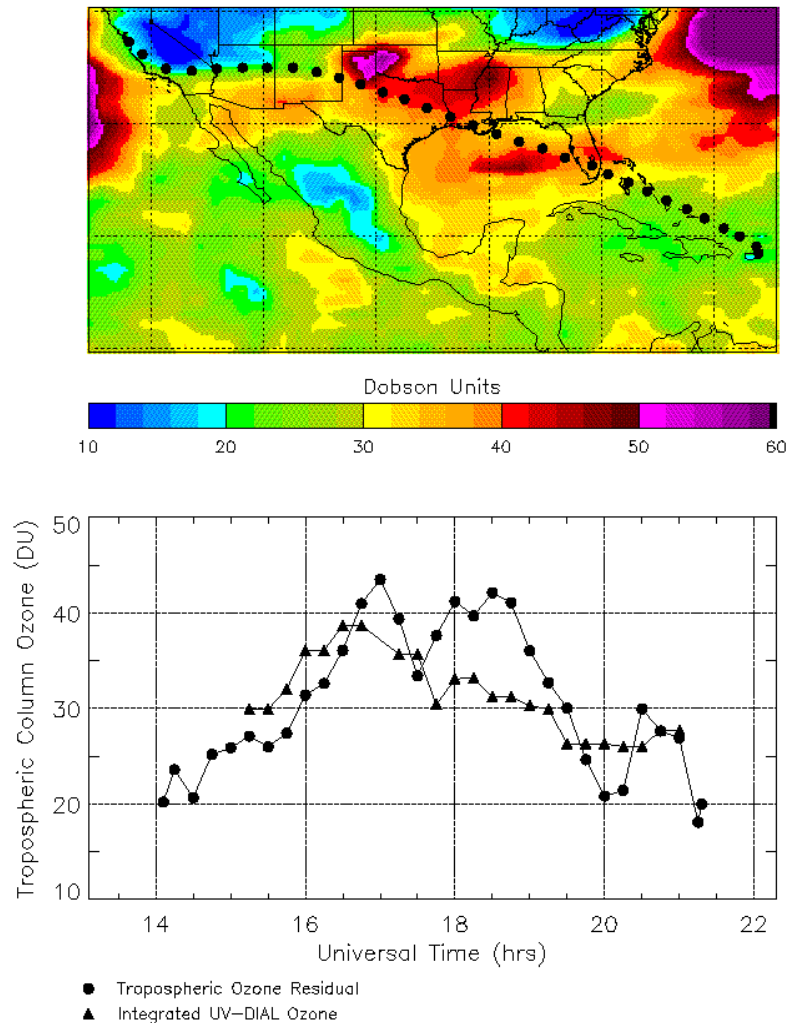


Figure 5-7: Comparison of TOR fields derived from the empirically corrected TOMS/SBUV residual method with tropospheric ozone columns derived from UV-DIAL measurements during a flight from San Juan, Puerto Rico (take-off ~1400 UT) to Moffett Field, CA (landing ~2130 UT), on October 26, 1992. Top panel shows the flight path superimposed on the TOR field; bottom panel compares the two methods at the points shown in the top panel. DIAL measurements are averaged over 15-minute flight segments.

5.4.3. Comparison with TES

An independent measurement of tropospheric ozone will also be available from TES. As data become available from both instruments, comparisons will be made and the conditions where the values differ will be studied. We will be in contact with the TES Science Team and coordinate any validation plans they have so that the two groups do not duplicate efforts or waste any resources required for validation/calibration studies.

5.5. References

- Browell, E.V., et al., Ozone and aerosol distributions and air mass characteristics over the South Atlantic Basin during the burning season, *J. Geophys. Res.*, **101**, 24,043-24,068, 1996.
- Chandra, S., J. R. Ziemke, W. Min, and W. G. Read, Effects of 1997-1998 El Niño on tropospheric ozone and water vapor, *Geophys. Res. Lett.*, **25**, 3867-3870, 1998.
- Christakos, G., Spatiotemporal information systems in soil and environmental sciences, *Geoderma*, **85**, 141-179, 1998.
- Christakos, G., and V.M. Vyas, A composite space/time approach to studying ozone distribution over eastern United States, *Atmos. Env.*, **32**, 2845-2857, 1998.
- Fishman, J., and A.E. Balok, Calculation of daily tropospheric ozone residuals using TOMS and empirically improved SBUV measurements: Application to an ozone pollution episode over the eastern United States, *J. Geophys. Res.*, **104**, 30,319-30,340, 1999.
- Fishman, J., and V.G. Brackett, The climatological distribution of tropospheric ozone derived from satellite measurements using version 7 TOMS and SAGE data sets, *J. Geophys. Res.*, **102**, 19,275-19,278, 1997.
- Fishman, J., C.E. Watson, J.C. Larsen, and J.A. Logan, Distribution of tropospheric ozone determined from satellite data, *J. Geophys. Res.*, **95**, 3599-3617, 1990.
- Fishman, J., V.G. Brackett, E.V. Browell, and W.B. Grant, Tropospheric ozone derived from TOMS/SBUV measurements during TRACE-A, *J. Geophys. Res.*, **101**, 24,069-24,082, 1996a.
- Fishman, J., J.M. Hoell, Jr., R.D. Bendura, R.J. McNeal, and V.W.J.H. Kirchhoff, NASA GTE TRACE-A experiment (September-October 1992): Overview, *J. Geophys. Res.*, **101**, 23,865-23,879, 1996b.
- Fishman, J., A.E. Balok, and F.M. Vukovich, Observations of Tropospheric Chemistry from Space: Past Insights and Future Directions, *Adv. Space Res.* (in press) 2001.
- Gregory, G.L., H.E. Fuelberg, S.P. Longview, B.E. Anderson, J.E. Collins, and D.R. Blake, Chemical characteristics of tropospheric air over the tropical South Atlantic Ocean: Relationship to trajectory history, *J. Geophys. Res.*, **101**, 23,975-23,972, 1996.
- Hudson, R. D., and A. M. Thompson, Tropical tropospheric ozone (TTO) from TOMS by a modified-residual method, *J. Geophys. Res.* **103**, 22,129-22,145, 1998.
- Logan J.A., An analysis of ozonesonde data for the troposphere: Recommendations for testing 3-D models, and development of a gridded climatology for tropospheric ozone, *J. Geophys. Res.*, **104**, 16,115-16,149, 1999.
- McPeters, R. D., et al., Nimbus 7 Total Ozone Mapping Spectrometer (TOMS) data products user's guide, Rep. NASA RP-1323, Natl. Aeronaut. and Space Admin., Greenbelt, Md., 1993.
- Thompson, A. M., and R. D. Hudson, Tropical tropospheric ozone (TTO) maps from Nimbus 7 and Earth Probe TOMS by the modified-residual method: Evaluation with sondes, ENSO signals, and trends from Atlantic regional time series, *J. Geophys. Res.*, **104**, 26,961-26,975, 1999.
- Thompson, A.M., J.C. Witte, R.D. Hudson, H. Guo, J.R. Herman, and M. Fujuwara, Tropical tropospheric ozone and biomass burning, *Science*, **291**, 2128-2132, 2001.
- Vukovich, F.M., V. Brackett, J. Fishman, and J.E. Sickles, II, On the feasibility of using the tropospheric ozone residual for nonclimatological studies on a quasi-global scale, *J. Geophys. Res.*, **101**, 9093-9105, 1996.

- Vukovich, F.M., V. Brackett, J. Fishman, and J.E. Sickles, II, A 5-year evaluation of the tropospheric ozone residual at nonclimatological periods, *J. Geophys. Res.*, **102**, 15,927-15,932, 1997.
- Ziemke, J.R., and S. Chandra, Comment on “Tropospheric ozone derived from TOMS/SBUV measurements from TRACE A” by J. Fishman et al., *J. Geophys. Res.*, 103, 13,903-13,906, 1998.
- Ziemke, J. R., S. Chandra, and P. K. Bhartia, Cloud slicing: A new technique to derive upper tropospheric ozone from satellite measurements, *J. Geophys. Res.*, **106**, 9853-9867, 2001.
- Ziemke, J. R., S. Chandra, and P. K. Bhartia, Two new methods for deriving tropospheric column ozone from TOMS measurements: The assimilated UARS MLS/HALOE and convective-cloud differential techniques, *J. Geophys. Res.*, **22**,115-22,127, 1998.
- Ziemke, J. R., S. Chandra, and P. K. Bhartia, A new NASA data product: Tropospheric and stratospheric column in the tropics derived from TOMS measurements, *Bull. Amer. Meteor. Soc.*, **81**, 580-583, 2000.

6. Convergence of O₃ Algorithms

Pawan K Bhartia

NASA Goddard Space Flight Center, Greenbelt, Maryland, USA

6.1. Overview

In the previous chapters, we discussed four different ozone algorithms designed to produce 3 products, including 2 algorithms for total ozone. One can reasonably argue that it should not be necessary to have so many algorithms to produce what is essentially a single product, vertical profile of ozone, of which total ozone and tropospheric ozone column are just special cases. Since the O₃ profile algorithm, described in Chapter 4, uses a superset of wavelengths that includes the wavelengths that the two total O₃ algorithms use, it has access to more information than the two total O₃ algorithms. Therefore, from optimal estimation theory, the profile algorithm should do at least as well in deriving total O₃, if not better. Viewed from this perspective, the only reason the tropospheric O₃ residual algorithm can extract new information from total O₃ data is that it incorporates better *a priori* (from the other Aura instruments) than that used by the profile algorithm. One should be able to achieve at least as good a result, if not better, by providing the same *a priori* to the profile algorithm.

As we discussed in Chapter 1, the reason why we have started out with 4 different algorithms has to do with heritage, past experience, and level of maturity of the various algorithms. TOMS V8 total ozone algorithm is the most recent version of a series of algorithms that have been progressively refined over the last 30 years. It is computationally very fast and requires very little input data (few measurements per pixel). The results of V8 and its predecessor algorithms have been extensively compared with ground-based Dobson and Brewer instruments. Though there are latitudinally and seasonally varying biases between the TOMS V8 results and the ground network, these biases have become smaller with V8.

By contrast, our experience using the DOAS and the maximum likelihood O₃ algorithms is more limited. There are several versions of these algorithms that produce significantly different results even when applied to the same data. Though, so far, there is no conclusive evidence that any of these algorithms agree better with ground-based network than the simpler TOMS algorithm, the strengths and weaknesses of the various algorithms are getting better understood. This has already resulted in modifications to the basic algorithms. For example, most DOAS algorithms are now planning to use total ozone-dependent air mass factor, which are calculated using profiles similar to those used by TOMS. In turn, the modified TOMS algorithm we describe in Chapter 2 uses the concept of differential absorption to isolate SO₂ from O₃, to correct for instrument drift, and to check the aerosol and sea-glint correction algorithm. Based on this experience, one can think of a “super algorithm” that would draw upon the strengths of the four algorithms we have proposed in this document. We believe that it is prudent to develop this algorithm in stages, rather than all at once. The following plan describes a possible build scenario for developing such an algorithm.

6.2. Profile Correction to total O₃ algorithms

Both the DOAS and the TOMS V8 total O₃ algorithms must use *a priori* profiles to derive total O₃. In principle, one may be replace these profiles with the profiles retrieved by the profile algorithm to improve the total O₃ estimates. Both algorithms have built-in features that allow them to use external profile information. However, as is clear from the averaging kernels shown in Chapter 4, the profile algorithm can provide very limited profile information below 20

km. So far, there is no evidence that the profile algorithm will be able to do significantly better below 20 km than the total O₃-dependent climatology described in Chapter 2. Though it can certainly do better at higher altitudes, the profile above 20 km, does not become important for total O₃ retrieval until the slant column density (SCD) of O₃ becomes quite large. For TOMS V8 this happens when SCD > 3000, which typically occurs at solar zenith angles > 82°, affecting only few percent of the OMI data. The situation should be roughly the same for the DOAS algorithm. Therefore, the OMI-derived O₃ profiles would be useful only at very large solar zenith angles to correct TOMS and DOAS total O₃.

6.3. Combining TOMS and DOAS algorithms

A key difference between the TOMS and the DOAS algorithms is that TOMS takes advantage of the strong continuum absorption of O₃ in the Huggins band (310-340 nm), while the DOAS algorithm uses the much weaker band absorption. As shown in Fig 6-1, the total absorption of the radiation is more than an order of magnitude larger than the differential absorption near 331 nm. Therefore, in principle, an algorithm that takes advantage of the total absorption of O₃ near 310 nm should be able to measure total O₃ with far greater precision than the DOAS algorithms. There are several reasons why such an algorithm has not yet been

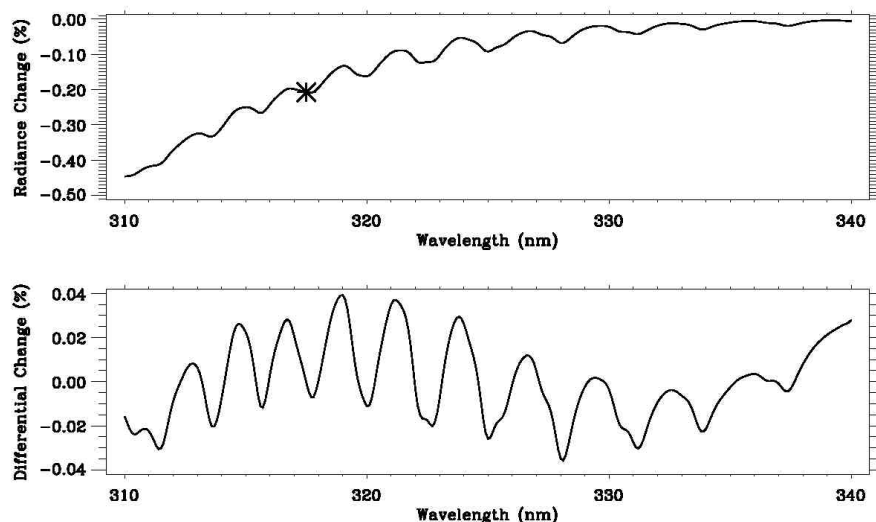


Figure 6-1: The upper panel shows change in absolute radiance produced by 1 DU increase in stratospheric O₃ at 45° SZA, nadir view. TOMS total O₃ wavelength is shown by the asterisk. The lower panel shows differential absorption obtained by subtracting a quadratic polynomial from the upper curve. OMI DOAS algorithm uses wavelengths longer than 331 nm.

developed. First, as noted before, removal of continuum absorption from the radiance spectrum also removes the interfering effects of aerosols, clouds, sea-glint etc.; indeed one removes any smoothly varying errors in radiative transfer calculations or in the instrument calibration. Thus, apart from errors that might be caused by the Ring Effect, the DOAS algorithm is largely insensitive to many forward model and instrument errors that have plagued previous algorithms, such as TOMS, that do not use differential absorption. In order to develop a total-absorption algorithm, the forward model must explicitly account for aerosols and clouds (i.e., by treating them as Mie scatterers rather than Lambertian reflectors), and the parameters that are needed to run such a model, cloud/aerosol optical depth, single-scattering albedo etc. must be supplied externally. As discussed in another ATBD, there are plans to calculate these parameters using the

longer OMI wavelengths. These parameters could be incorporated in the forward model, but with significantly added complexity. In addition, total-absorption algorithms require absolute values of TOA reflectances, rather than differential reflectances.

Given these inherent difficulties in developing a total-absorption algorithm, one may legitimately question the need for such an algorithm. Given the expected S/N of OMI, the DOAS algorithm described in Chapter 3 should provide daily global maps of vertical column density of O₃ to a precision of ~1%, at spatial resolution of ~25 km. This should be more than sufficient for any conceivable scientific study involving stratospheric column ozone. However, this is not the case if one is interested in studying tropospheric ozone from OMI. From Table 2-1 it can be noted that the short term variation of tropospheric O₃ in the lowest 5 km, as seen by the Hohenpeissenberg ozonesonde station, which is located not very far from major industrial areas of Europe, is only about 3 DU (1 σ). If one multiplies this number by the layer efficiency factor of 0.5 (described in Section 2.3.1) the expected variation in the total O₃ derived from OMI (irrespective of the algorithm used) would be only 1.5 DU (1 σ). So, even if one can do a very good job of removing the UTLS overburden from total O₃ (using other Aura instruments or cloud slicing), the minimum requirement for observing the lower tropospheric O₃ variations, at the full spatial resolution of OMI, is to achieve better than 1 DU precision in measuring total O₃. Even better precision is required if one wants to study planetary boundary layer O₃ enhancements in urban areas using OMI. From Fig. 6-1 it is obvious that it would be very difficult to achieve such high precisions with any differential absorption algorithm, but it may be possible to do so if one could take advantage of the total absorption of O₃ near 310 nm.

6.4. Combining TOR and Profile algorithms

Initially, the profile algorithm is likely to use latitude and season-dependent *a priori*. But if the TOR algorithm described in Chapter 5 is successful in showing that other Aura instruments are providing accurate estimates of stratospheric column O₃, one could, in principle, use the entire profile (of both temperature and O₃) produced by these instruments as *a priori* for O₃ profile retrieval using OMI. This would allow one to combine high spatial resolution information from OMI with high vertical resolution information from other Aura instruments in an optimum way.

6.5. Full Convergence of the 4 Algorithms

Above we have described three partial convergence scenarios, involving two algorithms at a time, which could lead to a single converged algorithm. To summarize, it is first necessary to demonstrate that the profile algorithm can reliably correct the total O₃ derived using the two total O₃ algorithms at large SCDs. Then it is necessary to demonstrate that a reliable algorithm that takes full advantage of the total absorption of O₃, rather than differential absorption, can be built to derive total O₃ with very high precision. Finally, we should consider bringing-in high vertical resolution profile information from other Aura sensors to improve OMI profiles, thus achieving a unique multi-instrument algorithm integration that could provide high spatial and high vertical resolution O₃ profiles over the entire globe.